Multimodal Tip Enhanced Raman Microscopy with a Cylindrical Vector Beam Focused by a Parabolic Mirror

Dissertation

der Mathematisch-Naturwissenschaftlichen Fakultät

der Eberhard Karls Universität Tübingen

zur Erlangung des Grades eines

Doktors der Naturwissenschaften

(Dr. rer. nat.)

vorgelegt von

Dipl. Chem. Kai Braun

aus Nürtingen

Tübingen

2014

Tag der mündlichen Qualifikation: 11.04.2014
Dekan: Prof. Dr. Wolfgang Rosenstiel
1. Berichterstatter: Prof. Dr. Alfred J. Meixner
2. Berichterstatter: Prof. Dr. Thomas Chassé

Table of Contents

Abstract

In my PhD-work I have developed and implemented several new functions in an existing near-field optical microscope based on a parabolic mirror for excellent tip illumination and optical signal collection. This improved microscope is an ideal tool for performing imaging and spectroscopy on opaque samples, in particular molecular films deposited on flat substrates with a spatial resolution on the order of 10^{-3} times then the optical wavelength. The new functions were hyperspectroscopic imaging, fluorescence life time imaging (FLIM) and scanning bias voltage tip enhanced Raman spectroscopy (SBV-TERS) based on a self built Scanning Tunneling Microscope (STM)-scan head. Utilizing these improvements, several new measurement methods have been developed, were the bias voltage is used to apply a strong electric field in the gap mode to manipulate and directly monitor the sample on a molecular scale. The results out of this thesis demonstrate how optical enhancement inside the gap mode can be further increased by a stronger localization via tunneling through a molecule. The bias voltage activated stimulated emission from an illuminated single molecule tunneling junction can improve the fundamental understanding of quantum plasmonics and lead to new analytical applications. Furthermore, this concept represents the basis for novel ultra-small, fast, optically and electronically switchable devices and could find applications in high-speed signal processing and optical telecommunications. The thesis is composed on the development of the setup and the following experiments exploring different questions on organic semi conductors. This work consists three chapters, describing the evolution of the microscope and the methods used for investigating different molecular systems which are relevant for organic electronics.

Firstly we have investigated a Diindinoperylen (DIP) molecular island film on silicon. DIP is a prominent candidate for several applications in organic electronics and is used e.g. in solar cells or Field effect Transistors (FET). The molecular films are evaporated and upon growing they form domains with a homogenous size and structural network, but different height boundaries. We measured tip enhanced near-field luminescence with an Avalanche Photo Diode (APD). In addition we measured spectra at relevant positions with different tip-sample separations. The topography recorded with tuning fork shear-force microscopy nicely shows the molecular islands. Single molecular steps at the domain boundaries can be resolved and revealing the upright orientation of the molecule. This can also be verified by Raman spectroscopy as mainly the out-of-plane modes are observed. In the presence of a near-field probe the luminescence of the molecular film is strongly enhanced. By scanning the tip above

the surface we saw an even further increase of the photoluminescence (PL) at the boundaries of the island and domains with a resolution better than 20 nm. Such phenomenon cannot be seen by conventional diffraction limited optical confocal microscopy. In a first model we stated the enhancement effect as a coupling between the plasmonic mode of the tip with an exciton polariton in the DIP-film and presented first theoretical calculations. The local film morphology does strongly influence the coupling and thus the radiative transition of the polariton leading to the PL-contrast in the images.

So far only single, local TERS spectra could be recorded, while the optical images of the integrated optical intensity recorded point by point with an APD. As a next step I have implemented a full synchronization of the spectrometer with the scanning unit. Thanks to this improvement, a preselected superimposed grid defines the positions were tip enhanced Raman spectroscopy (TERS) spectra can be recorded. We applied this technique to a couple of different samples and showed that high resolution spectral imaging or hyperspectral imaging is an ideal tool for studying a broad range of different phenomenon. For example, we studied the active layer of an organic photovoltaic cell, which consists of a polymer blend film. By measuring simultaneous the morphology and the spectroscopic information of a poly-3-hexylthiophene (P3HT) and [6,6]-phenyl-C_{61}-butyric acid methyl ester (PCBM) blend film the chemical distribution can be optically resolved with a previously unreached resolution. Furthermore the interplay among the quenching efficiency of the P3HT at the domain boundaries to the PCBM was mapped.

In this chapter the following experiments are based on the most recent modification of the microscope with a STM feedback and a diode laser as excitation source, which can be operated in pulsed or in continuous wave mode. The main emphasis of this work is to study self assembled monolayer (SAM) films on gold substrates. Such systems can be used as model interfaces of molecules and a metal electrode, as used in organic electronics. The combination of TERS and STM allows studying molecules on metallic surfaces under varying DC electric fields between the tip and the substrate. We show the influence of the electric-field on a SAM of Benzotriazole (BTA), 2-Mercatobenzothiazole (MBT) and 5-Chloro-2-Mercatobenzothiazole (Cl-MBT) by measuring spectra at different bias voltages. We acquired the chemical fingerprints of the molecules in the gap and impose reproducible changes in the individual spectra. Moreover the molecules, which are chemically bound to the surface, give rise to a massive enhancement of the luminescence if the bias voltage is higher than the energy gap between the Highest Occupied Molecular Orbital (HOMO) and the Fermi level of

the sample. The enhanced photon-emission occurs from radiative recombination by electrons close to the Fermi-level of the metal substrate to the HOMO of the molecule. Spectral narrowing and a nonlinear intensity increase as a function of bias voltage and optical pump power suggests that optical feedback and stimulated emission take place were the gap mode acts as a plasmonic resonator. To our best knowledge this effect has not been reported so far.

Zusammenfassung

Zusammenfassung

In meiner Doktorarbeit habe ich für ein bestehendes Nahfeld-optisches Mikroskop neue Messfunktionen entwickelt und eingebaut. Das Mikroskop benutzt einen Parabolspiegel als fokussierendes Element, der besonders geeignet ist, um die genutzte Spitze zu beleuchten und um das von der Probe gestreute optische Signal zu sammeln. Das erweiterte Mikroskop ist ein ideales Instrument, um auf lichtundurchlässigen Proben optische Abbildungen und Spektroskopie mit einer räumlichen Auflösung im Bereich von 10^{-3} der optischen Wellenlänge durchzuführen. Besonders geeignet sind hier molekulare Filme, welche auf ebenmäßigen Substraten abgeschieden wurden. Die damit neu gewonnenen Funktionen sind hyperspektrale Abbildung, eine Abbildung von Fluoreszenz-Lebenszeiten (FLIM) und spitzenverstärkte Raman-Spektroskopie bei unterschiedlichen Bias Spannungen (SBV-TERS), die auf einem selbstentwickelten Rastertunnelmikroskop (STM) basiert. Durch diese Erweiterungen wurden neue Messmethoden entwickelt, bei denen die Bias-Spannung benutzt wird, um ein starkes elektrisches Feld zwischen der Spitze und der Probe anzulegen. Dadurch kann die Probe auf molekularer Ebene direkt manipuliert und beobachtet werden. Die in der Arbeit beschriebenen Resultate dieser Methode zeigen, dass die optische Verstärkung zwischen Spitze und Probe noch weiter erhöht werden kann, indem man eine stärkere Lokalisierung durch einen molekularen Tunnelprozess erzeugt. Die hierbei auftretende durch Bias-Spannung aktivierte stimulierte Emission eines angeregten Einzelmolekül-Tunnelkontaktes kann zu einer Besserung unseres wesentlichen Verständnisses der Quantenplasmonik beitragen und so zu neuen analytischen Anwendungen führen. Außerdem repräsentiert dieses Konzept die Basis für neuartige ultra-kleine und -schnelle Bauteile, die sowohl optisch als auch elektrisch schaltbar sind und Anwendung in der Hochgeschwindigkeits-Signalverarbeitung und optischen Telekommunikationstechnik finden

können. Die Doktorarbeit ist zusammengesetzt aus dem Aufbau und der Entwicklung des Mikroskops sowie der zugehörigen Experimente, die sich mit verschiedenen Fragestellungen in der organischen Halbleitertechnik beschäftigen.

Zu Beginn wurden molekulare Inselfilme aus Diindinoperylen (DIP) auf Silizium untersucht. DIP ist ein vielversprechender Kandidat für einige Anwendungen in der organischen Halbleitertechnik und findet z.B. Nutzen in Solarzellen oder Feldeffekt-Transistoren (FET). Die molekularen Filme werden aufgedampft und bilden während des Wachstums Domänen aus, die ein einheitliches strukturelles Netzwerk und eine einheitliche Größe bilden, sich aber in der Schichtanzahl unterscheiden. Hierauf wurden spitzenverstärkte Lumineszenz-Bilder mit einer Lawinen-Photodiode (APD) aufgenommen. An verschiedenen einschlägigen Abstandspositionen zwischen Spitze und Probe wurden außerdem optische Spektren aufgenommen. Das Topographiebild, basierend auf einer Stimmgabel-Scherkraft-Mikroskopie, zeigt deutlich die molekularen Inseln. Einzelmolekülstufen an den Domänengrenzen sind deutlich zu erkennen und zeigen die aufrecht stehende Orientierung der Moleküle. Dies kann auch durch die Raman-Banden verifiziert werden, da nur die Banden außerhalb der Molekülebene im Spektrum sichtbar sind. Beim Rastern der Spitze über die Probe zeigte sich eine zusätzliche Erhöhung der Photolumineszenz (PL) an den Domänen- oder Inselgrenzen, die mit einer optischen Auflösung von weniger als 20 nm abgebildet werden konnte. Dieses Phänomen kann mit konventioneller, beugungsbegrenzter optischer Mikroskopie nicht beobachtet werden. In einem ersten Modell wurde die erhöhte Lumineszenz als eine Kopplung des Plasmons der Spitze und eines Exciton-Polaritons innerhalb des DIP-Films erklärt und durch erste theoretische Kalkulationen unterstützt. Die lokale Morphologie des Films beeinflusst diese Kopplung und damit auch den strahlenden Übergang des Polaritons, der zu dem PL-Kontrast in den Bildern führt, stark.

Bis hierhin konnten nur lokale TERS-Spektren aufgenommen werden. Die optischen Bilder wurden durch eine Punkt-für-Punkt-Abbildung erzeugt, indem eine APD die optische Antwort integrierte. Als zusätzliche Verbesserung habe ich eine volle Synchronisation des Spektrometers mit der Rastereinheit realisiert. Durch diese Erweiterung kann über den gewünschten Probenausschnitt ein vorher festgelegtes Gitter aus Punkten gelegt werden, wo während der optischen Messung ein TERS-Spektrum aufgenommen werden soll. Wir haben diese Technik auf eine Reihe von verschiedenen Proben angewendet und gezeigt, dass hochauflösende, spektrale Abbildung oder hyperspektrale Abbildung ein ideales Instrument ist, um einen breiten Bereich von optischen Phänomenen zu untersuchen. Als ein Beispiel

untersuchten wir die aktive Schicht einer organischen, photovoltaischen Zelle, die aus einem gemischten Polymerfilm besteht. Durch die gleichzeitige Messung der Morphologie und der spektroskopischen Information eines gemischten Films von Poly-3-Hexylthiophen (P3HT) und [6,6]-Phenyl-C_{61}-Butyricsäuremethylester (PCBM) kann die chemische Verteilung mit einer bis dahin nicht erreichbaren optischen Auflösung festgestellt werden. Zudem konnte die Wechselwirkung von P3HT zu PCBM an der Domänengrenze anhand der Löschungseffizienz direkt abgebildet werden.

Die Experimente im folgenden Abschnitt basieren auf der neuesten und wichtigsten Modifikation des Mikroskops. Dabei wurde mit einer STM-Abstandsregelung und einen Diodenlaser als Anregungsquelle gearbeitet. Dieser Laser kann entweder in gepulstem oder im Dauerstrich-Modus betrieben werden. In diesem Teil der Arbeit liegt der Schwerpunkt auf Filmen von selbstordnenden Monolagen (SAM) auf Goldsubstraten. Dieses System kann als Modellsystem für die Grenzfläche eines Moleküls an einer Metallelektrode betrachtet werden, welche in der organischen Elektronik oft vorkommt. Durch die Kombination von TERS mit einem STM kann man Moleküle auf einem metallischen Substrat unter dem Einfluss eines Gleichstromfeldes zwischen Spitze und Probe untersuchen. Indem wir Spektren mit unterschiedlichen Bias-Spannungen aufnahmen, zeigten wir den Einfluss eines elektrischen Feldes auf einen SAM von Benzotriazol (BTA), 2-Mercatobenzothiazol (MBT) und 5-Chloro-2-Mercatobenzothiazol (Cl-MBT). Hierbei haben wir die bekannten Raman-Banden der Moleküle zwischen Spitze und Probe aufgenommen und reproduzierbare Veränderungen in den einzelnen Spektren erzeugt. Darüber hinaus erzeugten die chemisch an das Substrat gebundenen Moleküle eine massive Verstärkung der Lumineszenz, wenn die positive Bias-Spannung an der Spitze größer wurde als der energetische Abstand zwischen dem höchstbesetzten Molekülorbital (HOMO) und dem Fermi-Level der Probe. Die verstärkte Photonenemission wird durch eine strahlende Rekombination von Elektronen nahe der Fermi-Kante des Substrates zum HOMO des Moleküls ausgelöst. Die als Funktion der Bias-Spannung auftretende Banden-Verschmälerung der Emission und der nichtlineare Anstieg der Intensität legen nahe, dass es sich hierbei um eine stimulierte Emission mit einer optischen Rückkopplung handelt – wobei der Bereich zwischen Spitze und Probe als plasmonischer Resonator fungiert. Unserem Kenntnisstand nach wird von einem solchen Effekt hier zum ersten Mal berichtet.

Motivation

Within the last several years, the rapid development of organic based electronics lead to a lot of marketable products. To these belong solar cells, FETs, light emitting diodes (LED) and even more complex systems, like displays. Even so there has been a great effort; a lot of questions about the working principle on the microscopic scale are still not answered. With some of the products the engineering is still empirical. Since the functions are related to charge transfer, charge separation or light absorption optical spectroscopy is widely used. These interactions take mainly place at the various interfaces like the grain boundaries in blend films and the contact to the electrode and hence are of great interest. The local morphology and the microscopy structure of the active specimen are determining the efficiency. Hence optical microscopy is often coupled with luminescence or Raman spectroscopy.

The so called Abbe limit, settled 1880 set for a long time the lower limit in reachable optical resolution. Although Synge proposed a method to descend this limitation in 1928 it still needs more then 50 years to invent the Scanning Near-field Optical Microscope (SNOM)[1]. This retardation was mostly caused by technical limitations, which have been solved by e.g. the invention of the laser[2] that provides a stable and bright light source. In the first experiments the sample has been illuminated thru a hole much smaller than the half wavelength of the used laser light. The size of the hole then sets the accessible optical resolution and is not restricted to the used illumination light anymore. Also the hole needed to keep at a nanometer distance to the sample, which has been achieved by piezoelectric movement stages. These essential requirements lead to the developing of the metalized glass fiber tips, which are still used up to today. Since these pioneering experiments a lot of effort has been done to overcome several limitations this approach still have. The size of the hole can't be made smaller than several tens of nanometer otherwise the throughput is too low. Moreover weak but chemically very sensitive Raman signals could not be detected properly. With the beginning of the new millennium the latest evolution in SNOM has been introduced. The Tip Enhanced Raman Spectroscopy (TERS)[3,4] and the following more specific methods e.g. Scanning Near-field Gap Mode Microscopy (SNGM) give not only rise to an increased resolution, but even further also increase the sensitivity, thru to the enhanced electromagnetic field below a sharp noble metal tip or particle. This invention allows actually to measure single molecules.

In this thesis we show our ongoing development on new tools and methods to gain a deeper understanding of organic semi conducting molecules and effects on electrode interfaces. We think that the combination of high resolution near-field optical microscopy with optical spectroscopy is an ideal tool to study such systems

1. Scientific Background and Working Principle

1.1 Optical Resolution

The image of a point-light source is called Airy pattern and consists of a bright centered spot, surrounded by circular rings. In a modern optical microscope the size of the airy disc is given by the Abbe Limit taking into account the numerical aperture (NA) and the effective emitted wavelength. A common way to describe the resolution of an optical microscope is the Rayleigh criterion. According to this definition, the smallest separation, where two point-like objects at the same wavelength can still be distinguished, is given by the distance of the first minimum to the center of the airy disc. In the past years several techniques have been developed to overcome this limit by distinguishing the two point objects by taking into account additional parameters. Nowadays there are several accepted ways to describe the optical resolution. Depending on the desired information e.g. localization of a point light source or the dimension of the optical response, for the same microscope there are several ways to increase the "resolution". In Photoactivated Localization Microscopy [PALM][5] or Stochastic Optical Reconstruction Microscopy [STORM][6] experiments the position of a isolated molecule can be localized better than 10 nm although the microscope itself has only a diffraction limited resolution of about 1 μm. Here the two light sources can be isolated since they are not emitting at the same time, i.e. time is the additional parameter. Therefore the localization is the main information and only depends on the accuracy with which the center of the Airy disc can be determined. In contrast to that, the following other methods increase the resolution by decreasing the optical image directly. In Stimulated Emission Depletion [STED][7-9] this is done with two overlapping foci with different intensity distributions, which are leading to a partly depletion of the specimen in the focus. Hence only a part of the focus will give an optical response. In contrast to that structured illumination[10] is a more technical approach, where the sample is excited with a patterned light source. By measuring the interference pattern of the illumination beam and the backscattered signal of the sample a computer program can deduct an image with twice the resolution. In 1974 the discovery of the surface enhancing effect of noble metals has lead to Surface Enhanced Raman Scattering (SERS)[11]. Here small particles or protrusions in the sample act as an optical antenna and give rise to a remarkable chemical sensitivity down to the single molecule level. The main drawback for imaging has been the fixed position of the active area. This problem was solved by the subsequent development of Tip enhanced Raman Spectroscopy (TERS)[3]. Hereby the

Localized Surface Plasmon (LSP) of a noble metal tip is used as an optical antenna. This effect allows also increasing the resolution in imaging by scanning the tip over the surface and is the method of choice in this work.

1.2 Localized Surface Plasmons and their role in TERS

A coherent, collective oscillation of the free electron gas in a bulk metal, driven by an external electrical field e.g. by a monochromatically polarized light source is called a plasmon oscillation. The plasmon itself is the energy quantum of this oscillation as a photon stands for an energetic quantum of an electromagnetic wave. In a perfect metal there are no intrinsic intensity losses throughout the whole frequency range. However, real metals have underlying limitations and only a few metals, in particular noble metals, can reach plasmon frequencies close to the optical regime. Since plasmons are electron oscillations, they can be described by the classical Maxwell´s equations with the charge carriers effective mass and the free electron gas density[12]. In principle there are three different types of plasmon oscillations. They are differentiated by their surroundings and dimensions. The so called bulk plasmon is characterized by its three dimensional surrounding, while the surface plasmon is always coupled to an electromagnetic wave which is propagating in the dielectric medium parallel to a metal/dielectric interface. The surface plasmon is also named surface plasmon polariton and has an evanescent character, which means it exhibits an exponential decay of the field strength perpendicular to the interface.

The third type is the localized surface plasmon (LSP). Here the electron oscillation is confined to a small volume element like a metal nano-particle, a metal tip, or a protrusion on a rough thin film. The LSP can be excited resonantly by an incident field with a matching momentum and direction. Since the electron gas is confined in three dimensions leading to a high local electron density at the surfaces. The resonance frequency strongly depends on material, geometry and size of the particle[37,38]. If the particle is placed close to a metal film and the incoming field is polarized perpendicular to the surface plane the LSP-oscillation of the particle create a mirror charge. This will lead to a coupled surface charge density oscillation, with slightly red shifted but even stronger confined field in the gap between the particle and the surface. This arrangement is quite similar to the traditional Helmholtz antenna and has a large scattering cross-section. Furthermore this configuration is also known as hot spot, a concept which is widely used in SERS to enhance the Raman sensitivity such that even single molecules can be observed[13].

1.3 Decisive Parameters

The main interests of TERS measurements are improved optical resolution and chemical sensitivity. In all our experiments we use gold tips, which are prepared according to Ren[14].

In order to efficiently excite the LSP of the tip we use a radially polarized cylindrical vector beam (CVB)[15]. This LSP generates a strong, evanescent electrical field at the apex of the tip. Hence its field strength drops dramatically by increasing the distance from the tip to the specimen[16,17]. At a gap size of approximately 10 nm to a sample surface the TERS-effect is negligible. Therefore the tip has to be kept at a short, constant distance from the sample surface for a maximum sensitivity. In our case this has been solved by either by a STM- or for non conductive samples a tuning fork shear-force feedback system.

The near-field originating from the tip is the main parameter for settling the increased lateral resolution. Since many years the size of the active area with the highest field enhancement is calculated with the tip apex radius. As a first consequence sharper tips lead to a higher resolution. In addition they create a stronger confinement of the field since the energy pumped into the optical antenna is concentrated to a smaller spot size.

Another parameter is the material of the sample itself. If the LSP of the tip can create a mirror charge in the sample, a so called gap mode is formed. It has been shown that this gap mode can even further increase the lateral resolution by additionally compressing the electric-field. State of the art experiments[18,19] have shown that the so far acknowledged theories needed to be revised since they cannot explain resolutions in the order of 1 nm. But they still predict the increased resolution at the basis of the pointed characteristics. In summary working on conductive samples one finds as general rule a higher resolution as well as for a decreasing gap size and for smaller tip radius.

1.4 Microscope Configuration

The major task is to choose the appropriate optical access and the desired configuration to excite the noble metal tip. There are several different solutions to fulfill this task, but in principle there are three main possibilities. The oldest and still widely used way is to set an Atomic Force Microscope (AFM) on top of an inverted microscope. The transparent sample is illuminated from below and the evanescent field at the upper sample/air interface is used to

excite the tip[4,20-22]. The main advantage is the rather easy implementation in commercial systems and the large optical access with no limitations to the microscope objective. Despite its benefits the main problem arises with opaque samples. Only thin optical transparent samples (e.g. dielectric or thin metal films) can be investigated. In contrast the side-illumination and the top illumination with a parabolic mirror (PM) are much more flexible and have no restrictions on the nature of the sample. In side illumination a p-polarized laser beam is shining on the tip[23]. From theoretical calculations it turns out that an angle of approx. 60 degree gives the best performance. Normally a long working distance objective with a numerical aperture (NA) between 0.5 to 0.8 is used for focusing the laser beam onto the tip. This NA is much smaller than for transmission illumination where a NA between 1.25 and 1.46 is used and leads to much lower detection efficiency.

In our case we use a PM as focusing and collecting element with a NA of almost 1 (0,998) giving a large collection angle. Furthermore the signal emerging from the focus can be collect within a solid angle of 2π, which is even better than with an immersion oil objective lens. In Fig. 2 a sketch of an illuminated PM is shown and shall illustrate the focusing principle. Only a small fraction of light is lost through to the shadowing by the sample. When a radially
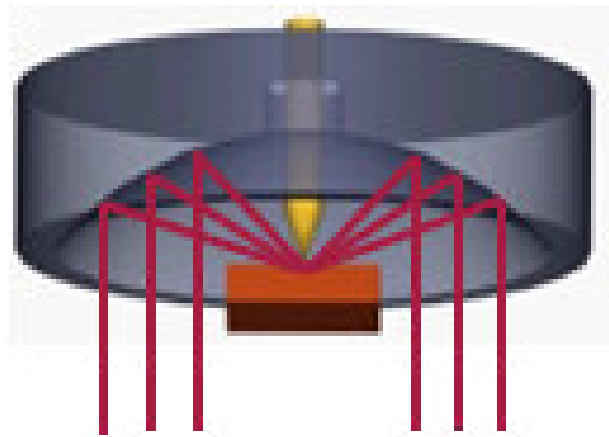

Fig. 1 Sketch of the Parabolic Mirror illuminated from below (red lines) and reflections on the surface which produce the focus. The tip is brought into this focus via a hole in the backside.

polarized doughnut mode (RPDM) is focused with such a PM, the electric field component is almost fully oriented parallel to the optical axis, which is hard to achieve with an objective lens[24]. Hence it is optimally suited for exiting a tip vertical to the PM basis. Furthermore such a focused RPDM gives the smallest diffraction-limited spot for a fixed NA and wavelength and has an area of only 0.134^2 lambda[25]. Hence the confocal background is further suppressed. The PM is a purely reflective optical element and gives rise to an optic which is completely free of chromatic aberrations. A major drawback for using the PM more frequently might be the problems to adjust the mirror properly. In comparison to an objective lens the PM is very sensitive to the alignment of the incoming beam. Even a small deviation of the k-vector of the incident beam from this optical axis gives rise to large aberrations[24]. An almost perfect parallel alignment of the incident laser beam is needed for a high quality

imaging. In Fig. 2 a sketch of the beam path of our PM microscope with a short description is shown.
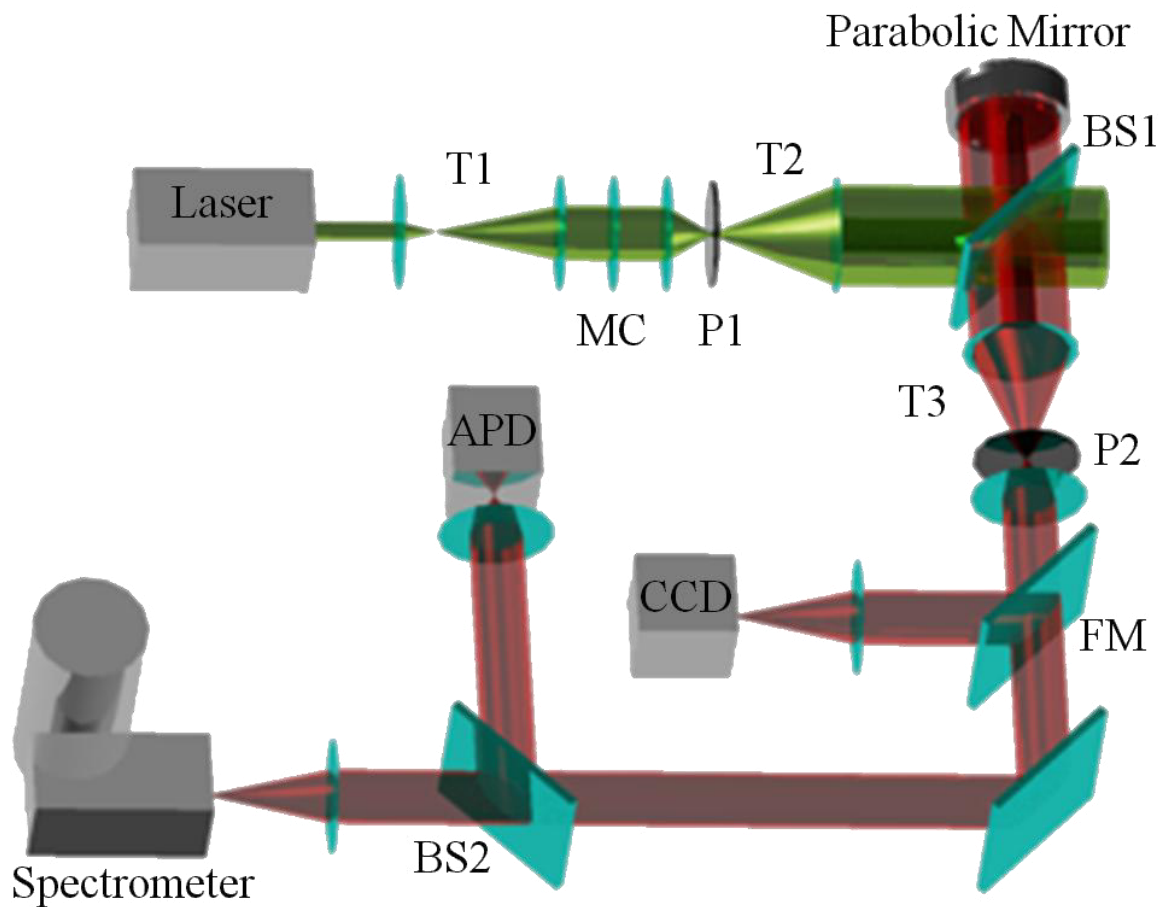

Fig. 2 Sketch of the beam path of a PM microscope. The laser light beam (green line) is enlarged by the telescope T1 and the mode converter MC transforms the linearly polarized beam into a higher order mode. Then the beam is further enlarged to match the dimensions of the PM in T2. The pinhole P1 cleans up the higher order mode and forms a cylindrical vector beam. Afterwards the light is transferred to the PM with a beam splitter BS1. The emitted signal (red line) is then reduced by T3 and guided to the BS2, which splits the signal equally to the two detectors. The flipping mirror FM and the CCD-camera are used as a help for adjustment.

2. Introduction

2.1 State of the art

With state of the art tip-enhanced near-field optical microscopy a spatial resolution on the order of a few nanometers has been achieved, which is dramatically below the diffraction limit and single-molecule sensitivity has been shown by several groups.[23,26-28] The heart of this technique is a sharp noble metal tip, made typically of Ag or Au that works like an optical antenna when it is illuminated with a tightly focused laser beam and brought as close as a few nanometers to the sample surface. This configuration enhances the incident optical field in the gap and leads also to an enhanced emission of photons from the gap[29-31]. The field enhancement is particularly high if the electric field-vector of the incident optical radiation is oriented along the tip axis and excites a coherent oscillation of the conducting electrons, called a plasmon oscillation, which creates a highly localized oscillating surface charge at the tip apex. The sample is polarized by the local electrical field and responds with a mirror surface charge just below the tip apex. Hence a highly confined gap-field is created by plasmon-polariton coupling between the tip and the sample which critically depends on the tip- and the sample-properties in the gap. A sensitive feedback loop based on tunneling[32] or mechanical force[33] prevents the tip from crashing into the surface. A super-resolution image can be recorded by scanning the tip or the sample in nanometer steps. At every pixel the topography and an optical spectrum can be recorded synchronically showing typically a luminescence back-ground and the enhanced narrow Raman lines of the molecules in the gap. Hence, the technique allows for recording simultaneously the topography and the chemical information with very high spatial resolution. Various fascinating results have recently shown the power of this technique in the spectral domain[23,34], using continuous laser excitation. Very recently Deckert et al. have demonstrated the direct molecular distinction of selected amino acids on insulin fibril surfaces with a lateral resolution better than 2 nm by applying tip-enhanced Raman spectroscopy (TERS)[35]. They can also induce and observe a photocatalytic reaction employing a dual wavelength approach by bringing a silver-coated atomic force microscope tip in contact with a self-assembled monolayer of p-nitrothiophenol molecules adsorbed on gold nano plates. The tip was used in a twofold way firstly to enhance the Raman signal and secondly to act as the catalyst[36]. The progress of surface- and tip-enhanced Raman spectroscopy for bioanalytical applications has been significant and has been summarized in an excellent recent review by Popp et al[37]. Nanoscale chemical imaging of non transparent

samples has made significant advances using top or side illumination tip-enhanced infrared[38] and Raman mapping[39,40]. A further exciting direction is related to the excitation of propagating surface plasmon polaritons in thin metal films e.g. by individual semiconducting single-walled carbon nanotubes[41] or in thin metal wires by low-energy electron tunneling[42].

It should be noted that emission of photons from local surface plasmons excited by inelastic tunneling in the tip-sample gap of a STM has already been experimentally[43] observed and theoretically[44] explained twenty years ago. A low fraction of tunneling electrons can interact with particular quantum states in the tunneling junction provided e.g. from molecular vibronic levels and thus transfer energy. Hence the process excited by inelastic tunneling (IET) can be detected decoupled from the STM. If the bias voltage exceeds 1.8 V optical transitions can be detected. Shortly after the initial pioneering work followed the first photon emission experiments at molecular resolution induced by inelastic tunneling through an annealed monolayer of carbon-60 molecules on an Au (110) surface[45]. In a careful study of hexa-tert-butyl-decacyclene (HTBD) molecules adsorbed on clean Au(111), Ag(111) and Cu(111) surfaces in UHV at 4.6 Kelvin it turned out, however, that the tunneling induced luminescence spectra originate from plasmon mediated emission of the substrate and the tip; while the molecules act as spacer, slightly modifying the plasmon emission[46]. In contrast to carbon 60 which is spherical and can have a transition dipole moment perpendicular to the substrate surface, HTBD is a planar molecule with a large π-electron system and a transition dipole moment for the lowest electronic transition oriented in the molecular plane. This suggests efficient coupling to surface plasmons and fast nonradiative decay. However, when the molecule is decoupled from the metal surface by a thin spacer layer inelastic tunneling can directly excite different vibronic transitions inside a single molecule[47-49]. Since the first observations of light emission stimulated by inelastic electron tunneling through a junction formed by a conducting sample and a STM tip this has been a very active field of research and was applied to a variety of systems, including pristine metal surfaces, single molecules on ultrathin dielectric films, molecules assembled in thin films or in nanostructures on metal surfaces or on dielectric films. For an excellent recent review see reference[50].

A popular method to study a few or even one single molecule in a tunneling gap is the so-called break junction[51]. In the simplest case a thin gold wire is mounted on a flexible substrate, which can be bent until the wire breaks forming nanometer junction between two sharp tips. A stable tunneling feedback can be obtained in such a configuration, which is similar to a STM. Afterwards a droplet of a very low concentrated solution is deposited to the

junction and rinsed carefully until only a few molecules are close by. It has been shown that it is possible to build a single metal-molecule-metal-contact in that way and to study the electrical properties of a single molecule. The last two methods work nicely and are powerful techniques, but it is not exactly clear what happens when the electrons pass through the molecule in the junction. Here it would be very helpful to record Raman spectra additionally, because they show the specific chemical fingerprint of the molecular structure. However, only a very limited number of reports have addressed this very important task. Only recently Liu et al[52] have introduced a "fishing mode" STM-technique where a 4,4´-bipyridine-molecule binds symmetrically between a sharp Au-tip and an Au-surface forming a single-molecule tunneling junction. By focusing a laser-beam onto the tunneling junction they observe directly the different conducting stats (on/off) in the (single-molecule) TERS-spectra.

2.2 Novelty of the work

In the work for my PhD I have further developed a homebuilt parabolic mirror scanning near-field optical microscope (PM-SNOM). I have implemented new measuring modes to further investigate organic semi conducting molecules and molecule/electrode interfaces. The first SNOM measurements and the design of the optical path have been done a few years before. The distance feedback of the tip was purely based on a tuning fork shear force feedback by tracking the real part of the oscillation amplitude. With this microscope as a starting point of the work I have investigated:

- Near-field study of Diindinoperylen (DIP) island thin films on silicon. The performed experiments have shown that the luminescence intensity in the near field was strongly increased and revealed the importance of the plasmon polariton coupling between the tip and the DIP crystalline film. A correlation among the enhanced PL intensity and the local film morphology at the nanometer scale was for the first time observed.

- Fully synchronized hyperspectroscopic imaging and morphology imaging. I have implemented a synchronization of the spectrometer with the scanning probe unit. This was one of the first systems with such a capability. Combining the topography, Raman and PL signal allows us two directly map the chemical nature of the single domains. With this technique we were able to study polymer blend films of poly3-

hexylthiophen (P3HT) and [6,6]-phenyl-C_{61} butyric acid methyl ester (PCBM), which are used as active layers in organic solar cells. We have investigated the influence of thermal annealing upon the morphology and the distribution of the two components. We were able to detect the interplay between these two components, e.g. the PL quenching efficiency of P3HT according to the presence of PCBM with an optical resolution of approximately 10 nm. Furthermore the PL quenching of the donor (P3HT) leads to a quantitative study of the electron transfer to the acceptor (PCBM). These measurements demonstrate the possibility of high resolution spectroscopic imaging as a versatile tool for studying chemical compositions and photophysics on a optical resolution scale way below the diffraction limit. We applied this technique successfully to several further polymer blend films and small molecule organic semi conducting island films e.g. pentacene.

- Integrated tunneling current/shear-force feedback. In the section step, I have implemented a homebuilt STM/shear force function in our PM-SNOM. Since many years several groups tried to combine both techniques. But only a limited number of groups have achieved a working combination and only one further group could combine it with a PM. With this new system I could measure the Raman and PL-Spectra of three different molecules Benzotriazole (BTA), 2-Mercaptobenzothiazole (MBT) and 5-Chloro-2-Mercaptobenzothiazole (CL-MBT) with a spatial resolution of 4 nm. Furthermore I also demonstrate the dependence of these optical signals on the DC-electric field applied by the bias voltage.

- Bias voltage dependent TERS. All three types of the above mentioned molecules form self assembled monolayers (SAM) on smooth gold surfaces. According to our measurements and to the literature these molecules are standing upright on the surface and exhibit their benzene ring in the direction of the tip. All three examples show a reversible and significant interaction with the DC-field by varying the intensity and FWHM of specific Raman bands. Especially the bands associated with the benzene rings around 1580 cm^{-1} show a splitting in two bands and show a strong polarization dependence.

- Light amplification by an optical pumped tunneling junction. By further increasing the bias voltage above 1.5 V the PL emission from the tip-molecule-Au substrate junction is increasing in a stepwise manner by about one order of magnitude. We could show that this novel effect is driven by a process related to the stimulated emission of tunneling electrons. The optical enhancement has nonlinear dependencies on the applied bias voltage and on the optical pump power. Furthermore the amplification ct is closely related to the polarity of the molecules and follows the principles of Surface Plasmon Amplification by Stimulated Emission of Radiation (SPASER). We have done in depth experiments and have developed a model to explain the light amplification of an optically pumped molecular junction in a STM similar to a laser.

3. Technical Achievements

In this work a new optical path and a STM/shear-force-scanhead has been constructed and implemented. This achievement greatly improves the optical resolution and sensitivity of our PM-SNOM[53]. Moreover this system makes it possible to address and/or manipulate a few or even one single molecule in the tunneling junction by a DC electric field in the tip-sample gap. Through this function it is possible to enhance or to weaken specific Raman bands; especially the bands related to aromatic systems that are sensitive to the bias voltage.

3.1 Design and Construction of a STM-SNOM Function

The precise and stable positioning of the tip into the focus of the confocal microscope is the perquisite requirement for TERS-experiments. This can be achieved with different solutions. However, since in most systems the laser illumination path is fixed, one needs to move the tip itself into the laser focus. Although there are some groups working on a solution with laser scanning, this is not easy. Since the polarization of the incoming light is a crucial parameter for a proper excitation of the tip plasmon, the movement of the beam itself may induce systematic signal enhancement fluctuations due to the changes of the tip position with respect to the focus.

We use a two stage movement system (coarse and fine tuning) for aligning the tip into the focus, which we call tip runner. For both systems the movement is based on piezo ceramics. In total the runner has six agile axes. For the experiments performed in this thesis a completely new design of this system was required with an implemented STM-function. The important improvements of this design are a much higher stability and an internal damping. Both help to reduce mechanical oscillations and therefore allow for improving the feedback. In Fig. 3 i) a schematic of the runner on top of the microscope head is shown. The blue system of coordinates labels the 3D direction in space. The Fig. 3 ii) and iii) represent two photographs of the tip runner. The image ii) shows the very front end with the tuning fork and an attached gold tip, which is mounted on a four segmented piezo tube for fine adjustment and scanning, while picture iii) shows the whole system with its axial symmetry mounted on top of the PM microscope head. The beetle type runner can be either use in shear-force-, STM- or in a combined mode.
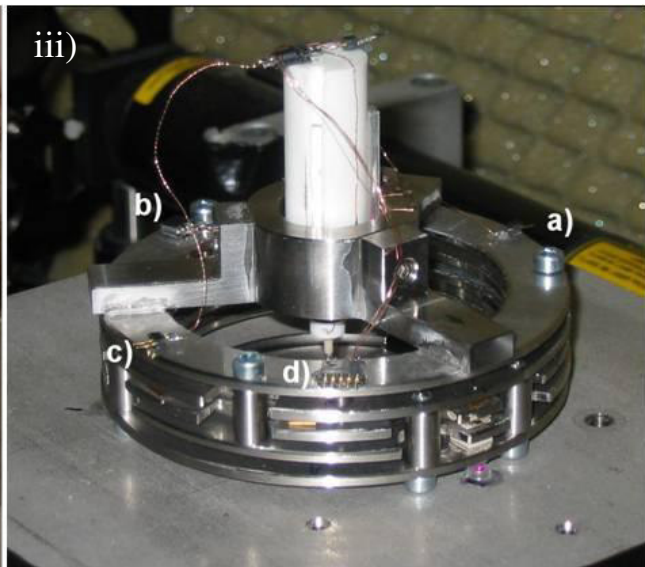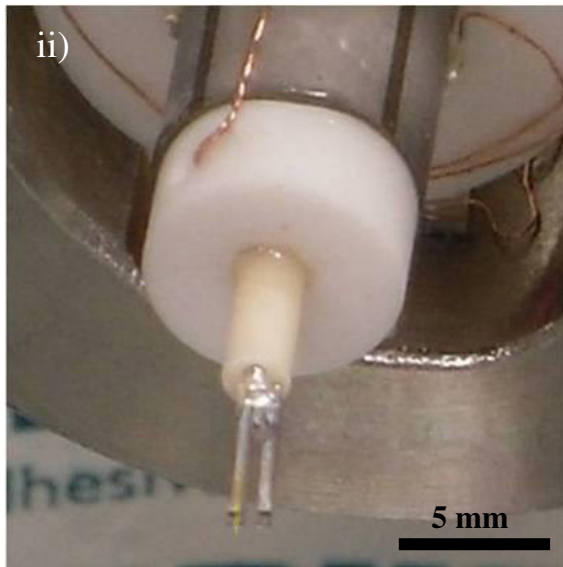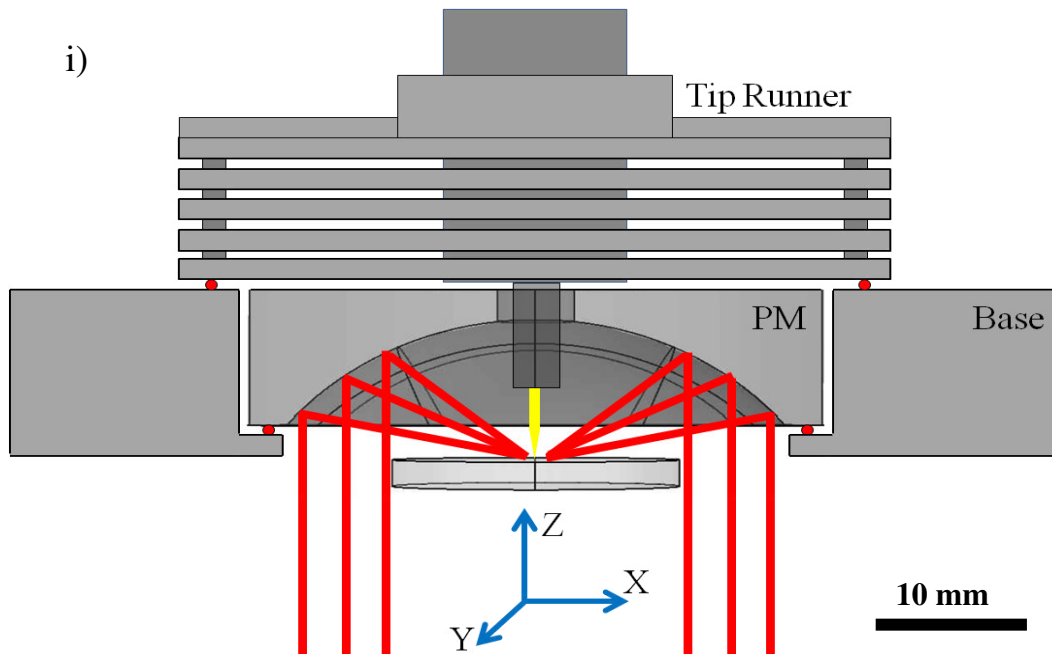
Fig. 3 i) Schematic of the microscope head with the tip runner on top of the base holding the tip into the focus of the PM. ii) Shows the tuning fork and an attached gold tip (left prong). The electrical connection is made via conductive glue (EPO-TEK EE120). iii) Photo of the whole tip runner with the connections (a) bias voltage, b) coarse positioning, c) tuning fork and d) piezo-tube for scanning and fine positioning.

The coarse stages can move the tip several millimeters in the (x,y,z)-direction and is used for a coarse approach. To achieve this we use three "slip-stick" motors. They consist of stacked piezo shear plates, which are driven with a saw tooth voltage signal. Through the flat rise of the signal the piezo bends slowly and the whole moving basis is pushed in the desired direction. This action is called the stick action. Then the signal is suddenly set back to zero and hence the piezo material contracts so fast that the mass of the runner cannot follow, giving rise to the slip action. After one cycle the system moves as much as the bending of the shear stacks. By varying the frequency the speed of travel can be controlled. The amplitude of

the saw tooth determines the step size and with this method a step size smaller than 100 nm can be achieved and at the same time, fast movement over a large range, up to 3 mm, is possible. A four segmented piezo tube is used to position the tip precisely into the focus. This tube has a resolution down to tens of picometers and also is used for tip-scanning. Furthermore, in the STM mode the tube is also used for adjusting the gap-width between the tip and the substrate to keep the tunneling current constant according to the feedback signal.

3.2 Spectroscopic Imaging

One major improvement, which was achieved during this work, is the full synchronization of the spectrograph with the scanning controller. The coupling itself is made via a TTL handshake signal processing. Different handshake modes are available, depending on the technical configurations of the used STM-controller and spectrograph. In our case a RHK SPM 1000 (controller) and an Acton 2300i Pro (spectrograph) with an attached Princeton Instruments SPEC-10 (CCD-camera) are combined. Normally the topography and the optical image (APD-based) are recorded with 256x256 pixels on an overall size between 200 – 1500 nm. On top of this we set a grid, a line or specific positions, where the scanner stops and directly starts the acquisition of the spectrum and afterwards goes on with the normal scanning. These different modes allow one to record topography and spectroscopic information in a synchronized manner using a minimum of time. These spectra can be easily analyzed individually, or plotted into an image using the intensity of the spectra and their corresponding position coordinates.

3.3 Implementation of a pulsed Laser-system and Fluorescence Lifetime Imaging

In a TERS experiment the tip is very close to the surface, any vibration brought to the decoupled setup leads to a crash of the tip. Hence no motor or hand driven optical attenuator is allowed to use during an experiment. Normally in TERS experiments a high average power is needed to shorten the integration time per spectrum. For further projects and measurements in between this work a picoseconds pulsed laser diode (Picoquant LDH D-C-640, with a wavelength of 634 nm and a pulse duration down to 100 ps) was implemented. This laser systems offer mainly two excellent advantages: 1) They allow for fast switching between

continuous wave (cw) and pulsed mode within seconds. Pulsed lasers offer high peak powers with rather low average power. This helps to avoid photo-bleaching on sensitive samples. In addition these lasers allow one to perform time resolved studies in the sub-nanosecond regime, e.g. fluorescence lifetime measurements or charge transfer effects. Hence the switching between cw and pulsed excitation offer high versatility. 2) In addition the power can be easily adjusted in both modes directly from the controller, which is very important for intensity dependent TERS-measurements. The main problem of these laser diodes is the rather poor beam quality. The beam has an elliptical intensity distribution and needs to be cleaned up into a Gaussian beam for direct use. Therefore the whole optics is rebuilt, by following the former design.

Together with the Laser diode the microscope has been upgraded with a time correlated single photon counting (TSSPC) unit (Picoquant Timeharp 200). With this extension it is possible to measure fluorescent lifetimes down to 100 ps and use a further imaging mode which is called fluorescent lifetime imaging (FLIM)[54]. A few proofs of concept measurements have been performed in the thesis work. In Fig. 4 such an experiment is shown, where we studied aggregated fluorescent beads and measured the intensity and the lifetime. The beads have a size of 80 nm and are coated with a fluorescent dye, which can be excited with a laser at 635 nm. The lifetime of the dye molecules is on the order of several nano seconds depending on the surrounding. Fig. 4a) shows the luminescence intensity of a glass sample covered with aggregates of fluorescent beads, while Fig. 4b) represents a fluorescent lifetime image of the same sample area.
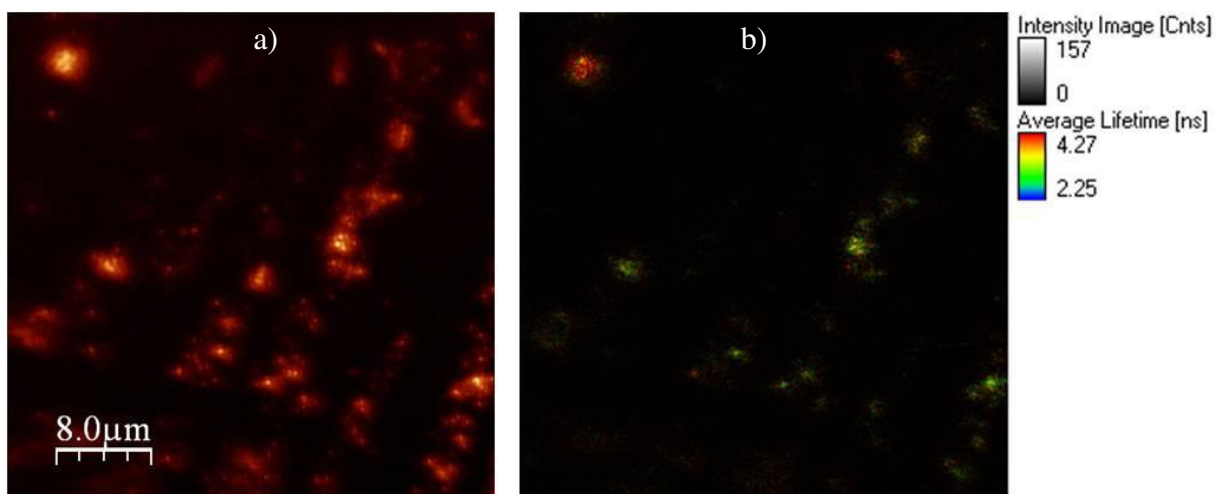

Fig. 4 a.) Fluorescence intensity of aggregated fluorescent beads imaged with an APD. b) Overlay of optical intensity (brightness) and lifetime (color-code). Both images are collected from the same position.

4. Experimental Results

4.1 Diindinoperylen film on Silicon

Diindinoperylen (DIP) and similar aromatic molecules with a large π-electronic system are prominent candidates for organic electronics. Hence the electronic and optical properties of material made of these molecules are of great interest and can be influenced by several ways of processing. It is important to note, that these properties deviade significantly from those of the monomer. Consequently there are studies on monomers, bulk crystals or amorphous phases or like in our case on thin films. These films are formed by controlled deposition and form a regular phase, which has various states of crystallinity[55]. Additionally the electronic and hence the optical properties of such films depend strongly on the local morphology, such as grain boundaries or localized defects[56,57].
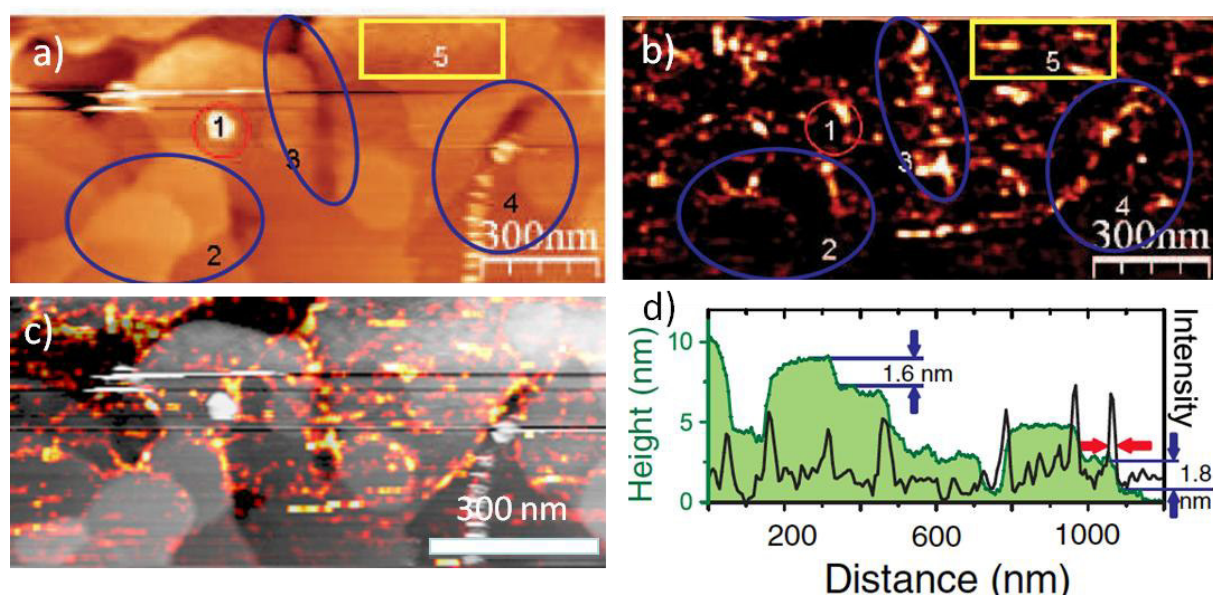

Fig. 5 (a) SNOM measurement of an organic semiconductor thin film consisting of domains of ordered DIP molecules showing the topography a) and the stokes shifted near-field optical image b). Laser power: 170 µW. Tip-sample distance: 3 nm. The topography shows clearly the flat molecular layers and terraces while the tip enhanced near field optical image shows bright lines all over the area. By overlapping the topographic and optical image c) the shining edge effect at the domain boundaries is clearly observed. In d) a line profile through the topographic image with its correlated optical intensity is displayed. Again the highest optical intensities occurred at the domain boundaries marked by the topography. Several steps which are marked with blue arrows show the height of a single molecular layers of 1.6 nm (green line).

These characteristics are well known to form the function in inorganic semiconducting devices. Thus thin molecular films are good model systems to gain further understanding of the interplay between the local morphology and the crystal structure and can lead to improved organic devices. Tip-enhanced near-field optical images Fig. 5b) and correlated topographic images Fig. 5a) of DIP on Si have been recorded. For image recording the etched Au-tip has

been parked in the focus, while the sample was scanned and kept at constant distance to the tip via a shear-force distance control based on a tuning fork. By checking carefully the optical image one can see that the dark regions are associated with the domains, while the bright lines follow nicely the grain boundaries. This can be further proven by overlaying a section of the optical and the topographic information [Fig. 5b)] and a comparison in the marked regions 2, 3, 4 and 5.
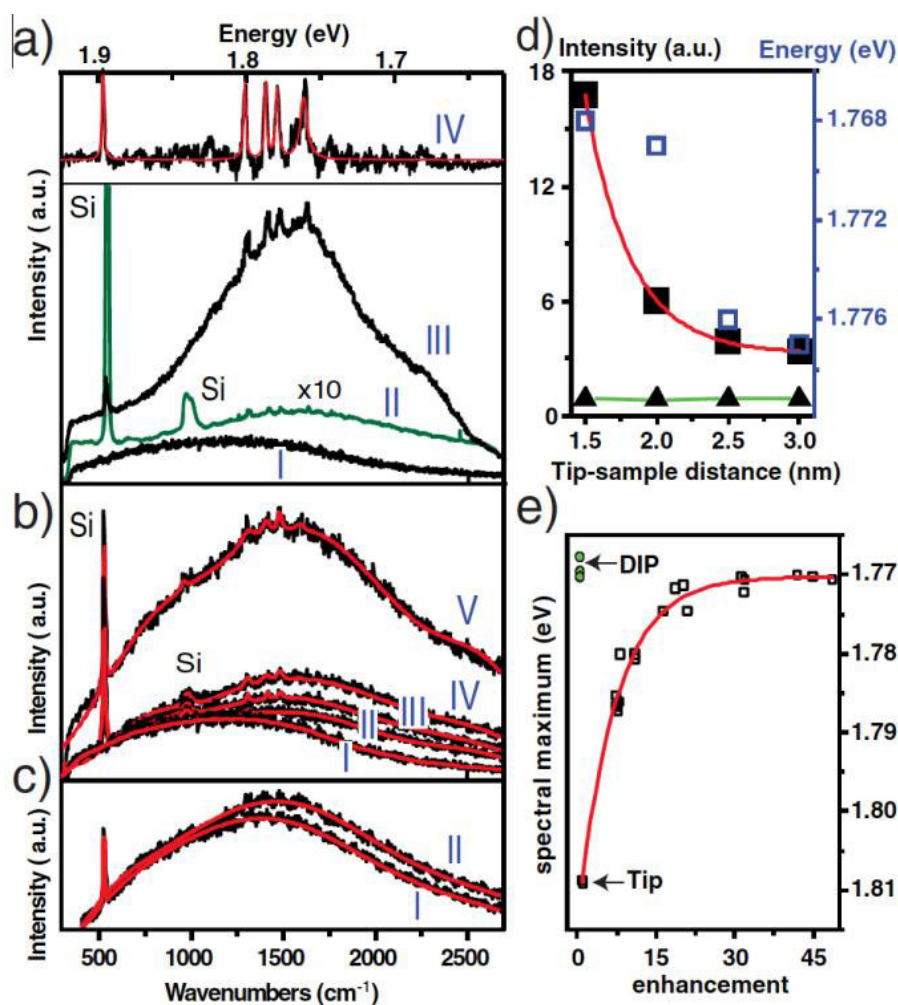

Fig. 6 a) Confocal far-field PL-spectrum (I) of a tip alone integrated for 10 s , (II) of DIP film integrated for 900 s, and (III) near-field spectrum integrated for 10 s at a gap width of 3 nm. (IV) TERS spectrum from (III) after PL-background subtraction with fitted Raman lines in red. (b) Spectra of the tip alone I and at different tip-sample distances. II, 3 nm; III, 2.5 nm; IV, 2 nm; V, 1.5 nm with an integration time of 10 s. (c) PL spectra, (I) from inside a domain and (II) from a domain edge. (d) Intensity of the Si Raman line (triangles), enhancement (closed squares), and energy shift (open squares) of the PL spectra as a function of tip-sample distance. (e) Energetic shift of the spectral maximum as a function of the total signal enhancement for different tips and days (empty squares). For comparison, the spectral maximum from the confocal far-field spectra of DIP are included (green circles).

The blue arrows in Fig. 5 d) mark a single molecular step (approx 1.5 nm) in the island film, while the red arrows mark the optical resolution, which is around 17 nm. Conventional optical confocal microscopy is not able to detect the increased luminescence at the grain boundaries, since the signal will always be averaged over the diffraction limited spot size. We have taken

tip enhance spectra at various points of interests. The spectra and the analysis are summarized in Fig. 6 and compared them also to a confocal spectrum. All spectra show the distinctive Raman bands of silicon at 520 cm^{-1}, except the spectrum from the tip itself [Fig. 6 a) and b) spectra I]. Beside the Si-bands no other Raman signal can be gathered in confocal mode and in TERS mode with a large gap size. When the tip is approached closer to the sample surface the PL is increasing [Fig. 6b) and d)] and finally with a distance of about 1.5 nm the corresponding ring breathing modes of the DIP at 1291 cm^{-1}, 1401 cm^{-1}, 1466 cm^{-1} and 1615 cm^{-1} appear [Fig. 6 a)]. This leaeds to a spectroscopic argument that the molecules are standing upright, which was already found in the topographic images and their measured step sizes. In the Confocal measurement the luminescence of the DIP film is very low due to quenching by the long range coupling of the π-electrons in the highly ordered thin film[58,59]. The situation changes dramatically when a tip is approaching the sample surface where at the closest tip-sample distance a maximum PL enhancement of about 6 x 10^5 has been achieved. Furthermore the maximum of the PL is red shifted upon approaching the tip to the surface, as expected in a gap mode. In the near-field optical image the brightest spots occur via the local radiative decay of excitons by exciton-plasmon coupling, which would decay nonradiatively without the presence of the tip. At the grain boundaries this coupling is stronger and hence the PL is further increased and shifted to lower energies.

4.2 STM-Raman Mapping

As a further example to demonstrate the optical performance of our microscope we show in the following a TERS mapping experiment from a self assembled monolayer (SAM) of 2-Mercapto-benzothiazole (MBT) on a smooth Au substrate MBT binds via the sulfur atom of the end-standing thiole-group to the Au surface, the first electronically excited state lies in the near UV, which is far away from our excitation laser (633 nm). Fig. 8 a) represents the sample topography with an area of 250 nm x 250 nm (100 mV bias voltage, I= 1nA) and a superimposed grid where every black dot marks the location where we have recorded one TERS spectrum.
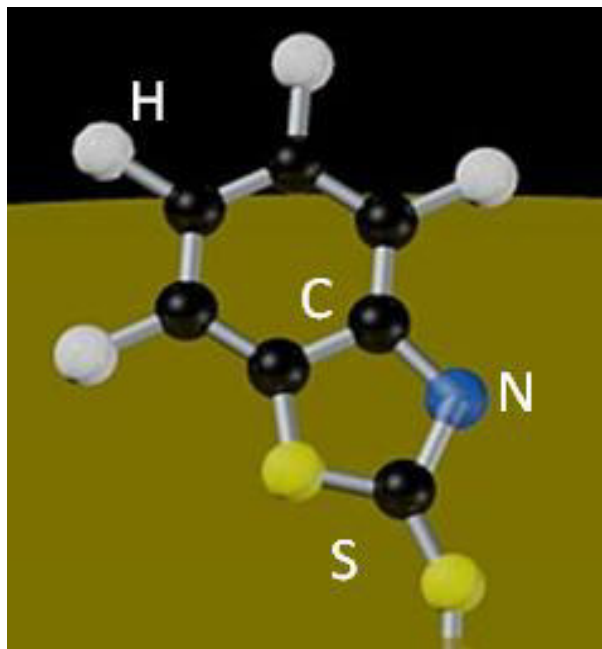

Fig. 7 Sketch of a MBT-molecule adsorbed on a smooth Au substrate

In contrast to the images presented in the last section the gap width was only on the order of 1 nm and can be controlled by the tunneling current between the tip and the conducting sample. Hence the tip-enhanced effect is stronger and reduces the acquisition time to 300 ms per spectrum. With a total of 64 x 64 spectra we are able to record 4096 spectra in less than half an hour. Fig. 8 b) is a two dimensional map of adjacent spectra in false color scale (red for high intensity, blue for low intensity), while Fig. 8 c) represent them in an expanded view. The spectra shown in Fig. 8 b) and c) are raw data with a good signal to noise ratio and show clearly the typical Raman bands of the MBT-molecule excited along the long molecular axis in excellent agreement with SERS-spectra known in the literature[60]. By comparing successive spectra recorded in one row with a separation of only 3.9 nm we clearly observe differences from one to the next spectrum such as intensity variations or splitting of individual lines. This behavior is reproducible and reflects local disorder in the film.
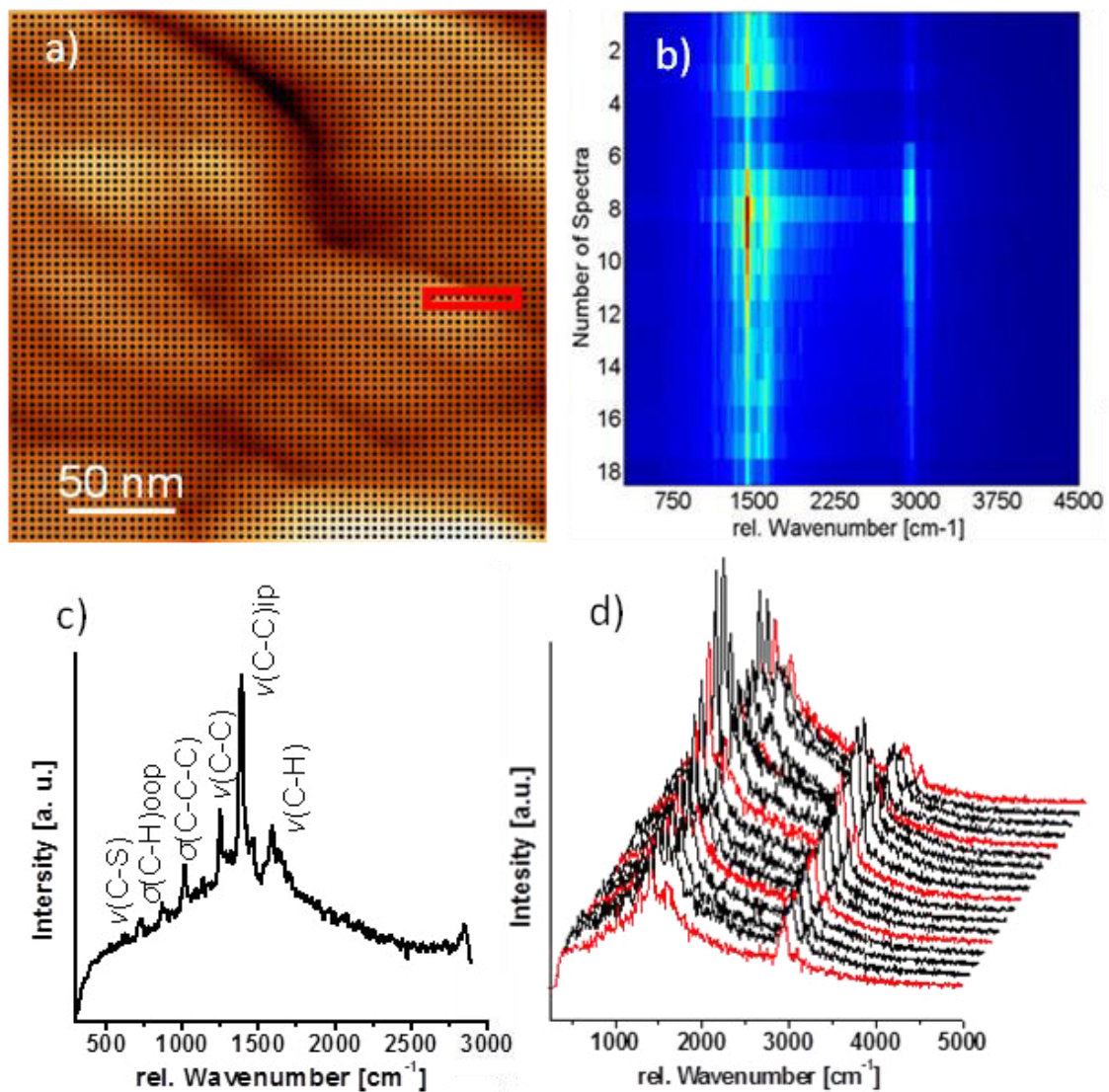
Fig. 8 Near-field measurement of a SAM of MBT on a smooth gold-film. In a) the topography and the superimposed spectral grid are shown. The red rectangle marks the region were the spectra where taken which are shown in b) and d). The single spectra are only separated less than 4 nm but still exhibit significant intensity variation.

4.3 Inelastic tunneling scattering

In contrast to the former and following experiments were for the excitation of the specimen a laser is used, this section is focusing on another approach based on tunneling electrons. The first observation of light emission by the so called inelastic tunneling (IET) process has been made in 1976 with a planar sandwich structure metal-insulator-metal device[61]. Upon applying a voltage between the two metal electrodes light emission from all over the junction could be observed. The authors suggest a model were inelastic tunneling electrons excite a surface plasmon, which can radiate by scattering at small surface protrusions. However already 1972 Young[62,63] proposed the IET-excitation in a junction formed by a tip and a sample, which was some years afterwards realized with the invention and further development of the STM[64,65]. The main advantage of this technique is the intrinsically ultra-high spatial resolution provided by the tunneling junction. This offers the possibility to directly address specific clusters, nanostructures and single molecules or even individual atoms. Fig. 9 shows a sketch of the potential energy diagram normally used for the theoretical description of a tunneling junction. In a
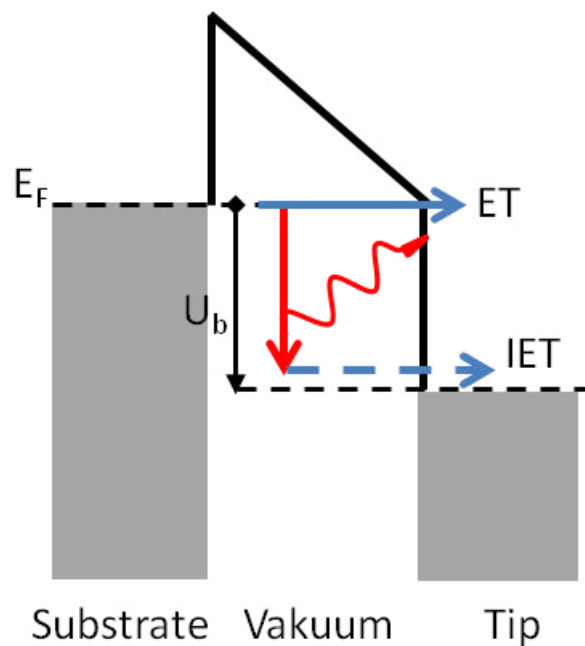
Fig. 9 Illustration of the energy diagram formed by a tunneling junction. The bias voltage lowers the Fermi-level of e.g. the tip and electrons tunnel either by elastic or inelastic fashion. The later one can excite a LSP between the tip and the sample via energy transfer.

tunneling process an electron can reach energy levels, which are contained in the junction. The electron can transfer energy to these levels, like for vibronic energy levels of molecules. This effect is employed in standard Scanning Tunneling Spectroscopy (STS)[66]. Normally the bias is only a few hundreds of mV suitable for exciting molecular vibrations, but if the bias is higher than 1.8 V the inelastically scattered electrons can launch processes, which are leading to a signal in the optical regime. Various junctions like metal-metal[64], or metal-molecule-metal[45] etc. have been studied. It has been shown that these experiments are able to provide an in-depth insight to molecular vibrations and allow one to address single molecules or even single chemical bonds[67]. In the first experiments pure metal junctions were used but within

the last decade people mainly focused on light emission from molecules, which are adsorbed on metal surfaces.

Due to the fact, that the IET can excite several SPP formed by the tip-sample junction, the material, size and shape of the tip has a strong influence on the resonance frequency and the strength of the emitted signal. It has been shown that noble metal tips have an up to one order of magnitude stronger signal than comparable tungsten tips.

Although most of the experiments aim at molecular luminescence, these systems prohibit intrinsically the light emission, since the physisorbed molecule is quenched due to the direct contact to the metal surface. Therefore people developed various decoupling methods, which still allow the forming of the gap mode in the tunneling junction. Probably the most efficient procedure is to introduce an ultra-thin decoupling layer of native oxid[68] onto the sample surface. However, also quite nice results have been achieved by the study of single molecules stacked on several monolayers[69]. These experiments provide chemical identification with a so far unmatched spatial resolution.

In our case working at ambient conditions we cannot achieve such high precision, but we can measure the effect itself and use it for later experiments as a reference.

Based on the experiments presented in Fig. 8 where we have recorded TERS-spectra of MBT-molecules in a tunneling junction, we have measured PL induced by inelastic tunneling on the same sample. In Fig. 10 we show an overview of PL spectra recorded from a tunneling junction consisting of an Au-tip and a smooth Au substrate covered with a SAM of MBT (tip-MBT-Au) as a function of the applied bias voltage. We have recorded several spectral series with positive and negative polarization (with reference to the tip) of the bias voltage. The first series Fig. 10 a) is taken at negative bias voltage. From -1400 mV a PL signal can be detected. Its intensity increases and shifts to higher energies at increasing bias voltage. After inverting the bias voltage we collect four spectra at specific voltages Fig. 10 c). In Fig. 10 b) the spectrally integrated intensities are displayed. While the spectra show comparable intensities and onset voltages, their shapes and energy ranges vary a lot.
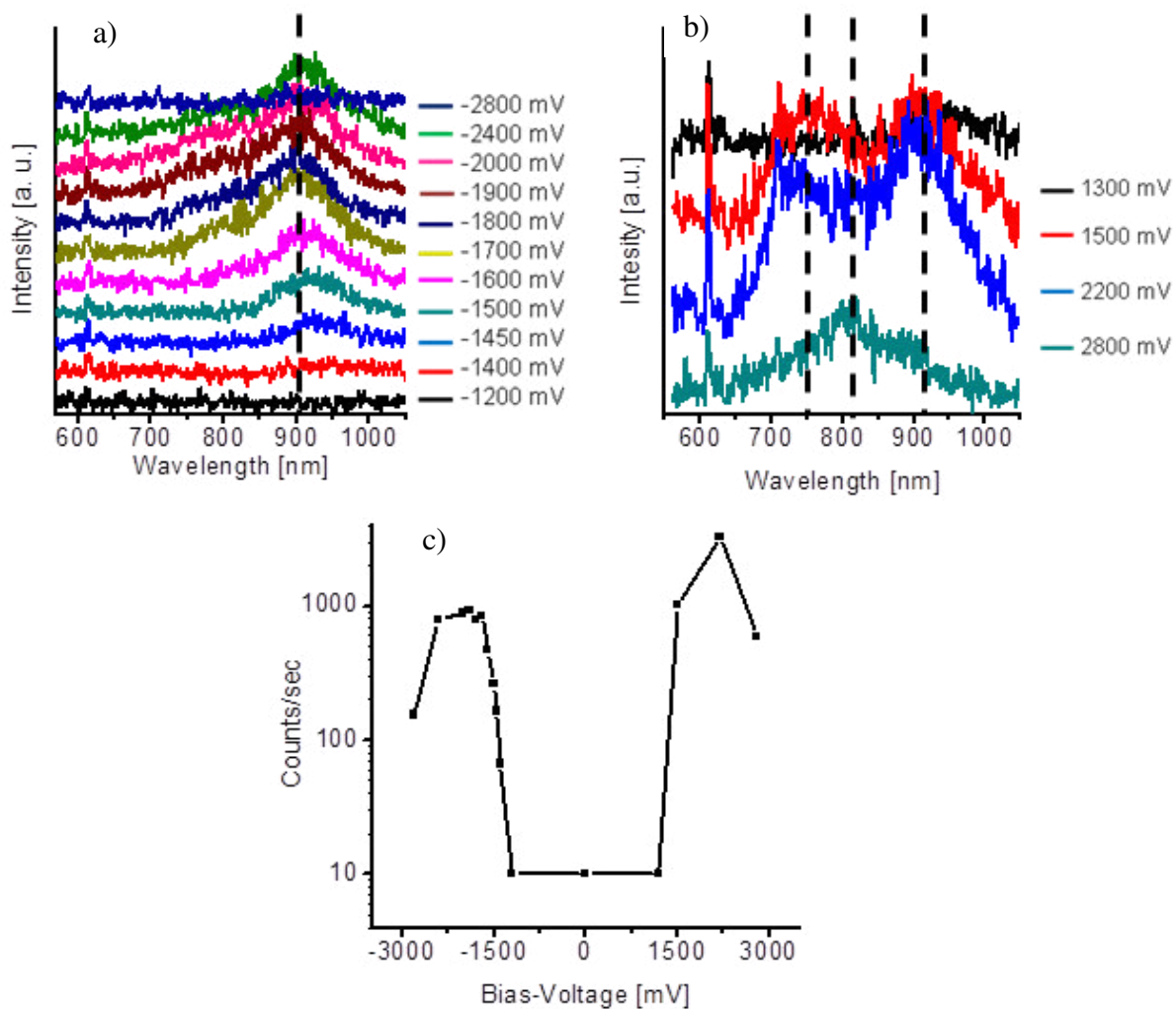
Fig. 10 a), b) PL-spectra from a monolayer film of 2-Mercaptobenzothiazole (MBT) molecules on a smooth Au substrate excited by inelastic tunneling for negative a) and positive b) bias voltage, respectively. (c) Spectrally integrated intensity.

The negative voltage leads to a single peak with a maximum of approx. 850 nm. In contrast at positive bias voltage a double peak with a maximum of 750 nm and 850 nm emerges. In principle with this measurement a coupled LSP from the surface and the tip are excited and the detected signals should be rather symmetric see Fig. 13 d). However we have studied a chemically modified surface. Therefore we expect an asymmetric junction, which is nicely represented in this measurement (compare Fig. 13 b).

4.4 STM TERS under varying electric fields by a Scanning Bias Voltage (SBV-TERS)

Using the tunneling current as a feedback signal allows us to precisely control the tip sample distance, even down to the angstrom regime. Hence (see section 1.3) strong plasmonic coupling inside a tip-substrate junction can be achieved, enabling high sensitivity and recording TERS-spectra with short integration times. In addition the STM implementation allows us to measure with strong, varying static (DC)-electric fields applied to the tip-sample gap, by controlling the bias voltage. Such a configuration is of great interest for investigating interfaces relevant for molecular (semiconductor) electronics. Of common interest in electronics is the reaction of the active component at the interface to the electrode as a function of the applied voltage. This situation can be obtained with a SAM of molecules on a metal surface in a tunneling junction, which can directly be studied with optical spectroscopy. This will be demonstrated here for three types of molecules (BTA, MBT and 5-Chloro-MBT see Fig 11).
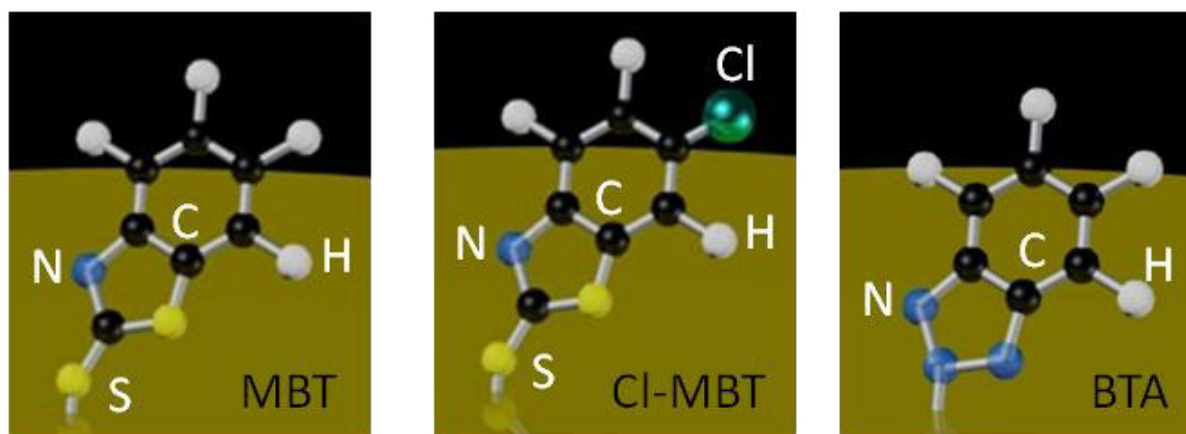

Fig. 11 Sktech of the chemical structures of the molecules MBT, Cl-MBT and BTA investigated by SBV-TERS. All three types consisting of an electrophile 5-ring with an annealed Benzene-ring.

They have comparable sizes and molecular structures, however different polarity, symmetries and hence electronic properties. All SBV-TERS experiments follow the same procedure, starting with s-SNOM images resolving the topography and a PL-image. According to the gathered information (surface roughness, optical contrast) the tip is parked stationarily over the sample surface at a point of interest while the bias voltage or the laser power is varied. The following experiments need to be divided into two voltage ranges, since they cover diverse effects from different origins. On the one hand a low voltage range, from -1.2 V to

+1.2 V, where small spectral changes are observed and a high voltage range, where dramatic spectral changes occur.

4.4.1 Low Bias Voltage TERS-Measurements

Beginning with the experiments with a bias voltage between 100-200 mV we observe TERS-spectra of MBT and BTA. By further increasing the bias voltage for both molecules several effects occur, which are associated mainly with the C=C stretching modes of the aromatic rings. The related peak is located at 1550-1620 cm^{-1}. For a practical analysis we discuss the molecules separately starting with BTA.
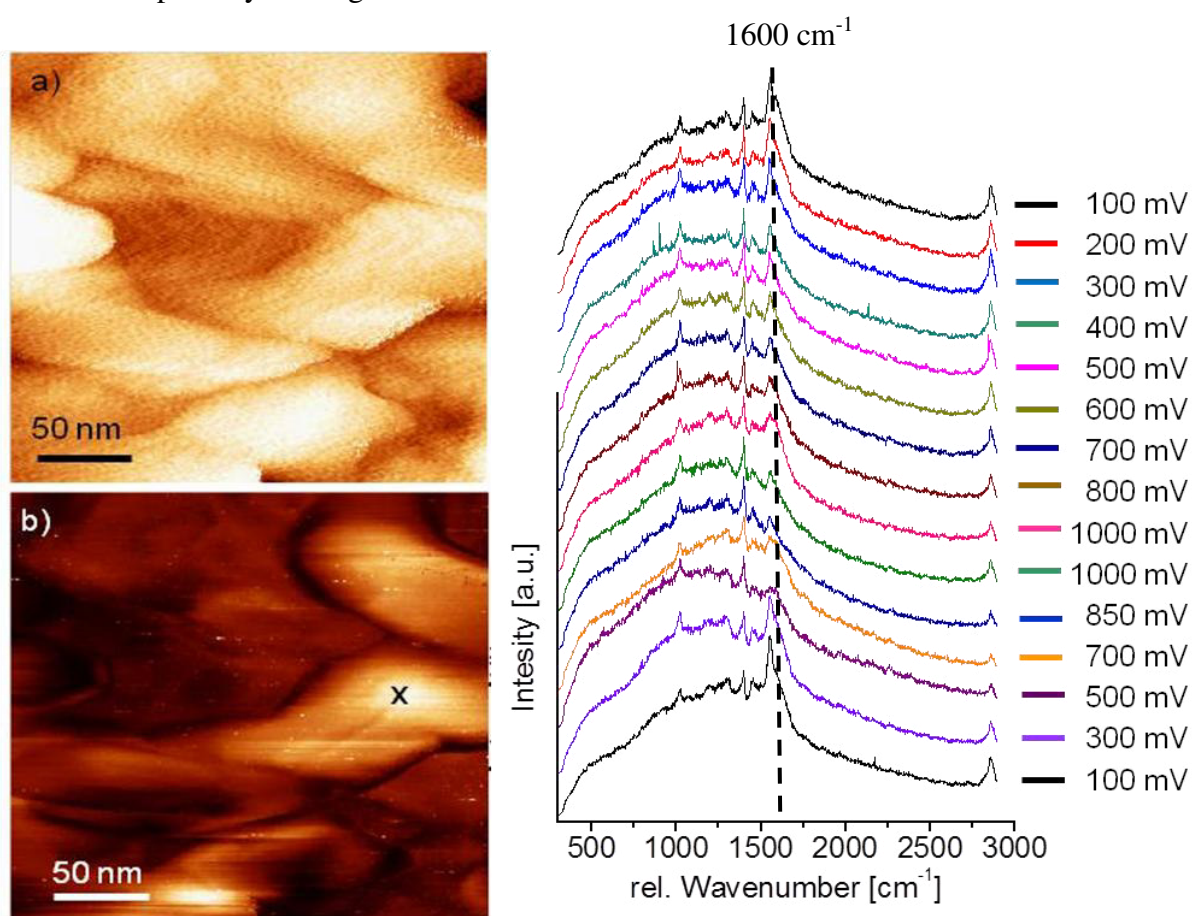

Fig. 12 Topography a) and tip enhanced PL b) images from a SAM of BTA on a smooth gold film. The spectral series shown in c) is taken at the marked x in picture b) The C=C stretching mode of the benzene ring at 1600 cm^{-1} is decreasing with an increase of the bias voltage.

The images in Fig. 12 show the results of a near-field experiment on a SAM of BTA prepared on a smooth gold film. The pictures a) and b) are from a standard tip enhanced near-field scan, showing the topography a) and the optical signal b) detected by an APD. In Fig. 12 c) a series of spectra is shown where the bias voltage is step-wise increased from 100 – 1000 mV and backwards. The spectra taken at specific voltages show a decrease of the Raman band at

~1600 cm^{-1} with increasing bias and are fully reversible by lowering the voltage back to 100 mV.

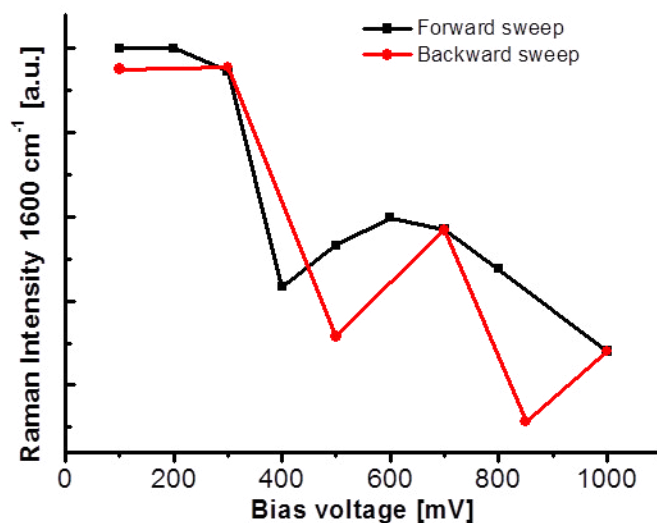Quite the opposite effect is observed when the same experiment is done for MBT. For positive bias voltages $|U_{bias}| \geq 800mV$ we observe a significant increase and broadening of the C=C stretching peaks of the Benzene-ring. Furthermore in the spectra at 900 and 1000 mV a clear splitting of the band is observed. In contrast to that, the line at 1375 cm^{-1} is decreasing
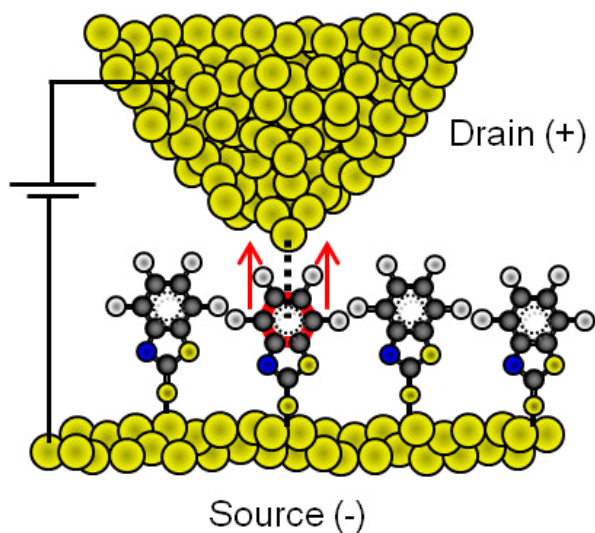
and other vibrations such as the σ−(C-C-C) band at 1100 cm^{-1} show a similar behavior. Additionally to the previous BTA study we have repeated the measurement with an inverse bias voltage. Interestingly for a negatively charged tip, the bias voltage has almost no effect. One obvious way to explain this behavior is that the polarizability tensor of the π-electron system of the molecule in the tunneling junction is influenced with higher bias voltages. This is suggesting that the negatively charged substrate leads to additional electron density on the surface bounded molecule, while a negative charged tip would not able to inject charges to the molecule itself (see example for MBT-molecules

Figure 14). Former studies in a conducting junction[52] have shown that mainly the Benzene-ring close to the tip apex is affected. The exact effect meaning the rise, shift or decrease of the Raman band of the Benzene is then not only dependent on the bias voltage itself but furthermore defined by the substituted functional groups or in our case by the annealed 5-ring.
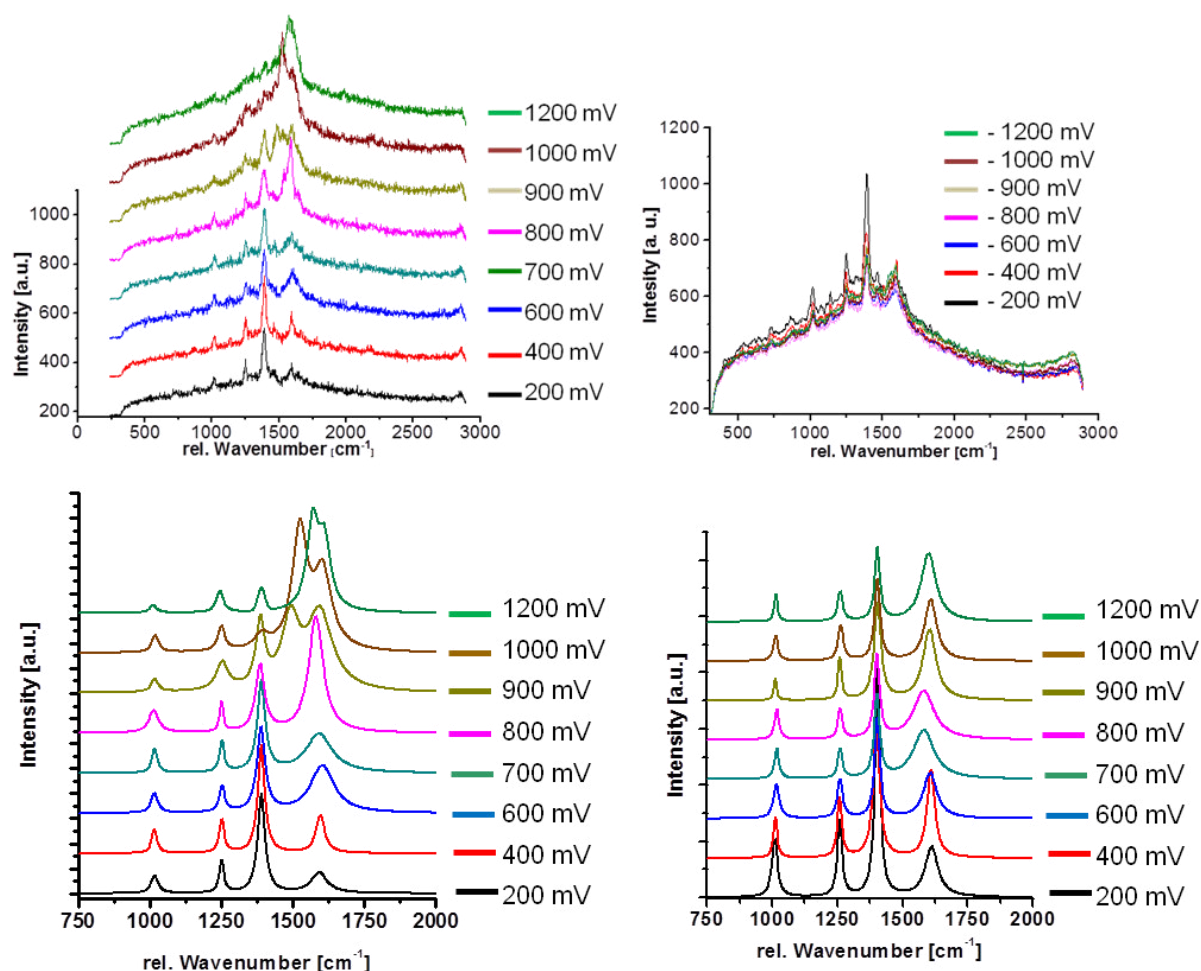
Fig. 15 (e), (f) Tip enhanced Raman spectra (with laser illumination) of MBT as a function of the applied bias voltage. At voltages > 600 mV we see a clear broadening and intensity increase of the 1620 cm^{-1} aromatic ring stretching mode and further ring modes occur. In contrast, for the reversed polarity we observe almost no effect. In c) and(d) the respective fitted Raman lines from a) and b) are shown.

The electronic properties of the 5-rings in MBT and BTA are quite opposite. The triazole in BTA acts chemically as base and therefore has a +Inductive-effect[70] and provides electron density to the annealed Benzene-ring, while the thiazole in MBT has an –Inductive-effect hence pulling electron density from the Benzene-ring. These two behaviors could explain the spectral differences, which are shown by these molecules as function to the increasing bias voltage in a straight forward way. A further detail, which needs to be taken into account, is the size of the enhanced near-field spot created by the optical antenna. Single-molecule experiments have shown[19,71] the strong enhancement provided by the tip. Nevertheless these

measurements were done in Ultra High Vacuum (UHV), or even at low temperatures. We studied SAMs under ambient condition. Hence very likely several molecules are excited by the incoming enhanced near-field, while only a single molecule at the time is affected by tunneling. This could explain the reported effects (increase, decrease and splitting of Raman-bands) in a two step process, where there is TERS from the molecules in the near-field and a varying TERS-signal from the molecules in the tunneling junction.

We want to note that this effect is fully reversible for both molecules and we are not aware that this has been described before. These are preliminary data indicating what kind of effects can be observed. Further measurements and an in depth analysis are beyond the scope of this thesis.

4.4.2 High voltage tunneling enhanced TERS

The formerly shown experiments offer already a great extend to the so far understood mechanism of TERS. Furthermore this effect can be used to enhance the resolution by addressing a molecules specific reaction on the chosen bias voltage. In the following experiments we will demonstrate an auxiliary effect, which can only be observed at higher bias voltages, in particular $U_b > 1.4$ V. We show that gap mode enhanced Raman scattering and luminescence emission from an STM junction consisting of an Au-molecules-Au junction can be enhanced by at least one order of magnitude. In addition this effect shows as well as the former experiment with MBT, a strong polarization dependency of the bias voltage. For both polarizations the intensity increases stepwise by overcoming a certain threshold voltage. In the full experiment is displayed. We have measured the bias dependent spectra for the Cl-MBT junction and a clean Au-Au junction. Furthermore we have collected the same data without illumination. For these experiments we used CL-MBT, since the additional chlor atom do not influence the chemical bonding to the surface, but will introduce a stronger polarizability of the benzene ring. The first electronic state is only accessible via UV light and cannot be excited by our laser wavelength of λ = 632.8 nm, which excludes direct luminescence from the molecule.

Common to all four situations presented in Fig. 16 and discussed above is that the bias voltage has to overcome a certain threshold before one can observe an enhancement of the TERS or PL signal (if the junctions are laser illuminated) or an enhancement of the luminescence induced by inelastic tunneling (if the laser is off). This threshold suggests that the energy levels of the surface-bound molecules and the density of electronic surface states of the Au substrate along with their relative alignment play a paramount role in ultraviolet photoelectron spectroscopy (UPS) measurements of a monolayer of Cl-MBT on Au reveal the energetic distribution of the HOMO of the surface-bound molecules with respect to the Fermi level of the Au surface at around (-1.5) – (-2.0) eV and the d-bands of Au below -2.0 eV. These energy ranges coincide with the bias for which we observe the step-like of the TERS signal and the laser-induced Au luminescence signal. First we consider light emission induced by tunneling without laser irradiation. For low bias voltage the emitted light originates predominantly from the radiative decay of localized surface plasmons excited by inelastic electron tunneling. When $U_b \geq 1500$ mV we note that electrons can in addition elastically) tunnel from the HOMO of the surface-bound molecules (at -1.5 – 2.0 eV) to the positively charged tip, leaving a holes behind in the outmost orbitals respective molecules. Electrons

from the metal can subsequently recombine with those holes. A recombination involving electrons near the Fermi energy will result in the emission of a photon with the excess energy. This process explains the PL band at around 775 nm observed for a bias voltage of 1800 mV (blue spectrum in Fig. 16b). When the bias voltage is further increased, also electrons from surface orbitals of the d-band can tunnel elastically to the tip, giving rise to holes.
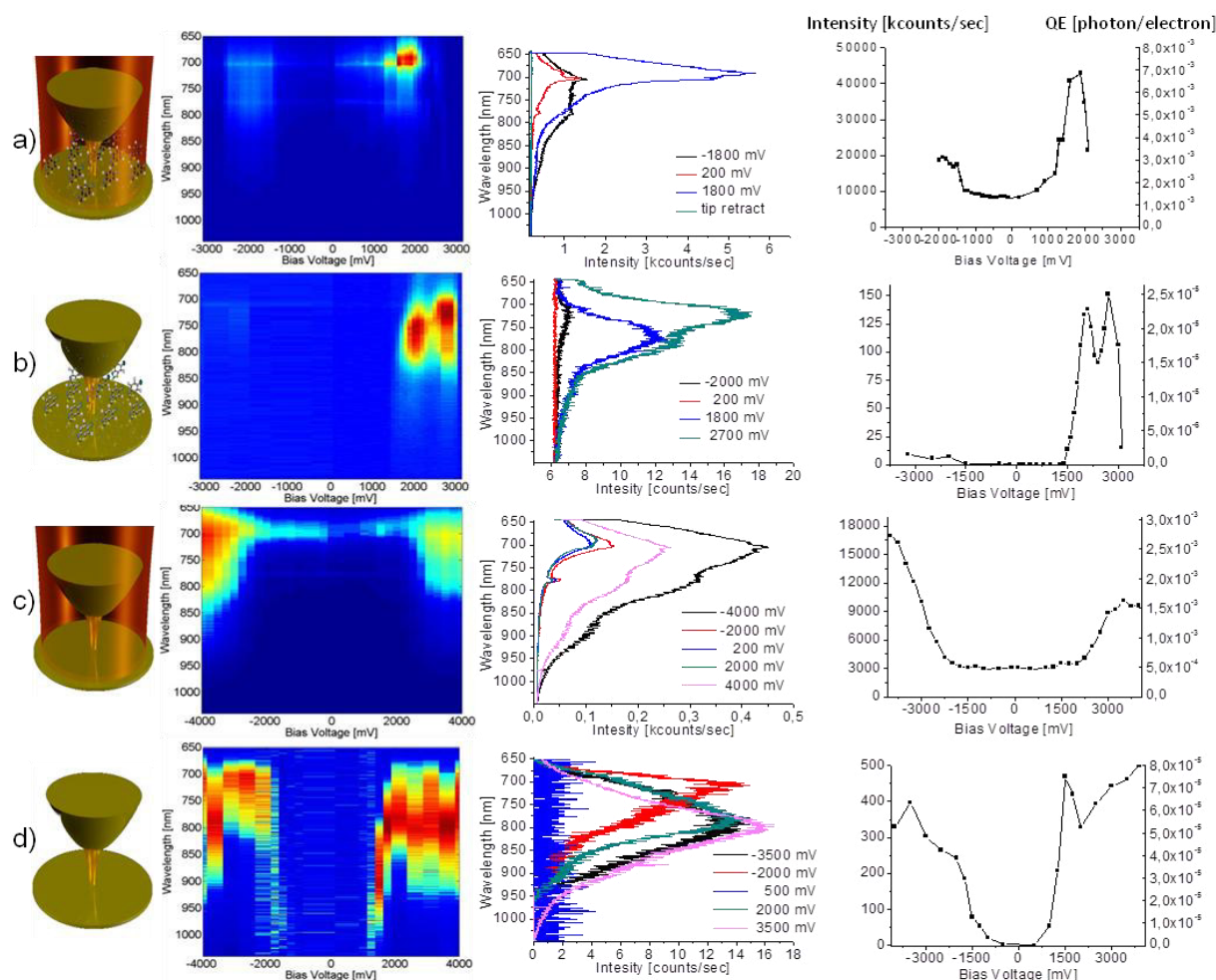

Fig. 16 a) Tip-enhanced light emission spectra, optically excited at λ = 632.8 nm, as a function of the bias voltage, taken from an Au substrate covered with a monolayer of Cl-MBT molecules (left), spectrally integrated intensity trajectory (right) and sample spectra recorded at different bias voltages (center). Spectra were recorded successively at the same sample position with different positive and negative bias voltages ("positive" means "positive tip"). The numbers next to the spectra indicate the voltages at which the spectra were obtained. (b) Luminescence spectra excited by inelastic tunneling without laser illumination as a function of the bias-voltage. (c) Tip-enhanced photoluminescence spectra for a Au-sample/Au-tip junction optically excited at λ = 632.8 nm and (d) luminescence spectra excited by inelastic tunneling without laser illumination as a function of the bias voltage. All spectra were recorded with the same tunneling current, therefore the corresponding quantum efficiencies (QEs) are calculated for a tunneling current of 1 nA and are normalized to 1s integration time. In panels (a) and (c) the laser power at the sample was 250 μW.

The subsequent recombination with electrons is the source of the blue-shifted band at 725 nm (green spectrum in Fig. 16b). If the bias voltage is inverted, i.e. if the tip is (negative and the sample is positive we observe only a very weak PL signal. Obviously electron-hole formation and radiative recombination is hindered by the inverted polarity. In contrast, for a bare Au/Au

junction the tunneling-induced luminescence is only weakly polarity-dependent and differences between both polarities could be explained due to the geometrical difference between the tip apex and the substrate surface. Hence we conclude that electron-hole formation and radiative recombination occurs very localized in those few surface-bound molecules that form a tunneling junction between the substrate and the tip. .

Illuminating the tip/sample junction with a focused laser beam polarized along the tip axis leads to a coupled surface plasmon oscillation in the tip and the underlying sample surface that manifests itself as a highly localized surface charge oscillation at the tip apex and the Au surface forming the cavity, which are coupled by their optical near field. Recently, it has been shown that plasmon-excited nanoparticles can be an efficient source of hot electrons. Each surface plasmon quantum can either decay into a photon or into an electron-hole pair (EHP) that can recombine under em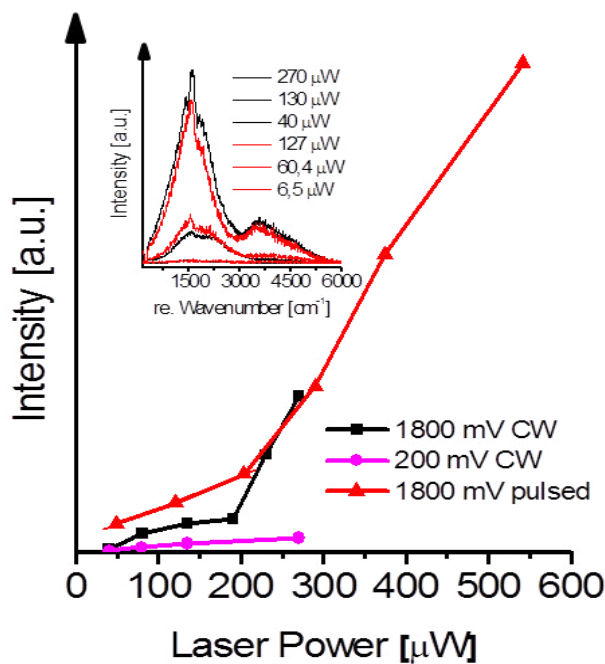ission of a luminescence photon. In an Au-Au junction luminescence emission occurs most efficiently from the very tip apex and the opposing substrate area, where the oscillating surface charges create the highest field strength. The luminescence spectrum of the bare Au-Au junction recorded at zero bias shows that radiative recombination of EHP is most efficient for hot electrons that are excited from near the Fermi level, leading to well-known Au luminescence[72] (Fig. 16c), while hot electrons close to the Fermi level relax thermally. The situation changes if the bias voltage is high enough to create holes in the d-band by elastic tunneling. In this case, also the hot electrons with energy close to

Fig. 17 Integrated Stokes-shifted emission intensity as a function of the incident laser power for continuous-wave (CW) and pulsed illumination. In both cases, a distinct threshold can be seen separating a low-gain regime at low laser powers from a high-gain regime at higher laser powers. Inset shows the spectrally resolved emission intensity at various CW (black curves) and pulsed (red curves) laser powers.

the Fermi level decay radiatively, leading to the step-like increase in the luminescence intensity by an order of magnitude when the bias voltage passes the energy of the d-band at approximately 2000 mV. New studies of very small gaps (< 1 nm) and nearly touching nanoparticles show that an upper limit is imposed to the field enhancement in the gap by the intrinsic nonlocality of the dielectric response of the metal and the tunneling of the plasmon-excited electrons through the gap. In our experiments, the confinement limit of electron

tunneling and electron-hole recombination is defined by the surface bound individual molecules.

The nonlinear increase of the emission intensity with increasing laser power is typical for a system where a feedback process is taking place, directing a portion of the amplified Raman and PL emission back towards the substrate/molecule hybrid system. Considering the fact that the Raman scattering and PL emission processes originate in the very center of the tip/substrate gap, any generated photon will first couple to the gap mode before being scattered to the far field. While the gap mode's plasmon resonance is very broad, exhibiting a quality factor of only, the resonantly stored energy is extremely well localized spatially, in a volume having an upper limit of approximately 4x4x1 nm³. Thus, the feedback of the emitted energy back to the quantum system is very efficient, still. A stimulation of the radiative decay of hot electrons into the molecule's HOMO level explains the nonlinear intensity increase as indicated by the additional emission process (4) in Fig. 18. The optical system comprising the gap mode and the substrate/molecule hybrid system is reminiscent of a novel nanoscale laser, containing an extremely fast optical gain material exhibiting a population inversion, i.e. the hot-electron recombination of the molecule's HOMO level, bi-directionally coupled to a resonator, i.e. the plasmonic gap mode. In this case, population inversion and thus gain is expected under the very conditions
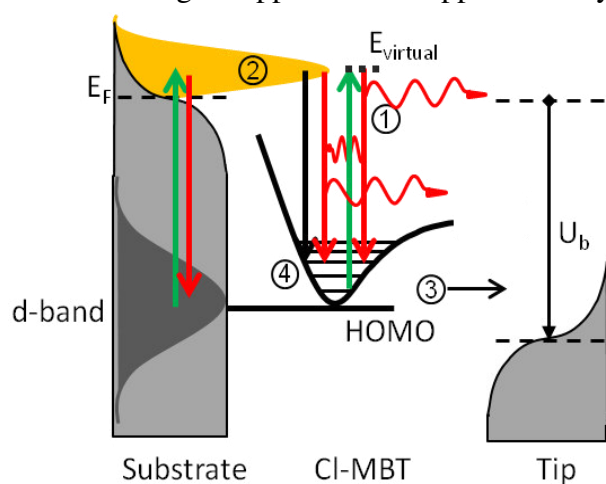

Fig. 18 Schematic energy level diagram of the molecule/gap hybrid system in a laser-illuminated molecular tunneling junction of an STM. Green arrows denote processes drawing energy from the incident laser field and red arrows represent emission processes. The incident radiation leads to (1) Raman scattering form the surface bound molecules and (2) generates hot surface electrons with a non-thermal distribution indicated in yellow. Nonradiative processes are indicated by black arrows, e.g. inelastic tunneling of electrons from the molecules HOMO levels to the tip (3) when the Fermi-level of the tip falls below the HOMO-level of the closest surface-bound molecules and nonradiative recombination of hot electrons (4) with holes in the molecules repopulating the HOMO levels.

for which enhanced emission can be observed experimentally: depletion of the HOMO via elastic tunneling to the tip and generation of hot electrons by irradiating the plasmonic system with incident laser light. TERS scattering from neighboring molecules acts as an optical seed signal in the cavity mode and is amplified in the molecular tunneling junction by stimulated emission from hot electrons recombining with holes in the surface-bound molecules. This leads to the spectral narrowing of the amplified signal (Fig. 12b) in the metal-molecule-metal

junction for a positive bias voltage above threshold. For a negative bias voltage electrons can tunnel directly from the tip to the metal substrate without the creation of holes in the HOMO-level of the surface bound molecules. In this case the molecules rather form a thin insolating layer hindering light emission from inelastic tunneling.

Having understood the individual processes one can attempt to describe the behavior of the Au/Cl-MBT/Au junction in an energy level scheme as represented in Fig.18 Green arrows represent processes drawing energy from the incident pump-laser field such as, i.e. Raman scattering from the surface-bound molecules (1) and generation of hot electrons from the d-band leading to Au-luminescence when the recombine with the respective holes (2). Plasmon excitation is not shown in this figure. When the Fermi level of the tip drops below the HOMO energy of the surface-bound molecules, elastic electron tunneling from the molecules to the tip occurs (3) and), leaving holes in those molecules. These holes can now be refilled by a hot surface-electrons from the Au substrate (4), emitting photons which can be observed by the detector. The rate of this additional optical process depends on the local density of hot surface electrons which is a function of the incident laser power, and the tunneling rate from the HOMO to the tip which is a function of the bias voltage. The observed dependence on the incident laser power as shown in Fig. 17 exhibits a distinct nonlinear behavior with a threshold separating a low gain regime at low laser powers from a high gain regime at higher powers. for continuous-wave (CW) and pulsed excitation (pulse length 100 ps, 80 MHz repetition rate) Both curves show the nonlinear onset at comparable power and have the same slope in the high gain regime when we plot the curve for pulsed excitation as a function of the cw-equivalent power (see suppl.), indicating that on the time scale of 100 ps the system has reached stationary conditions, which is expected for relaxation times of plasmon oscillations being on the order of 100 fs and below. The respective spectra show that both the Raman lines around 1600 cm^{-1} and the luminescence background are enhanced. At higher powers, an additional plasmonic luminescence band appears at 3700 cm^{-1}.

5. Conclusion and Outlook

During my PhD work a variety of technical developments are achieved. New functions, such as Hyperspectroscopic imaging, STM, FLIM and SBV-TERS are implemented. The target systems range from monolayers of small molecules to organic blend films. The knowledge obtained provides in-depth understanding of the optical, photo- physical –chemical as well as photo-electric properties of organic materials and molecule metal interfaces. We have discovered novel luminescence properties of semiconducting molecular films, were the tip is not only used for enhancing the excitation but also acts as an antenna for enhanced emission. Furthermore, the new functions integrated homebuilt microscope enables in some substances the unique opportunity to study complicated systems like polymers, blends and electrode/active layer interfaces. Until now there have only little possibilities to study this type of samples and most of them have been limited by the optical resolution. With the newly develop system the resolution could be increase by more than one order of magnitude. In particular, the collective influences from electrical and optical manipulation of (single) small molecules in a nanometer-sized near-field gap established in a tunneling junction. The first successful experiments show fascinating results and so far unexploited possibilities to study photo effects. In addition the superluminescence experiments show a truly new pathway of photon-emission, were the lowest unoccupied molecular orbital is bypassed. This could lead to ultra stable and ultra small photon sources working millions of cycles even in ambient conditions, since photo bleaching is effective avoided.

Recently several well-known big manufacturers such as Bruker have jumped into the market and are offering commercial TERS-microscopes. For the SPM part they offer a large variety of options like AFM and/or STM tip feedback as well as shear-force sensors. The most straight forward design is to combine the SPM unit with a commercial inverted confocal microscope Few TERS products work with side illumination or top illumination mode. Growing interests in the research field of SNOM/TERS are witnessed. This microscopes deliver nanometer scaled optical resolution and single molecule sensitivity in terms of fingerprint vibrational spectroscopy. The big advantage by still developing and building own systems is motivated by the freedom to choose what is needed e.g. laser systems, special laser polarizations (CVBs) etc.

To further optimize the performance of our homebuilt multi-functional setup, in the next steps the following aspects will be aimed at:

1) Transfer of the system into an ultra high vacuum (UHV) chamber. So far the optical microscope works at ambient condition for the sake of easy adjustment and convenient testing of new measuring modes. As the new functions of the microscope getting optimized, a big part of the system, at least the microscope head with the sample stage, the STM and the PM will be integrated with UHV techniques. The obvious benefits will be a clean environment and a much higher photo-stability of the sample, which are extremely essential to apply our technique in general surface science.

2) Combination with a cryogenic system. To study or to manipulate the molecular behavior on a single molecule level, varieties of influencing factors have to be considered, such as thermal drifts, surface diffusions, decompositions etc. Working at low temperatures will inevitably help to minimize such influences and enable single molecule imaging combined with SNOM/TERS research.

Thus we would like to use our knowledge to copy the system and rebuild it in UHV and combine it also directly with helium cooled cryogenic system. A further interesting research direction is given by molecules, which are resonant with the used laser wavelength. Here we expect even stronger influences to the bias voltage, since already simultaneous excited states are accessible and maybe leading to pump probe type measurements. But we will also continue with the ambient conditions experiments, which are closer to the real applications.

6. Literature

1   Pohl, D. W., Denk, W. & Lanz, M. Optical stethoscopy: Image recording with resolution lambda/20. *Appl. Phys. Lett.* **44**, 651-653, (1984).
2   Maiman, T. H. Stimulated Optical Radiation in Ruby. *Nature* **187**, 493-494, (1960).
3   Inouye, Y. & Kawata, S. Near-field scanning optical microscope with a metallic probetip. *Opt. Lett.* **19**, 159-161, (1994).
4   Stockle, R. M., Suh, Y. D., Deckert, V. & Zenobi, R. Nanoscale chemical analysis by tip-enhanced Raman spectroscopy. *Chem. Phys. Lett.* **318**, 131-136, (2000).
5   Betzig, E. *et al.* Imaging Intracellular Fluorescent Proteins at Nanometer Resolution. *Science* **313**, 1642-1645, (2006).
6   Rust, M. J., Bates, M. & Zhuang, X. Sub-diffraction-limit imaging by stochastic optical reconstruction microscopy (STORM). *Nat Meth* **3**, 793-796, (2006).
7   Hell, S. W. Far-Field Optical Nanoscopy. *Science* **316**, 1153-1158, (2007).
8   Hell, S. W. & Wichmann, J. Breaking the diffraction resolution limit by stimulated emission: stimulated-emission-depletion fluorescence microscopy. *Opt. Lett.* **19**, 780-782, (1994).
9   Klar, T. A. & Hell, S. W. Subdiffraction resolution in far-field fluorescence microscopy. *Opt. Lett.* **24**, 954-956, (1999).
10   Gustafsson, M. G. L. Nonlinear structured-illumination microscopy: Wide-field fluorescence imaging with theoretically unlimited resolution. *PNAS* **102**, 13081-13086, (2005).
11   Fleischmann, M., Hendra, P. J. & McQuillan, A. J. Raman spectra of pyridine adsorbed at a silver electrode. *Chem. Phys. Lett.* **26**, 163-166, (1974).
12   Brongersma, M. L. & Shalaev, V. M. The Case for Plasmonics. *Science* **328**, 440-441, (2010).
13   Kneipp, K. *et al.* Single Molecule Detection Using Surface-Enhanced Raman Scattering (SERS). *Phys. Rev. Lett.* **78**, 1667-1670, (1997).
14   Ren, B., Picardi, G. & Pettinger, B. Preparation of gold tips suitable for tip-enhanced Raman spectroscopy and light emission by electrochemical etching. *Rev. Sci. Instrum.* **75**, 837-841, (2004).
15   Quabis, S., Dorn, R., Müller, J., Rurimo, G. K. & Leuchs, G. in *Conference on Lasers and Electro-Optics/International Quantum Electronics Conference and Photonic Applications Systems Technologies.* IWG3 (Optical Society of America).
16   Pettinger, B., Domke, K. F., Zhang, D., Picardi, G. & Schuster, R. Tip-enhanced Raman scattering: Influence of the tip-surface geometry on optical resonance and enhancement. *Surf. Sci.* **603**, 1335-1341, (2009).
17   Pettinger, B., Domke, K. F., Zhang, D., Schuster, R. & Ertl, G. Direct monitoring of plasmon resonances in a tip-surface gap of varying width. *Phys. Rev. B* **76**, (2007).
18   Kurouski, D., Deckert-Gaudig, T., Deckert, V. & Lednev, I. K. Structure and Composition of Insulin Fibril Surfaces Probed by TERS. *J. Am. Chem. Soc.* **134**, 13323-13329, (2012).
19   Zhang, R. *et al.* Chemical mapping of a single molecule by plasmon-enhanced Raman scattering. *Nature* **498**, 82-86, (2013).
20   Bailo, E. & Deckert, V. Tip-enhanced Raman spectroscopy of single RNA strands: Towards a novel direct-sequencing method. *Angew. Chem. Int. Edit.* **47**, 1658-1661, (2008).
21   Hartschuh, A., Pedrosa, H. N., Novotny, L. & Krauss, T. D. Simultaneous Fluorescence and Raman Scattering from Single Carbon Nanotubes. *Science* **301**, 1354-1356, (2003).

22 Hayazawa, N., Inouye, Y., Sekkat, Z. & Kawata, S. Near-field Raman scattering enhanced by a metallized tip. *Chem. Phys. Lett.* **335**, 369-374, (2001).

23 Pettinger, B., Ren, B., Picardi, G., Schuster, R. & Ertl, G. Nanoscale Probing of Adsorbed Species by Tip-Enhanced Raman Spectroscopy. *Phys. Rev. Lett.* **92**, 096101, (2004).

24 Lieb, M. A. & Meixner, A. J. A high numerical aperture parabolic mirror as imaging device for confocal microscopy. *Opt. Express* **8**, 458-474, (2001).

25 Stadler, J., Stanciu, C., Stupperich, C. & Meixner, A. J. Tighter focusing with a parabolic mirror. *Opt. Lett.* **33**, 681-683, (2008).

26 Frey, H. G., Witt, S., Felderer, K. & Guckenberger, R. High-Resolution Imaging of Single Fluorescent Molecules with the Optical Near-Field of a Metal Tip. *Phys. Rev. Lett.* **93**, 200801, (2004).

27 Neacsu, C. C., Dreyer, J., Behr, N. & Raschke, M. B. Scanning-probe Raman spectroscopy with single-molecule sensitivity. *Phys. Rev. B* **73**, 193406, (2006).

28 Zhang, W., Yeo, B. S., Schmid, T. & Zenobi, R. Single Molecule Tip-Enhanced Raman Spectroscopy with Silver Tips. *J. Phys. Chem. C* **111**, 1733-1738, (2007).

29 Martin, O. J. F. & Girard, C. Controlling and tuning strong optical field gradients at a local probe microscope tip apex. *Appl. Phys. Lett.* **70**, 705-707, (1997).

30 Martin, Y. C., Hamann, H. F. & Wickramasinghe, H. K. Strength of the electric field in apertureless near-field optical microscopy. *J. Appl. Phys.* **89**, 5774-5778, (2001).

31 Novotny, L., Sánchez, E. J. & Sunney Xie, X. Near-field optical imaging using metal tips illuminated by higher-order Hermite–Gaussian beams. *Ultramicroscopy* **71**, 21-29, (1998).

32 Pettinger, B., Picardi, G., Schuster, R. & Ertl, G. Surface-enhanced and STM tip-enhanced Raman spectroscopy of CN− ions at gold surfaces. *J. Electroanal. Chem.* **554–555**, 293-299, (2003).

33 Karrai, K. & Grober, R. D. Piezoelectric tip-sample distance control for near field optical microscopes. *Appl. Phys. Lett.* **66**, 1842-1844, (1995).

34 Hartschuh, A., Anderson, N. & Novotny, L. Near-field Raman spectroscopy using a sharp metal tip. *J. of Microsc-Oxford* **210**, 234-240, (2003).

35 Deckert-Gaudig, T., Kämmer, E. & Deckert, V. Tracking of nanoscale structural variations on a single amyloid fibril with tip-enhanced Raman scattering. *J.f Biophotonics* **5**, 215-219, (2012).

36 van Schrojenstein Lantman, E. M., Deckert-Gaudig, T., Mank, A. J. G., Deckert, V. & Weckhuysen, B. M. Catalytic processes monitored at the nanoscale with tip-enhanced Raman spectroscopy. *Nat Nano* **7**, 583-586, (2012).

37 Pahlow, S. *et al.* Bioanalytical application of surface- and tip-enhanced Raman spectroscopy. *Eng. Life Sc.* **12**, 131-143, (2012).

38 Huber, A. J., Kazantsev, D., Keilmann, F., Wittborn, J. & Hillenbrand, R. Simultaneous IR Material Recognition and Conductivity Mapping by Nanoscale Near-Field Microscopy. *Adv. Mater.* **19**, 2209-2212, (2007).

39 Stadler, J., Schmid, T. & Zenobi, R. Nanoscale Chemical Imaging Using Top-Illumination Tip-Enhanced Raman Spectroscopy. *Nano Lett.* **10**, 4514-4520, (2010).

40 Wang, X. *et al.* High-Resolution Spectroscopic Mapping of the Chemical Contrast from Nanometer Domains in P3HT:PCBM Organic Blend Films for Solar-Cell Applications. *Adv. Funct. Mater.* **20**, 492-499, (2010).

41 Hartmann, N. *et al.* Launching Propagating Surface Plasmon Polaritons by a Single Carbon Nanotube Dipolar Emitter. *Nano Lett.* **12**, 177-181, (2011).

42 Bharadwaj, P., Bouhelier, A. & Novotny, L. Electrical Excitation of Surface Plasmons. *Phys. Rev. Lett.* **106**, 226802, (2011).

43   Berndt, R., Gimzewski, J. K. & Johansson, P. Inelastic tunneling excitation of tip-induced plasmon modes on noble-metal surfaces. *Phys. Rev. Lett.* **67**, 3796-3799, (1991).

44   Persson, B. N. J. & Baratoff, A. Theory of photon emission in electron tunneling to metallic particles. *Phys. Rev. Lett.* **68**, 3224-3227, (1992).

45   Berndt, R. *et al.* Photon Emission at Molecular Resolution Induced by a Scanning Tunneling Microscope. *Science* **262**, 1425-1427, (1993).

46   Hoffmann, G., Libioulle, L. & Berndt, R. Tunneling-induced luminescence from adsorbed organic molecules with submolecular lateral resolution. *Phys. Rev. B* **65**, 212107, (2002).

47   Chen, C., Chu, P., Bobisch, C. A., Mills, D. L. & Ho, W. Viewing the Interior of a Single Molecule: Vibronically Resolved Photon Imaging at Submolecular Resolution. *Phys. Rev. Lett.* **105**, 217402, (2010).

48   Huan, Q., Jiang, Y., Zhang, Y. Y., Ham, U. & Ho, W. Spatial imaging of individual vibronic states in the interior of single molecules. *J. Chem. Phys.* **135**, 014705-014706, (2011).

49   Wu, S. W., Nazin, G. V. & Ho, W. Intramolecular photon emission from a single molecule in a scanning tunneling microscope. *Phys. Rev. B* **77**, 205430, (2008).

50   Rossel, F., Pivetta, M. & Schneider, W.-D. Luminescence experiments on supported molecules with the scanning tunneling microscope. *Surf. Sci. Rep.* **65**, 129-144, (2010).

51   Reed, M. A., Zhou, C., Muller, C. J., Burgin, T. P. & Tour, J. M. Conductance of a Molecular Junction. *Science* **278**, 252-254, (1997).

52   Liu, Z. *et al.* Revealing the molecular structure of single-molecule junctions in different conductance states by fishing-mode tip-enhanced Raman spectroscopy. *Nat Commun* **2**, 305, (2011).

53   Stanciu, C., Sackrow, M. & Meixner, A. J. High NA particle- and tip-enhanced nanoscale Raman spectroscopy with a parabolic-mirror microscope. *J. Microsc-Oxford* **229**, 247-253, (2008).

54   Lakowicz, J. R. & Berndt, K. W. Lifetime-selective fluorescence imaging using an rf phase-sensitive camera. *Rev. Sci. Instrum.* **62**, 1727-1734, (1991).

55   Dürr, A. C. *et al.* High structural order in thin films of the organic semiconductor diindenoperylene. *Appl. Phys. Lett.* **81**, 2276-2278, (2002).

56   Kelley, T. W. & Frisbie, C. D. Gate Voltage Dependent Resistance of a Single Organic Semiconductor Grain Boundary. *J. Phys. Chem. B* **105**, 4538-4540, (2001).

57   Loi, M. A. *et al.* Supramolecular organization in ultra-thin films of [alpha]-sexithiophene on silicon dioxide. *Nat Mater* **4**, 81-85, (2005).

58   Gisslén, L. & Scholz, R. Crystallochromy of perylene pigments: Interference between Frenkel excitons and charge-transfer states. *Phys. Rev. B* **80**, 115309, (2009).

59   Heinemeyer, U. *et al.* Exciton-phonon coupling in diindenoperylene thin films. *Phys. Rev. B* **78**, 085210, (2008).

60   Lee, C. J., Lee, S. Y., Karim, M. R. & Lee, M. S. Comparison of the adsorption orientation for 2-mercaptobenzothiazole and 2-mercaptobenzoxazole by SERS spectroscopy. *Spectrochim. Acta A* **68**, 1313-1319, (2007).

61   Lambe, J. & McCarthy, S. L. Light Emission from Inelastic Electron Tunneling. *Phys. Rev: Lett.* **37**, 923-925, (1976).

62   Young, R., Ward, J. & Scire, F. The Topografiner: An Instrument for Measuring Surface Microtopography. *Rev. Sci. Instrum.* **43**, 999-1011, (1972).

63   Young, R. D. Surface microtopography. *Phys. Today* **24**, 8, (1971).

64   Gimzewski, J. K., Reihl, B., Coombs, J. H. & Schlittler, R. R. Photon emission with the scanning tunneling microscope. *Z. Physik B - Cond. Mat.* **72**, 497-501, (1988).

65   Gimzewski, J. K., Sass, J. K., Schlitter, R. R. & Schott, J. Enhanced Photon Emission in Scanning Tunnelling Microscopy. *EPL (Europhysics Letters)* **8**, 435, (1989).

66   Wittneven, C., Dombrowski, R., Morgenstern, M. & Wiesendanger, R. Scattering States of Ionized Dopants Probed by Low Temperature Scanning Tunneling Spectroscopy. *Phys. Rev. Lett.* **81**, 5616-5619, (1998).

67   Qiu, X. H., Nazin, G. V. & Ho, W. Vibrationally Resolved Fluorescence Excited with Submolecular Precision. *Science* **299**, 542-546, (2003).

68   Flaxer, E., Sneh, O. & Cheshnovsky, O. Molecular Light Emission Induced by Inelastic Electron Tunneling. *Science* **262**, 2012-2014, (1993).

69   Guo, X. L. *et al.* Molecular fluorescence from ZnTBP porphyrin molecular layers on Cu(100) induced by tunnelling currents. *Nanotechnology* **15**, S402, (2004).

70   Peter, K., Vollhart, C. & Neil, E. *Organische Chemie*. 5. Edition edn, P. 787ff (Wiley-VCH Verlag, 2011).

71   Steidtner, J. & Pettinger, B. Tip-enhanced Raman spectroscopy and microscopy on single dye molecules with 15 nm resolution. *Phys. Rev. Lett.* **100**, (2008).

72   Wackenhut, F., Failla, A. V. & Meixner, A. J. Multicolor Microscopy and Spectroscopy Reveals the Physics of the One-Photon Luminescence in Gold Nanorods. *Phys. Chem. C* **117**, 17870-17877, (2013).

7. Publication List

1.   Fleischer, M.; Stade, F.; Heeren, A.; Haeffner, M.; Kern, D. P.; <u>Braun, K.;</u> Stanciu, C.; Meixner, A. J., "Arrays of Well-Defined Size-Tunable Metallic Nano-Cones for Plasmonic Applications". *MRS Online Proceedings Library* **2007,** *1055*.

2.   Fleischer, M.; Stanciu, C.; Stade, F.; Stadler, J.; <u>Braun, K</u>.; Heeren, A.; Haffner, M.; Kern, D. P.; Meixner, A. J., "Three-dimensional optical antennas: Nanocones in an apertureless scanning near-field microscope". *Appl. Phys. Lett.* **2008,** *93* (11).

3.   Fleischer, M.; <u>Braun, K</u>.; Zhang, D.; Jäger, S.; Meixner, A. J.; Kern, D. P. Plasmonic gold structures with individually designed geometries, *Proc. SPIE* **2009**; p 73941Q.

4.   Fleischer, M.; Stade, F.; Heeren, A.; Haffner, M.; <u>Braun, K</u>.; Stanciu, C.; Ehlich, R.; Horber, J. K. H.; Meixner, A. J.; Kern, D. P., "Nanocones on transparent substrates for investigations in scanning probe microscopes". *Microelectron. Eng.* **2009,** *86* (4-6), 1219-1221.

5.   Wang, X.; Zhang, D.; <u>Braun, K.</u>; Egelhaaf, H.-J.; Meixner, A. J., "Confocal and near-field spectroscopic investigation of P3HT:PCBM organic blend film upon thermal annealing", *Proc. SPIE* **2009**; p 73950F.

6.   Zhang, D.; Wang, X.; <u>Braun, K</u>.; Egelhaaf, H. J.; Fleischer, M.; Hennemann, L.; Hintz, H.; Stanciu, C.; Brabec, C. J.; Kern, D. P.; Meixner, A. J., "Parabolic mirror-assisted tip-enhanced spectroscopic imaging for non-transparent materials". *J. Raman Spectrosc.***2009,** *40* (10), 1371-1376.

7.   Fleischer, M.; Zhang, D.; <u>Braun, K</u>.; Jager, S.; Ehlich, R.; Haffner, M.; Stanciu, C.; Horber, J. K. H.; Meixner, A. J.; Kern, D. P., "Tailoring gold nanostructures for near-field optical applications". *Nanotechnology* **2010,** *21* (6).

8.   Wang, X.; Zhang, D.; <u>Braun, K</u>.; Egelhaaf, H. J.; Brabec, C. J.; Meixner, A. J., "High-Resolution Spectroscopic Mapping of the Chemical Contrast from Nanometer Domains in P3HT:PCBM Organic Blend Films for Solar-Cell Applications". *Adv. Funct. Mat.* **2010,** *20* (3), 492-499.

9.   Zhang, D.; Heinemeyer, U.; Stanciu, C.; Sackrow, M.; <u>Braun, K</u>.; Hennemann, L. E.; Wang, X.; Scholz, R.; Schreiber, F.; Meixner, A. J., "Nanoscale Spectroscopic Imaging of Organic Semiconductor Films by Plasmon-Polariton Coupling". *Phys. Rev. Lett.* **2010,** *104* (5).

10.   Zhang, D.; Horneber, A.; Mihaljevic, J.; Heinemeyer, U.; <u>Braun, K</u>.; Schreiber, F.; Scholz, R.; Meixner, A. J., "Plasmon resonance modulated photoluminescence and Raman spectroscopy of diindenoperylene organic semiconductor thin film". *J. Lumin.* **2011,** *131* (3), 502-505.

11.   Hentschel, M.; Dorfmuller, J.; Giessen, H.; Jager, S.; Kern, A. M.; <u>Braun, K</u>.; Zhang, D.; Meixner, A. J., "Plasmonic oligomers in cylindrical vector light beams". *Beilstein J. Nanotech.* **2013,** *4*, 57-65.

12.   Jager, S.; Kern, A. M.; Hentschel, M.; Jager, R.; Braun, K.; Zhang, D.; Giessen, H.; Meixner, A. J., „Au Nanotip as Luminescent Near-Field Probe". *Nano Lett.* **2013,** *13* (8), 3566-3570.

13.   Braun, K.; Zhang, D.; Wang, X.; Mihaljevic, J.; Meixner, A., "Novel Parabolic Mirror Microscope Illuminated with Cylindrical Vector Beams for Confocal and Tip Enhanced Super Resolution Imaging". In *Fringe 2013*, Osten, W., Ed. Springer Berlin Heidelberg: 2014; pp 791-796.

14.   Blum, C.; Opilik, L.; Atkin, J. M.; Braun, K.; Kammer, S. B.; Kravtsov, V.; Kumar, N.; Lemeshko, S.; Li, J. F.; Luszcz, K.; Maleki, T.; Meixner, A. J.; Minne, S.; Raschke, M. B.; Ren, B.; Rogalski, J.; Roy, D.; Stephanidis, B.; Wang, X.; Zhang, D.; Zhong, J. H.; Zenobi, R., "Tip-enhanced Raman spectroscopy - an interlaboratory reproducibility and comparison study". *J. Raman Spectrosc.* **2014,** *45* (1), 22-31.

15.   Braun, K.; Kern, A. M.; Wang, X.; Adler, H.; Peisert, H.; Chasse, T.; Zhang, D.; Meixner, A. J., "Superluminescence from an optically pumped single molecule tunneling junction by injection of plasmon induced hot electrons". *submitted,* 2014.

8. Acknowledgments

I would like to thank:

- My supervisor **Prof. Dr. Alfred J. Meixner** (University of Tübingen) for the nice time in his working group and giving me the great opportunity for this thesis. Also for the invaluable support and giving me a great degree of freedom in work.

- **Prof. Dr. Thomas Chassé** and his working group for assisting and discussion with the STM experiments.

- **PD Dr. Dai Zhang** (University of Tübingen) and **Dr. Catrinel Stanciu** for guidance start up help and advices.

- **Wolfgang Neu** for always preparing exactly the sample substrate which I needed.

- **Dr. Wolfgang Langer** (University of Tübingen) and the whole **administration office** (University of Tübingen) for solving the small and bureaucratic problems.

- My girlfriend **Katharina List** for her priceless support, encouraging and her sympathetic during this thesis.

- **Claudia Braun, Frank Wackenhut** and **Sebastien Peter** for the invaluable support and "solving" of problems.

- All members of the **Nano-optics group, University of Tübingen** for fruitful discussions and the team work.

Chapter 1. Gap mode spectroscopy: Enhancing the fluorescence of molecules via coupling to a plasmon mode of a near-field tip.

We have measured correlated topographic and near-field optical images of an organic semiconductor thin film (DIP) deposited on a silicon substrate. The feedback to keep the tip at a constant distance to the surface was based on a tuning fork shear-force sensor. The optical image was recorded with an APD and at specific positions spectra were taken with a CCD-camera coupled to a spectrometer. DIP thin films form molecular layers with an island structure and sub-μm sized terraces. Single molecular steps at the boundary of the terraces can be clearly resolved in the topographic image. The upright orientation of the molecule is derived from the Raman spectra of the films. The main emphasis of this study is on the photoluminescence (PL) properties of the molecular film, which is strongly enhanced by the presence of the plasmonic tip. Furthermore the optical image shows an even further increased optical signal at the boundaries of the molecular domains. The enhanced PL is arised from the coupling between a plasmonic mode of the gold tip with the exciton polaritons in the DIP-film. This coupling is strongly influenced by the local film morphology and thus leads to increased PL-contrast in the optical image.

This chapter is based on:

Zhang, D.; Heinemeyer, U.; Stanciu, C.; Sackrow, M.; **Braun, K**.; Hennemann, L. E.; Wang, X.; Scholz, R.; Schreiber, F.; Meixner, A. J., "Nanoscale Spectroscopic Imaging of Organic Semiconductor Films by Plasmon-Polariton Coupling". *Phys. Rev. Lett.* **2010,** *104* (5).

Zhang, D.; Horneber, A.; Mihaljevic, J.; Heinemeyer, U.; **Braun, K**.; Schreiber, F.; Scholz, R.; Meixner, A. J., "Plasmon resonance modulated photoluminescence and Raman spectroscopy of diindenoperylene organic semiconductor thin film". *J. Luminesc.* **2011,** *131* (3), 502-505.

Nanoscale Spectroscopic Imaging of Organic Semiconductor Films
by Plasmon-Polariton Coupling

D. Zhang,[1,†] U. Heinemeyer,[2] C. Stanciu,[1] M. Sackrow,[1] K. Braun,[1] L. E. Hennemann,[1] X. Wang,[1] R. Scholz,[3]
F. Schreiber,[2] and A. J. Meixner[1,*]

[1]*Institute of Physical and Theoretical Chemistry, University of Tübingen, D-72076 Tübingen, Germany*
[2]*Institute of Applied Physics, University of Tübingen, D-72076 Tübingen, Germany*
[3]*Walter Schottky Institute and Physics Department, Technical University of Munich, D-80333 München, Germany*
(Received 27 February 2009; published 3 February 2010)

Tip-enhanced near-field optical images and correlated topographic images of an organic semiconductor film (diindenoperylene, DIP) on Si have been recorded with high optical contrast and high spatial resolution (17 nm) using a parabolic mirror with a high numerical aperture for tip illumination and signal collection. The DIP molecular domain boundaries being one to four molecular layers (1.5–6 nm) high are resolved topographically by a shear-force scanning tip and optically by simultaneously recording the 6×10^5 times enhanced photoluminescence (PL). The excitation is 4×10^4 times enhanced and the intrinsically weak PL-yield of the DIP-film is 15-fold enhanced by the tip. The Raman spectra indicate an upright orientation of the DIP molecules. The enhanced PL contrast results from the local film morphology via stronger coupling between the tip plasmon and the exciton-polariton in the DIP film.

Because of their exciting electronic, optical, and optoelectronic properties, organic semiconductor films are extensively studied for applications in solar cells, organic light emitting diodes, and organic field-effect transistors [1,2]. Diindenoperylene (DIP) is one of the promising organic semiconductor materials. If deposited under suitable conditions on Si oxide or ITO, it forms closed films with high structural order and has a relatively large exciton diffusion length of about 100 nm along the growth direction on ITO [3,4]. The electronic properties of thin films are usually different from the monomer or bulk crystal properties; moreover, they depend strongly on the microscopic film morphology, such as grain boundaries. The need for understanding and exploiting these phenomena led to a large number of investigations in scanning probe microscopy combined with confocal microscopy [5]. However, the quantitative spectroscopic measurement of local optical properties of organic semiconductor surfaces with a resolution matching molecular domains has been plagued by a lack of contrast, sensitivity, or spatial resolution. To address this challenging issue, we have carried out tip-enhanced spectroscopic measurements on a DIP thin film employing our home-built parabolic mirror assisted near-field optical microscope [6].

A sharp laser-illuminated Au tip is used as an optical antenna approaching closely to the sample surface, confining the excitation field to a subdiffraction volume at the tip apex and retrieving emitted or scattered photons to the far field for detection. A sensitive feedback based on tunneling current [7] or mechanical force [8] prevents the tip from crashing into the surface and allows for recording simultaneously the topography and the correlated chemical information via Raman spectroscopy [7]. The topographic

resolution of this technique can reach a few nanometers, whereas the optical resolution is essentially determined by the apex size of the antenna tip [9].

Thirty nm thick DIP films were deposited on Si(100) covered with native oxide [10]. Tip-enhanced spectroscopic measurements are performed by radially illuminating the apex of an electrochemically etched sharp Au tip with $\lambda = 632.8$ nm He-Ne laser light polarized along the tip shaft [Fig. 1(a)]. In contrast to conventional near-field optical microscopes, we used a parabolic mirror for illumination and signal collection [Fig. 1(b)] which are performed from the top of the sample under perfect diffraction and polarization conditions. Hence, no restriction applies with respect to the conductivity or transparency of the sample substrate [11].

In Fig. 2(a), a near-field optical image of the DIP film is shown with the simultaneously recorded topography, revealing the well-known DIP film morphology with stepped
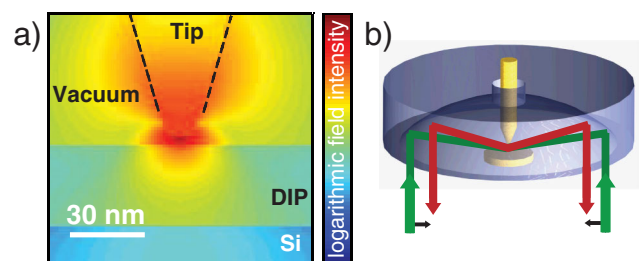

FIG. 1 (color online). (a) Calculated field intensity distribution when an Au tip is placed 3 nm above a 30 nm DIP film. The intensity is plotted on a logarithmic scale. (b) Illumination (green upright arrows) and optical signal collection (red downward arrows) by the parabolic mirror.

terraces [10]. Most of the domains exhibit step heights of 1.5–1.8 nm, in accordance with upright-oriented DIP molecules defining a lattice constant along the substrate normal of 1.65 nm [see Fig. 2(b)] [10]. Some exceptionally high dots appearing in the topography, such as the one labeled as 1, are probably dust particles from the ambient experimental condition. The near-field optical image shows bright lines, spots, and dark regions appearing at first glance like random features. However, a thorough comparison with the topography reveals that the bright features correlate with most of the DIP domain boundaries, such as the regions labeled as 2, 3, and 4. Moreover, enhanced optical contrast is observed in regions where no molecular step is revealed in the topography, such as region 5. The optical signal from bright regions is about four times higher than that of dark regions and does not depend significantly on the step height. The blue vertical arrows in Fig. 2(b) point out a terrace boundary of one molecular height where a sharp optical signal with a FWHM of ≈ 17 nm (red horizontal arrows) is resolved, indicating an optical resolution of at least 17 nm.

To investigate the nature of the tip-enhanced spatially resolved optical features, spectroscopic measurements were performed. Figure 3(a) shows the spectrum (II) recorded without a tip. The dominant Raman line at 520 cm^{-1} is the optical phonon of the Si substrate. The broader feature around 960 cm^{-1} arises from the density of states of two phonons in Si [12]. The contribution of the DIP film is barely visible, consisting of a weak PL background with a maximum at 1575 cm^{-1} (1.76 eV). Upon approaching the Au tip close to the DIP film, an intense tip-enhanced signal appears (spectrum III), consisting of a broad PL background and distinct Raman lines. The

Raman lines of the Si substrate lying 30 nm beneath the DIP surface appear weaker due to the strongly reduced field enhancement. The tip-enhanced Raman bands [Fig. 3(a) IV] at 1291, 1401, 1466, and 1615 cm^{-1} correspond to far-field measured and calculated breathing modes of DIP within deviations of a few cm^{-1} [13,14]. Crystalline DIP films exhibit strongly uniaxial anisotropic properties with the largest component of the dielectric tensor along a direction inclined by approx. 17° against the substrate normal [15]. In Raman spectroscopy, the scattering cross sections are proportional to $|\vec{e}_s \cdot \overleftrightarrow{R} \cdot \vec{e}_i|^2$, where $\vec{e}_i$ and $\vec{e}_s$ are the polarization directions of the incident and scattered fields, and $\overleftrightarrow{R}$ is the Raman tensor (see supplementary material [16]). The near-field below the tip apex is oriented along the substrate normal so that it couples efficiently to the largest element of the
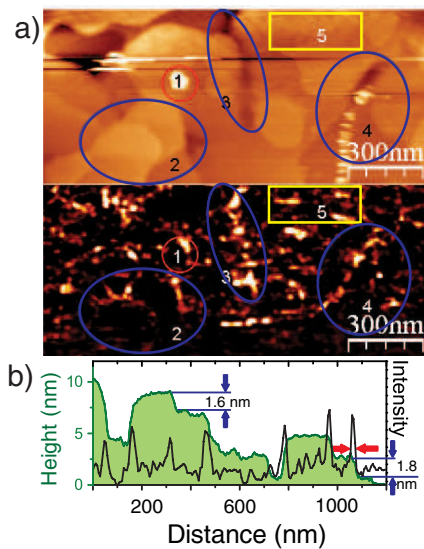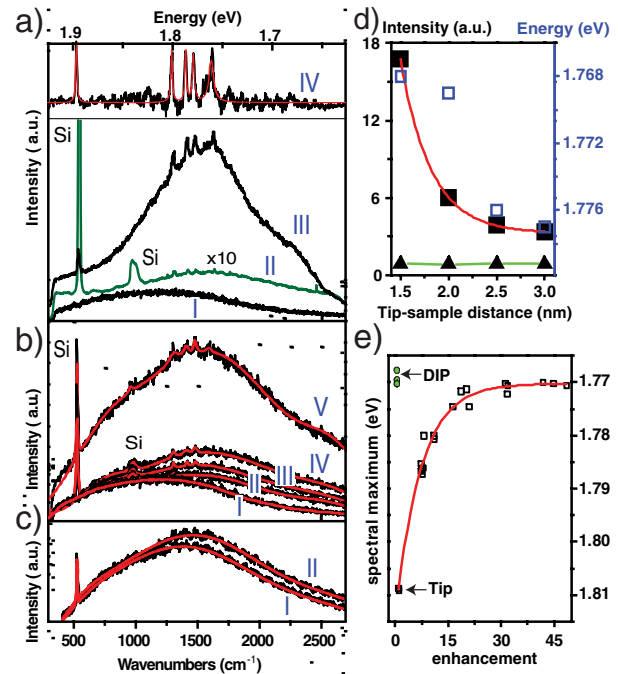

FIG. 3 (color online). (a) Confocal far-field PL-spectrum (I) of a tip alone integrated for 10 s , (II) of DIP film integrated for 900 s, and (III) tip-enhanced spectrum integrated for 10 s at a tip-DIP distance of 3 nm. Excitation power: 170 μW. (IV) Tip-enhanced Raman spectrum obtained from (III) after subtraction of PL-background with fitted spectrum (red curve). (b) Spectra collected at different tip-sample distances. II, 3 nm; III, 2.5 nm; IV, 2 nm; V, 1.5 nm and I: spectrum of tip alone. Integration time: 10 s. (c) PL spectra, (I) from inside a domain and (II) from a domain edge. Tip-sample distance: 3 nm. Excitation power: 170 μW. Acquisition time: 30 s. (d) Intensity of the Si Raman line (triangles), enhancement (closed squares), and energy shift (open squares) of the PL spectra as a function of tip-sample distance. (e) Energetic shift of the spectral maximum as a function of the total signal enhancement for different tips and days (empty squares). For comparison, the spectral maximum from the confocal far-field spectra of DIP are included (green circles).

FIG. 2 (color online). (a) Simultaneously recorded topographic (upper panel) and near-field optical images (lower panel). Scan area: 1.5×0.7 μm^2. Laser power: 170 μW. Tip-sample distance: 3 nm. (b) Line profile through the topographic image with its correlated optical intensity.

Raman tensor corresponding to the long axis of the DIP-molecule. Therefore, the C-C breathing modes are selectively excited giving the Raman patterns observed in the tip-enhanced Raman spectroscopy (TERS) spectrum [17].

In most TERS investigations, the dispersive PL background is of minor interest. However, in our spectra, it dominates the observed intensity so that it is the key to a deeper understanding of the influence of surface morphology on the DIP optical properties. The absorption spectrum excited with a polarization perpendicular to the sample surface shows distinct vibronic lines at 2.25, 2.42, and 2.59 eV [15], giving PL bands at 2.14, 1.96, and 1.77 eV [18]. The two higher lying PL bands cannot be excited by the He-Ne laser. Nevertheless, in the electronic ground state, the first vibronic levels of typical Raman-active breathing modes around 0.17 eV are still thermally occupied with a probability of about 10^{-3}. Starting from these vibronic levels, a further weak resonance is expected around 2.09 eV. The off-resonant excitation with our laser results in the PL band around 1.76 eV shown in Fig. 3(a) (III).

Spectra collected as a function of tip-sample distances in the range from 3 nm to 1.5 nm [see Fig. 3(b)] reveal a steeply increasing PL intensity when approaching the sample to the tip, accompanied by a red shift of the PL maximum, whereas the positions of the DIP Raman lines remain constant. The PL spectrum collected from the Au tip alone is shown in Figs. 3(a) and 3(b) as curve I with a maximum at 1225 cm^{-1} (1.807 eV). It is typical for our Au tips and serves as a reference for estimating the contribution of the tip PL to the distance-dependent spectra II–V in Fig. 3(b). They show clearly different spectral shapes and intensities as compared to the tip spectrum. This indicates that these spectra involve PL contributions from both tip and DIP film. In Fig. 3(e), the maxima of several distance-dependent spectra (different days with different tips) are plotted against the total signal enhancement, revealing an asymptotic approach from the tip PL maximum towards the DIP PL maximum. Therefore, we conclude that the DIP PL dominates the spectra at close tip-sample distances. A careful fitting of the spectra shown in Fig. 3(b) reveals also a slight red shift of the DIP PL from 1.787 to 1.767 eV [blue open squares in Fig. 3(d), see supplementary material [16]]. Recently, Pettinger *et al.* [9] have reported a comparable red shift from 1.882 to 1.826 eV and an intensity increase of the tip-enhanced Raman spectra when reducing the tip-sample distance from 5 to 1 nm towards a layer of guanine/CIO$^-_4$ adsorbed on an Au(111) crystal surface, assigned to a strongly distance-dependent plasmon coupling between Au tip and Au surface interpreted by a free electron gas model [19].

Finite domain time domain simulations of the time-averaged field distribution for our tip-sample configuration [Fig. 1(a)] reveal a high field enhancement in the gap between the Au tip and the DIP film resulting from the efficient coupling of a localized plasmon in the tip apex

and a respective polarization in the DIP film just below the gap (see supplementary material [16]). The incident radially polarized light field induces a coherent oscillation of the conduction electrons in the tip along the axis, leading to a local field enhancement in and around the tip apex, in the tip-DIP gap, and in the DIP film underneath. Hence, we have a similar situation as found in the case of an Au tip above an Au(111) crystal where the tip plasmon and the localized surface plasmons are coupled by the gap field [20]. In analogy to the conduction electrons in gold, in the highly ordered DIP film, the π electrons provide the major contribution of the dielectric constant [15,17]. Therefore, in response to the plasmon oscillation in the tip, we have a coherent local oscillation of the π electrons in the film leading to an exciton-polariton strongly coupled to the gap field. Integrating the PL intensities of spectra II and III in Fig. 3(a), one can derive that the PL intensity in the TERS spectrum is about 2600 times stronger. In addition, the intensity enhancement in the gap is restricted to an area of about $A = 227$ nm^2, much smaller than the area of the far-field focus with a diameter of about 260 nm, corresponding to $A = 5.3 \times 10^4$ nm^2. Hence, we find an average enhancement factor in the first molecular layer under the tip of 6×10^5. To explain the origin of such a high PL enhancement, one must compare for the tip-enhanced case and for the confocal case the excitation rate Γ_{exc}, and the balance between the radiative decay rate Γ_r and the non-radiative decay rate Γ_{nr}, since the PL intensity is proportional to $\Gamma_{exc}[1 - \Gamma_{nr}/(\Gamma_r + \Gamma_{nr})]$, the term in brackets being the PL yield. The PL in DIP films results from the radiative decay of Frenkel excitons created locally in the surface layer of the molecular film. An exciton has a transition dipole $\mathbf{D}_{exc} = 8.2$ D [17] oriented along the long axis of the DIP molecules. The excitation rate Γ_{exc} is proportional to $|\mathbf{D}_{exc} \cdot \mathbf{E}_{exc}|^2$ where $\mathbf{E}_{exc}$ is the effective excitation field at the laser frequency ω_{exc} in the top layer of the film. From the calculated field intensity distribution in Fig. 1(a) and assuming that the value of the dipole moment in the tip-enhanced case does not differ significantly from the confocal case, we find that the excitation rate is enhanced in the near field by a factor of 4×10^4 as compared to the far-field excitation (see supplementary material [16]). The extra 15-times stronger PL intensity determined from the experiment then has to be explained by the influence of the tip on the PL yield of the film. Crystalline films of perylene chromophores like DIP have an exciton dispersion with a minimum at the surface of the Brillouin zone, resulting in a rather low PL yield in the percent range, or $\Gamma_{nr} \gg \Gamma_r$ [21]. This is different in the presence of the tip. According to Fermi's golden rule, the spontaneous radiative decay rate per frequency interval is $\frac{\partial \Gamma_r(\omega)}{\partial \omega} = \frac{2\omega}{3\hbar\epsilon}|\mathbf{D}_{em}|^2 \rho(\omega)$, where $\mathbf{D}_{em}$ is the transition dipole for emission and $\rho(\omega)$ the photonic mode density along the tip axis. The tip increases locally the photonic mode density $\rho(\omega)$ in the gap between the apex and the DIP-film and thus increases the radiative recombination rate Γ_r.

Furthermore, the absorption by the tip provides an additional Γ_{nr} channel; both effects influence the PL yield. Hence, the extra 15 times stronger PL-intensity must be explained by a 15 fold increase of the PL-yield due to the tip with respect to the confocal far-field excitation, reflecting a 17 times enhanced Γ_r (supplementary material [16]).

An increased PL intensity along the terraces of a molecular crystal has never been observed before due to a lack of spatial resolution and sensitivity. Therefore, our results have to be discussed on the basis of bulk measurements averaging over large sample areas. *In situ* ellipsometric measurements of the complex dielectric function during the growth of pentacene films have revealed a blue shift in the imaginary part of the dielectric function in the first few molecular layers. Such a blue shift with respect to the bulk properties is a consequence of a reduced gas-to-crystal shift in the surface layer and results from a decoupling of the surface or edge molecules and their transitions from the underlying bulk material [22]. Therefore, their Γ_r should correspond more to a single molecule, far above the much slower Γ_r occurring in molecular crystals [23,24]. As a consequence, these molecules are expected to fluoresce independently. The red shift of the PL from step edges shown in Fig. 3(c) seems contradictory to the expected blue-shifted PL. However, we must not only consider the reduced intermolecular interactions at grain boundaries or surface edges, but also an enhanced tip-sample interaction. The energetic influence of an enhanced coupling between the Au plasmon and the DIP exciton-polariton seems to slightly outweigh other energetic influences on the molecular transition energy, giving a small red shift of the PL emission. The energetic shift of the transition energies at step edges leads to a further reduction of the exciton diffusion away from these sites, in keeping with a faster Γ_r arising from the molecular transition dipole. Within the ensemble of edge sites, the distribution over transition energies is influenced by geometric variations like the number of neighboring molecules. The intensity variations along the grain boundaries reflect the local disorder of the step edges, influencing, e.g., Γ_r and Γ_{nr}. Because of the anisotropic properties of the DIP film, the exciton diffusion length in the lateral and vertical directions can be different. Considering the lateral resolution of 17 nm achieved in our near-field imaging of the DIP film, we deduce that the upper limit of the DIP exciton diffusion length in the lateral direction should be comparable to this value. Otherwise, if the exciton generated by the tip-enhanced light field could diffuse away from the region probed by the tip, sharp PL imaging would not be possible. In addition, Kurrle *et al.* [4] have reported an exciton diffusion length of 100 nm along the direction perpendicular to the substrate. Because of the coupling between the tip plasmon and the DIP exciton polariton, we have a different situation since the Γ_r is speeded up so that the radiative lifetime τ_{rad} is reduced.

Therefore, we expect the 100 nm diffusion length to be shortened according to $L_{diff} = \sqrt{D\tau_{rad}}$, where D is the diffusion constant.

In conclusion, we have shown that tip-enhanced near-field optical microscopy with a parabolic mirror microscope reveals fine optical details correlated to the local film morphology and local spectroscopic information at the level of single molecular layers. The increased optical contrast and the nanometer spatial resolution at the molecular domain boundaries indicate an enhanced coupling between the tip plasmon and the exciton polariton in the molecular film, resulting in a 15-fold increased PL-emission yield. Our results open new perspectives for analyzing the local spectroscopic properties of molecular semiconductor films together with the local morphology at a spatial resolution far beyond the diffraction limit.

*alfred.meixner@uni-tuebingen.de
†dai.zhang@uni-tuebingen.de
[1] *Physics of Organic Semiconductors*, edited by W. Brütting (Wiley, Berlin, 2005).
[2] W. R. Salaneck *et al.*, *Conjugated Polymer and Molecular Interfaces: Science and Technology for Photonic and Optoelectronic Applications* (CRC Press, Boca Raton, 2001).
[3] A. C. Dürr *et al.*, Appl. Phys. Lett. **81**, 2276 (2002).
[4] D. Kurrle *et al.*, Appl. Phys. Lett. **92**, 133306 (2008).
[5] M. A. Loi *et al.*, Nature Mater. **4**, 81 (2005).
[6] C. Stanciu *et al.*, J. Microsc. **229**, 247 (2008).
[7] K. F. Domke *et al.*, J. Am. Chem. Soc. **128**, 14721 (2006).
[8] R. M. Stöckle *et al.*, Chem. Phys. Lett. **318**, 131 (2000).
[9] B. Pettinger *et al.*, Phys. Rev. B **76**, 113409 (2007).
[10] A. C. Dürr *et al.*, Phys. Rev. Lett. **90**, 016104 (2003).
[11] M. Sackrow *et al.*, Chem. Phys. Chem. **9**, 316 (2008).
[12] P. A. Temple and C. E. Hathaway, Phys. Rev. B **7**, 3685 (1973).
[13] R. Scholz and M. Schreiber, Chem. Phys. **325**, 9 (2006).
[14] V. Presser *et al.*, J. Raman Spectrosc. 40, 2015 (2009).
[15] U. Heinemeyer *et al.*, Phys. Rev. B **78**, 085210 (2008).
[16] See supplementary material at http://link.aps.org/supplemental/10.1103/PhysRevLett.104.056601 for detailed information.
[17] L. Gisslén and R. Scholz, Phys. Rev. B **80**, 115309 (2009).
[18] M. Heilig *et al.*, J. Lumin. **110**, 290 (2004).
[19] *Near-field Optics and Surface Plasmon Polaritons*, Topics Appl. Phys., edited by S. Kawata (Springer, Berlin, 2001).
[20] J. A. Porto *et al.*, Phys. Rev. B **67**, 085409 (2003).
[21] A. Nollau *et al.*, J. Appl. Phys. **87**, 7802 (2000).
[22] I. Vragović *et al.*, Eur. Phys. J. B **66**, 185 (2008).
[23] I. Vragović *et al.*, Phys. Rev. B **68**, 155202 (2003).
[24] A. Y. Kobitski *et al.*, Phys. Rev. B **68**, 155201 (2003).

Plasmon resonance modulated photoluminescence and Raman spectroscopy of diindenoperylene organic semiconductor thin film

D. Zhang [a,*], A. Horneber [a], J. Mihaljevic [a], U. Heinemeyer [b], K. Braun [a], F. Schreiber [b], R. Scholz [c], A.J. Meixner [a,*]

[a] Institut für Physikalische und Theoretische Chemie, University of Tübingen, 72076 Tübingen, Germany
[b] Institut für Angewandte Physik, University of Tübingen, 72076 Tübingen, Germany
[c] Institut für Angewandte Photophysik, Technische Universität Dresden, 01062 Dresden, Germany

A B S T R A C T

In a comparison between a bare diindenoperylene (DIP) film and a DIP film spin-coated with a layer of gold nanoparticles, we have investigated the influence of plasmon resonances in the gold particles on spectroscopic properties of the molecular film. Under off-resonant excitation with a laser at 633 nm, the bare DIP film showed only weak photoluminescence (PL) and Raman signals, but after spin-coating gold nanoparticles on such a DIP film, we found an enhancement of both the PL and Raman signals by a factor of about 3, whereas no enhancement could be observed when the same sample was excited with laser light of 488 nm. This difference reveals that at 633 nm, plasmon resonances in the gold nanoparticles are excited, leading in turn to an enhancement of PL and Raman signals of the weakly absorbing DIP film via coupling between plasmons in the gold particles and exciton–polaritons in the molecular film. For the laser at 488 nm, due to a much larger absorption coefficient of DIP, excitons in the molecular film are directly excited, out-weighing the influence of an off-resonant coupling to the plasmon resonances in the gold particles occurring at much lower energy.

© 2010 Elsevier B.V. All rights reserved.

1. Introduction

During the last decades, semiconducting organic materials have been studied intensively due to their interesting opto-electronic properties, giving rise to a broad range of applications [1] such as organic field effect transistors, organic light emitting diodes or organic solar cells. Diindenoperylene (DIP) is one of the promising semiconducting organic materials since it forms closed films with high structural order, relatively large hole mobility and rather long exciton diffusion length [2]. The optical response of dissolved DIP molecules is dominated by the π–π^* HOMO–LUMO transition, revealing a strong coupling of the optical excitation to internal vibrations around 0.17 eV. In the crystalline phase, this spectroscopic fingerprint of the excited monomer is modified by the interference between charge transfer states involving stack neighbours and Frenkel excitons consisting of Bloch waves formed from neutral molecular excitations [3–6].

Surface plasmon resonances in metallic nanoparticles can produce a large enhancement of local electric field in their immediate surroundings. This phenomenon can be exploited for an increased optical absorption resulting in a larger photocurrent in p–n junctions [7] and for surface enhanced Raman scattering, allowing detection of single molecules [8,9]. The field enhancement is restricted to a small volume around each nanoparticle, so that the combination of plasmonic resonances with scanning probe techniques can simultaneously achieve a strongly enhanced optical response together with a high spatial resolution [10]. As demonstrated recently, placing a sharp gold tip as a local probe within a few nanometers from the sample surface into the focus of a parabolic mirror, the strong plasmonic enhancement of the local electric field around the tip apex can be used for a highly localized excitation of a sample of interest, in our case, a DIP film [11]. Moreover, the evanescent electric field around the tip alters the photonic density of states, modifying in turn the spontaneous emission rate from the excitons in the molecular material directly underneath [10,12]. Based on this excitation and detection scheme, dramatically enhanced photoluminescence (PL) and Raman spectra from DIP could be observed together with spatially resolved monomolecular steps of highly ordered DIP films, which revealed a localized 'shining-edge effect', with a further enhancement of PL by a factor of about 4 with respect to flat surface regions [11].

In the present work, we investigate the influence of gold nanoparticles on Raman scattering and PL emission from a semiconducting DIP thin film for two laser lines either resonant (633 nm) or off-resonant (488 nm) with respect to plasmon modes in the metallic nanoparticles, revealing how the Raman

and PL processes are influenced by the respective resonance conditions. Finite-difference time-domain (FDTD) simulations of the interaction between the enhanced electric field around the spherical gold particles and the DIP films are used for an interpretation of the experimental findings.

2. Material and methods

All samples were prepared on smooth Si(1 0 0) substrates covered by 150 nm of SiO$_2$. DIP layers of 20 nm thickness were grown at a substrate temperature of 130 °C at a rate of 12 ± 3 Å/min under UHV conditions, leading to films of high structural order. 20 µL gold nanoparticles (20 nm diameter) were deposited on these films (Sigma-Aldrich, 1:20 diluted in water) by dropping the aqueous suspension onto the DIP thin film surface. The sample was then rotated at a speed of 3200 rpm to spin-coat the gold nanoparticles over the surface. Optical properties of the DIP sample are measured on a home-built confocal optical microscope [13,14]. Instead of an objective lens, this microscope uses a parabolic mirror (numerical aperture 0.998) for laser focusing and signal collection. This instrument yields a small focal spot with an area of $0.134\lambda^2$. The excitation laser beam is directed to this parabolic mirror and reflected onto the sample surface coinciding with the focal plane of the mirror. Either radial or azimuthally polarized laser beams were used for the measurements. For azimuthal polarization, the electric field distributes exclusively in the xy focal plane. For radial polarization of the laser beam in the focal region the electric field is mainly polarized along the sample normal z (93.5% intensity at 633 nm) with a marginal intensity (6.5%) polarized within the xy focal plane [15]. The optical signal is detected either by a CCD coupled spectrometer (600 grating) or by an avalanche photodiode detector (APD) for PL imaging.

3. Results and discussion

3.1. Excitation of DIP thin film with 488 nm (2.54 eV) laser

The HOMO–LUMO transition of crystalline DIP has a maximum at 2.25 eV (551 nm) corresponding to the first absorption peak (0-0) of the optical response. The spacing of the vibronic progression still resembles the one for dissolved monomers, but the relative strength of different subbands can be understood only

from an in-depth analysis of the interference between Frenkel excitons and CT transitions [3–6].

Fig. 1a shows the resonant Raman spectra collected from a 20 nm thick DIP film under excitation at 488 nm polarized either radially (spectrum I) or azimuthally (spectrum II). With radially polarized excitation, clear Raman features (inset of Fig. 1a) appeared at 520, 634, 1284, 1395, 1459 and 1608 cm^{-1}. Except for the intense Raman peak at 520 cm^{-1} and a broad 2 phonon band around 960 cm^{-1} originating from the Si substrate [16], all other Raman cross-sections can be assigned to the in-plane C–C stretching vibrations and C–H bending modes of a DIP molecule [4,17]. The PL from DIP increases towards larger Stokes shift, saturating the detector above 2750 cm^{-1}. Non-saturated PL spectra covering the range between 1.75 and 2.40 eV are shown in Fig. 1b. A small mismatch between four adjacent detection windows results from the energy-dependent detection efficiency of the camera. The intensity maxima located at 1.81, 1.97 and 2.14 eV correspond to similar PL features reported earlier [18].

When switching the polarization to the azimuthal mode, where the electric field is restricted to the xy focal plane, a much smaller Raman spectrum (inset of Fig. 1a) was collected. The Si Raman peak at 520 cm^{-1} in spectrum II amounts to only 56% of its intensity in spectrum I due to its polarization-dependent Raman cross-section at this excitation wavelength. The Raman intensities assigned to DIP decreased more strongly, for the Raman peak at 1284 cm^{-1} to about 20% of the intensity with radially polarized excitation. This reduction is somewhat larger than that of the ratio of the respective PL intensities, amounting to about 30%. Previous investigations of similar DIP films have demonstrated that the transition dipole oriented along the long axis of the molecules is tilted by about $\theta \approx 17°$ against the substrate normal, so that a more efficient interaction with light polarized along the substrate normal can be expected, as realized for radial polarization of the laser beam [3,11].

3.2. Plasmonic enhancement for excitation with 633 nm (1.96 eV) laser

In this section, we compare the spectra obtained from a bare DIP film and from a DIP film after deposition of gold nanoparticles. In the latter case, the laser at 633 nm (1.96 eV) is expected to result in an efficient coupling to the plasmonic resonances in the gold spheres, yielding eventually a moderate enhancement of the spectroscopic response of DIP.
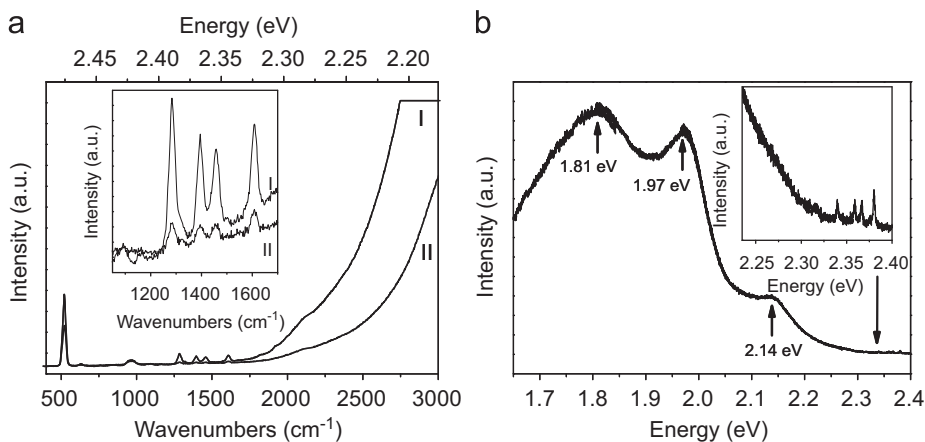

Fig. 1. (a) Spectra collected with a confocal parabolic-mirror microscope from DIP thin film with 488 nm excitation, integration time 60 s. I: with polarization perpendicular to the sample surface (radially polarized laser) and II: with polarization in the sample plane (azimuthally polarized laser). Inset : spectra I and II on an enlarged scale highlighting the Raman features. (b) PL spectra collected over four adjacent spectral detection windows for polarization perpendicular to the sample surface (radially polarized laser beam), integrated over 10 s for each spectrum. Inset: enlarged spectrum of the region with the strongest Raman features of DIP.
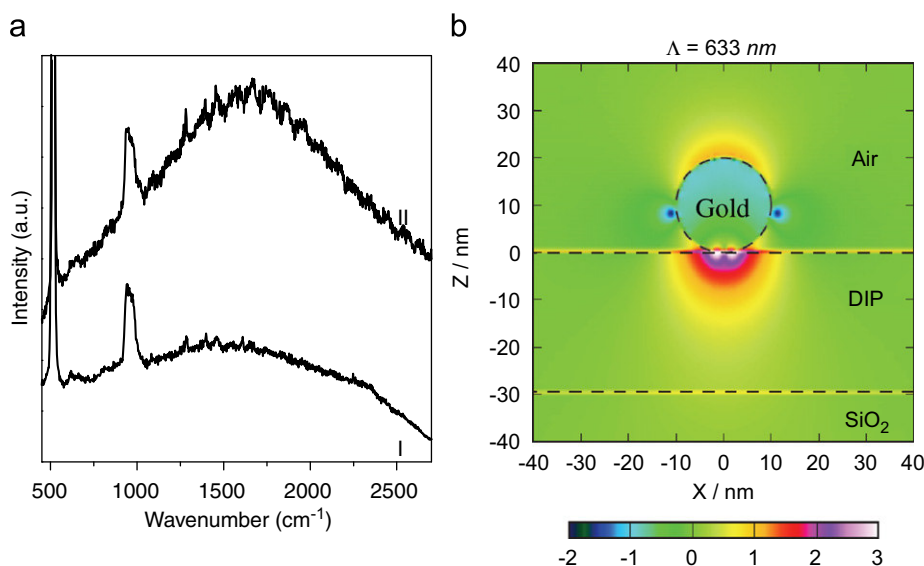
Fig. 2. (a) Spectra collected for excitation at 633 nm with radial polarization. I: DIP film, spectrum integrated over 60 s and II: DIP film covered with gold nanoparticles, spectrum integrated over 60 s. Laser power: 170 μW. (b) Field intensity for excitation of a gold nanosphere with a diameter of 20 nm on top of a DIP film with a thickness of 30 nm, for polarization along the sample normal z. The results of a FDTD simulation are reported on a logarithmic scale corresponding to relative intensities of 10^{-2}–10^3 with respect to the far field region.

Fig. 2a shows the spectra recorded from the DIP film with 633 nm illumination. The dominant Raman line at 520 cm^{-1} and the broad band around 960 cm^{-1} both arise from the Si substrate [16]. Raman and PL signals from the bare DIP film (spectrum I) were very weak. The positions of all the distinguishable Raman bands (1284, 1395, 1459 and 1608 cm^{-1}) are in good agreement with those observed when excited at 488 nm. The very weak PL and Raman intensities observed with an excitation laser of 633 nm are due to the inefficiency of the off-resonant excitation at 1.96 eV with respect to the 0–0 subband of crystalline DIP at 2.25 eV. Spectrum II was collected from the DIP thin film after deposition of Au nanoparticles. Despite the progressive oscillatory features being superimposed on the spectrum, the DIP Raman features remain clearly visible, and the PL background was significantly increased. The Si Raman features arise from the substrate region far away from the gold nanoparticles, so that no plasmonic enhancement can be expected. Therefore, normalizing the spectra to the respective Raman intensities of Si, for DIP we derived a PL and Raman enhancement factor of about 3. Confocal PL imaging has revealed an aggregation of the gold nanoparticles into larger clusters, which have a broad distribution of red-shifted plasmon resonances [19], as compared to that of the individual gold particles in well dispersed aqueous solution [20]. Hence, such particle aggregates must also lead to an enhancement of Raman and PL spectra arising from the DIP film underneath. This agrees well with our previous work based on tip-enhanced spectroscopic measurements, which demonstrated that the coupling between the longitudinal plasmonic resonance in the gold tip and the exciton–polariton in the underlying DIP film enhances the PL emission via the modified photonic mode density close to the tip apex [11]. Due to similarities between the tip-induced plasmon near field and the plasmon resonances arising from aggregated gold nanoparticles, the enhanced PL intensity of the DIP thin film with spin-coated gold particles can be assigned to the same coupling mechanism. This idea is corroborated by FDTD simulations of light intensity around a gold nanoparticle on top of the DIP film as visualized in b. For excitation with a laser at 633 nm at the gold–DIP interface an enhancement of light intensity of about 10^3 can be expected. Due to a small fraction of the DIP surface being covered by gold nanoparticles, the
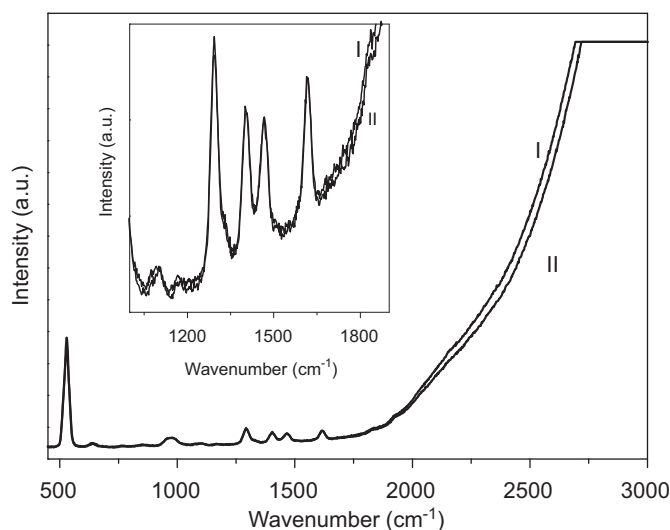

Fig. 3. Raman spectra integrated over 60 s for radially polarized laser beam at 488 nm. I: DIP film and II: DIP film covered with gold particles. Inset: enlarged spectrum covering the region with the largest Raman features of DIP.

observable average enhancement factors for PL and Raman signals remain much smaller.

For a comparison between the enhancement at 633 and 488 nm, DIP films with and without gold nanoparticles have been excited at 488 nm. The respective results in Fig. 3 demonstrate that spectrum I collected from a bare DIP film and spectrum II arising from a DIP film covered with gold nanoparticles exhibit similar Raman and PL intensities. In sharp contrast to excitation at 633 nm, at 488 nm no significant enhancement can be observed. This difference reveals that at 633 nm plasmon resonances in the gold nanoparticle aggregates lead to enhancement of absorption, PL and Raman scattering of the otherwise weakly absorbing DIP film via plasmon–exciton coupling. For 488 nm excitation, however, the situation is reversed. Due to the several orders of magnitude larger absorption cross-section of the DIP film in this

region, excitons in the molecular film can be created independently from the gold particles having their plasmon resonances at much lower energy. Hence, absorption, PL and Raman scattering from the DIP film are no more affected by the coupling between plasmons in the gold particles and exciton–polaritons in the organic material.

4. Conclusions

In summary, we have investigated Raman and PL spectra of 20 nm thick DIP films under resonant and off-resonant excitation conditions. Both the Raman and PL intensity are strongly polarization-dependent. With radially polarized excitation, the Raman signal is about 5 times stronger than azimuthally polarized excitation. On excitation at 633 nm, plasmon resonances of gold nanoparticles spin-coated onto the DIP thin film can be excited more efficiently than excitation at 488 nm, inducing a strong plasmon resonance in aggregates of nanoparticles. Accordingly, only at the longer excitation wavelength, the efficient coupling between the plasmon resonance in the gold nanoparticles and the exciton–polaritons in DIP enhances both the Raman and the PL spectra from the molecular semiconductor.

Acknowledgements

References

[1] F. Schreiber, Phys. Status Solidi A 201 (2004) 1037.
[2] A.K. Tripathi, J. Pflaum, Appl. Phys. Lett. 89 (2006) 082103.
[3] U. Heinemeyer, R. Scholz, L. Gisslén, M.I. Alonso, J.O. Ossó, M. Garriga, A. Hinderhofer, M. Kytka, S. Kowarik, A. Gerlach, F. Schreiber, Phys. Rev. B 78 (2008) 085210.
[4] L. Gisslén, R. Scholz, Phys. Rev. B 80 (2009) 115309.
[5] U. Heinemeyer, K. Broch, A. Hinderhofer, M. Kytka, R. Scholz, A. Gerlach, F. Schreiber, Phys. Rev. Lett. 104 (2010) 257401.
[6] S. Kowarik, A. Gerlach, S. Sellner, F. Schreiber, L. Cavalcanti, O. Konovalov, Phys. Rev. Lett. 96 (2006) 125504.
[7] D.M. Schaadt, B. Feng, E.T. Yu, Appl. Phys. Lett. 86 (2005) 063106.
[8] K.A. Willets, R.P. van Duyne, Annu. Rev. Phys. Chem. 58 (2007) 267.
[9] W.E. Doering, S.M. Nie, J. Phys. Chem. B 106 (2002) 311.
[10] P. Anger, P. Bharadwaj, L. Novotny, Phys. Rev. Lett. 96 (2006) 113002.
[11] D. Zhang, U. Heinemeyer, C. Stanciu, M. Sackrow, K. Braun, L.E. Hennemann, X. Wang, R. Scholz, F. Schreiber, A.J. Meixner, Phys. Rev. Lett. 104 (2010) 056601.
[12] C.K. Carniglia, L. Mandel, K.H. Drexhage, J. Opt. Soc. Am. 62 (1972) 479.
[13] C. Stanciu, M. Sackrow, A.J. Meixner, J. Microsc. 229 (2008) 247.
[14] D. Zhang, X. Wang, K. Braun, H.-J. Egelhaaf, M. Fleischer, L. Hennemann, H. Hintz, C. Stanciu, C.J. Brabec, D.P. Kern, A.J. Meixner, J. Raman Spectrosc. 40 (2009) 1371.
[15] M.A. Lieb, A.J. Meixner, Opt. Express 8 (2001) 458.
[16] P.A. Temple, C.E. Hathaway, Phys. Rev. B 7 (1973) 3685.
[17] R. Scholz, L. Gisslén, B.-E. Schuster, M.B. Casu, T. Chassé, U. Heinemeyer, F. Schreiber, J. Chem. Phys. 134 (2011) 014504.
[18] M. Heilig, M. Domhan, H. Port, J. Lumin. 110 (2004) 290.
[19] M. Steiner, Ch. Debus, A.V. Failla, A.J. Meixner, J. Phys. Chem. C 112 (2008) 3103.
[20] P.N. Njoki, I.I.S. Lim, D. Mott, H-Y. Park, B. Khan, S. Mishra, R. Sujakumar, J. Luo, C.-J. Zhong, J. Phys. Chem. C 111 (2007) 14664.

Chapter 2. Gap mode microscopy: From single point spectra to a hyperspectroscopic image

As an important improvement, a full synchronization between the scanning unit of the microscope and the spectrometer has been realized. This upgrade allows not only measuring the topography with correlated optical signals from an APD, but also acquiring hyperspectroscopic images with a predefined number of data points. In this Chapter we present experimental results on the investigation of the active layer of an organic photovoltaic polymer blend film. By measuring simultaneous the morphology and the spectroscopic information of a poly-3-hexylthiophene (P3HT) and [6,6]-phenyl-C_{61}-butyric acid methyl ester (PCBM) blend film the molecular distribution can be resolved optically at a previously unreached resolution. Furthermore the interplay among the quenching efficiency of the P3HT at the domain boundaries to the PCBM is mapped. This experiments lead to the conclusion that high resolution near-field spectroscopic imaging is an ideal tool to study the local chemical composition and photophysics of a blend film on a scale of a few nanometer.

In addition to the organic blend films, metallic nano-particles or lithographically fabricated nanostructures are also investigated using the gap mode hyperspectroscopic imaging.

This chapter is based on:

Wang, X.; Zhang, D.; **Braun, K**.; Egelhaaf, H. J.; Brabec, C. J.; Meixner, A. J., "High-Resolution Spectroscopic Mapping of the Chemical Contrast from Nanometer Domains in P3HT:PCBM Organic Blend Films for Solar-Cell Applications". *Adv. Funct.. Mat.* **2010,** *20* (3), 492-499.

Zhang, D.; Wang, X**.; Braun, K**.; Egelhaaf, H. J.; Fleischer, M.; Hennemann, L.; Hintz, H.; Stanciu, C.; Brabec, C. J.; Kern, D. P.; Meixner, A. J., "Parabolic mirror-assisted tip-enhanced spectroscopic imaging for non-transparent materials". *Journal of Raman Spectroscopy* **2009,** *40* (10), 1371-1376.

High-Resolution Spectroscopic Mapping of the Chemical Contrast from Nanometer Domains in P3HT:PCBM Organic Blend Films for Solar-Cell Applications

By *Xiao Wang, Dai Zhang,* Kai Braun, Hans-Joachim Egelhaaf, Christoph J. Brabec,* and *Alfred J. Meixner**

A high-resolution near-field spectroscopic mapping technique is successfully applied to investigate the influence of thermal annealing on the morphology of a poly(3-hexylthiophene) and [6,6]-penyl-C_{61} butyric acid methyl ester (P3HT:PCBM) blend film. Based on the simultaneously recorded morphological and spectroscopic information, the interplay among the blend film morphology, the local P3HT:PCBM molecular distribution, and the P3HT photoluminescence (PL) quenching efficiency are systematically discussed. The PL and Raman signals of the electron donor (P3HT) and acceptor (PCBM) are probed at an optical resolution of approximately 10 nm, which allows the chemical nature of the different domains to be identified directly. In addition, the local PL quenching efficiency, which is related to the electron transfer from P3HT to PCBM, is quantitatively revealed. From these experimental results, it is proposed that high-resolution near-field spectroscopic imaging is capable of mapping the local chemical composition and photophysics of the P3HT:PCBM blends on a scale of a few nanometers.

1. Introduction

Solar cells based on blends of conjugated polymers and fullerenes offer promising alternatives in the development of a new generation of low-cost and flexible photovoltaic devices.[1] Using blends of poly-(3-hexylthiophene) and [6,6]-penyl-C_{61} butyric acid methyl ester (P3HT:PCBM), which have both been intensely used as electron donor and acceptor in organic solar cell devices, respectively, 5% energy-conversion efficiencies have been achieved.[2,3] One of the main factors affecting the power-conversion efficiency of P3HT:PCBM solar cells is the efficiency of creation and dissociation of electronically excited states (excitons).[4] Whilst exciton creation is determined by the absorption efficiency of P3HT, exciton dissociation at the donor/acceptor interface is highly related to the local morphology and distribution of P3HT and PCBM.[5] Therefore, the blend film morphology has to be carefully tailored to optimize the total efficiency of the solar cell.[6,7] The ideal blend should phase segregate to form bulk heterojunctions endowing a bicontinuous dispersion of P3HT and PCBM with the mean domain size commensurate with the exciton diffusion length (5–10 nm) and a maximum interfacial area for exciton dissociation. Each of the two phases should be highly crystalline, thus, enabling effective hole- and electron transport. Thermal annealing has widely been employed as an effective postproduction treatment for achieving this goal.[8,9] However, the selection of optimal annealing time and temperature has, so far, only been achieved empirically because of a lack of sufficient information about the internal order of the active layer and the regional organization of the composites on a scale matching the ideal length scale for exciton diffusion/dissociation and electron/hole transport. Therefore, a better understanding of the blend film morphology evolution during postproduction treatment and device performance is essential and urgently needed.[10,11] Several techniques such as aperture scanning near-field optical microscopy (SNOM),[12,13] scanning Kelvin probe microscopy (SKPM),[14,15] near-field scanning photocurrent microscopy (NSPM),[16,17] and conducting atomic force microscopy (C-AFM)[18,19] have been employed for this purpose. Although these techniques are sufficient to obtain high-resolution information on

[*] Dr. D. Zhang, Prof. A. J. Meixner, X. Wang, K. Braun
Institute of Physical and Theoretical Chemistry
University of Tübingen
Auf der Morgenstelle 8, 72076 Tübingen (Germany)
E-mail: dai.zhang@uni-tuebingen.de;
alfred.meixner@uni-tuebingen.de
Dr. H.-J. Egelhaaf, Dr. C. J. Brabec
Konarka Technologies GmbH
Landgrabenstr. 94, 90443 Nürnberg (Germany)
Dr. C. J. Brabec
Lehrstuhl für Werkstoffe der Elektronik- und Energietechnik
Friedrich-Alexander-Universität Erlangen-Nürnberg
Martensstraße 7, 91058 Erlangen (Germany)
Dr. C. J. Brabec
Bayerisches Zentrum für Angewandte Energieforschung (ZAE Bayern)
Martensstraße 7, 91058 Erlangen (Germany)

www.MaterialsViews.com

ADVANCED
FUNCTIONAL
MATERIALS

www.afm-journal.de

FULL PAPER

the morphology, corresponding information about the local charge-transfer efficiency is either impossible to obtain or can only be monitored at a macroscopic spatial resolution, which is far from matching the exciton diffusion length.

Recently developed tip-enhanced near-field optical microscopy provides an innovative approach for studying this topic from a different perspective. The basic principle of this technique is to employ a sharp metal tip as an optical antenna to approach the sample surface very closely using a sensitive feedback mechanism based on a tunneling current[20] or mechanical force.[21] In this way the topography and the correlated chemical information can be recorded simultaneously via Raman- or IR spectroscopy.[22] The topographic resolution of this technique reaches down to a few nanometers or even the atomic scale whereas the optical resolution is essentially determined by the apex size of the antenna tip.[23] Employing this technique to study the P3HT:PCBM blend film allows not only to obtain correlated topographical and optical information (Raman and photoluminescence (PL)) at resolutions on the nanometer scale but it also endows ultrahigh sensitivity, enabling, for instance, the detection of a single molecule.[24] In addition, whereas PL intensity variations reflect the efficiency of charge generation at the P3HT:PCBM interface,[25] Raman spectroscopy, which is very sensitive to the degree of π-electron delocalization along the chain axis of conjugated polymers, shows nanoscale changes in morphology by monitoring the vibrational modes of the P3HT polymer chains that are involved in electronic transitions. Therefore, spectroscopic mapping of the PL and Raman signals from the P3HT:PCBM blend film on the submicrometer or even nanometer scale correlated with the obtained morphological information is promising for the investigation of organic blend films on the nanometer scale and for a better understanding of the relationship between the blend film morphology and charge generation.

In this paper we demonstrate the application of confocal and near-field optical microscopy in the study of local Raman and PL intensity variations with respect to morphology changes of a P3HT:PCBM blend-film model system, which was fabricated on a silicon wafer upon thermal annealing for 5 min. or 30 min. at 140 °C. We show how the molecular distributions of P3HT and PCBM in the composite can be distinguished chemically on the submicrometer and nanometer scale using near-field spectroscopic mapping techniques. Furthermore, the correlation of the Raman features of the P3HT phase with its crystallinity on the submicrometer scale is shown. The interplay between the blend film morphology, the local distribution of P3HT:PCBM, and the P3HT PL quenching efficiency is also discussed.

2. Results and Discussion

To derive the optical information for determining the presence of P3HT and PCBM, we first collected the PL and Raman fingerprint information of pristine P3HT and PCBM thin films by confocal optical microscopy. Figure 1a shows the PL emission profiles
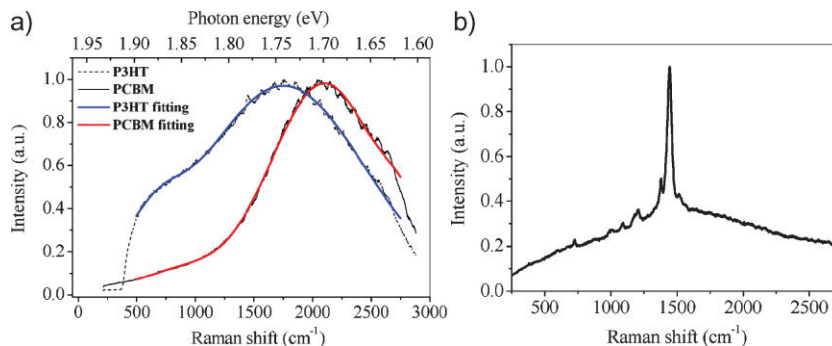

Figure 1. a) Normalized spectra collected from pristine P3HT and pristine PCBM thin films. b) Confocal Raman spectrum of P3HT.

together with the corresponding fitted curves for both the pristine P3HT polymer and a PCBM film. The maximum PL emissions from P3HT and PCBM appear at 1.74 eV (Raman shift of 1750 cm^{-1} vs. the He–Ne laser line) and 1.70 eV (Raman shift of 2100 cm^{-1} vs. the He–Ne laser line), respectively. The emission profiles collected from the P3HT and PCBM pristine films seem different from their conventional PL emission spectra.[26,27] This is related to the cut-off side effect of our laser-blocking filters in the shorter wavelength region and to the decreasing CCD camera efficiency in the longer wavelength region. Under 632.8 nm He–Ne laser illumination the P3HT polymer exhibits well-defined Raman peaks at 1450, 1380, 1210, 1090, 997, and 724 cm^{-1} (see Fig. 1b), which are assigned to C=C stretching, C−C stretching, a combination of C−C stretching and C−H bending, C−H bending, C−C stretching, and C−S−C deformation vibrations, respectively.[28] The Raman peaks from the pristine PCBM film were not distinguishable under our experimental conditions. Therefore, the different PL emission maxima of P3HT and PCBM as well as the strong Raman C=C stretching vibration of P3HT (1450 cm^{-1}) were used to determine the presence of both components and to calculate the P3HT luminescence quenching efficiency in the P3HT:PCBM blend film.

2.1. Confocal Spectroscopic Mapping

Figure 2a shows the confocal optical image collected by the avalanche photodiode (APD) from a P3HT:PCBM blend film that had been thermally annealed at 140 °C for 30 min. The bright region in the center of the image indicates the place where more photons are emitted or inelastically scattered as compared to the dark regions. On the same area, we performed confocal spectroscopic mapping experiments by collecting 32 × 32 spectra during the laser focus raster scanning the 10 μm × 10 μm scan area. Figure 2b shows the optical image obtained by integrating the spectral intensity of the 32 × 32 mapping spectra from 223 cm^{-1} to 2886 cm^{-1}. Similar to the optical image collected by the APD, stronger optical signals are detected from the center of the tested region. To determine the origin of this strong optical signal, we fitted all of the 32 × 32 spectra according to the PL emission profiles from pristine P3HT and PCBM PL (Gaussian fitting function), and the P3HT Raman peaks (Lorentzian fitting
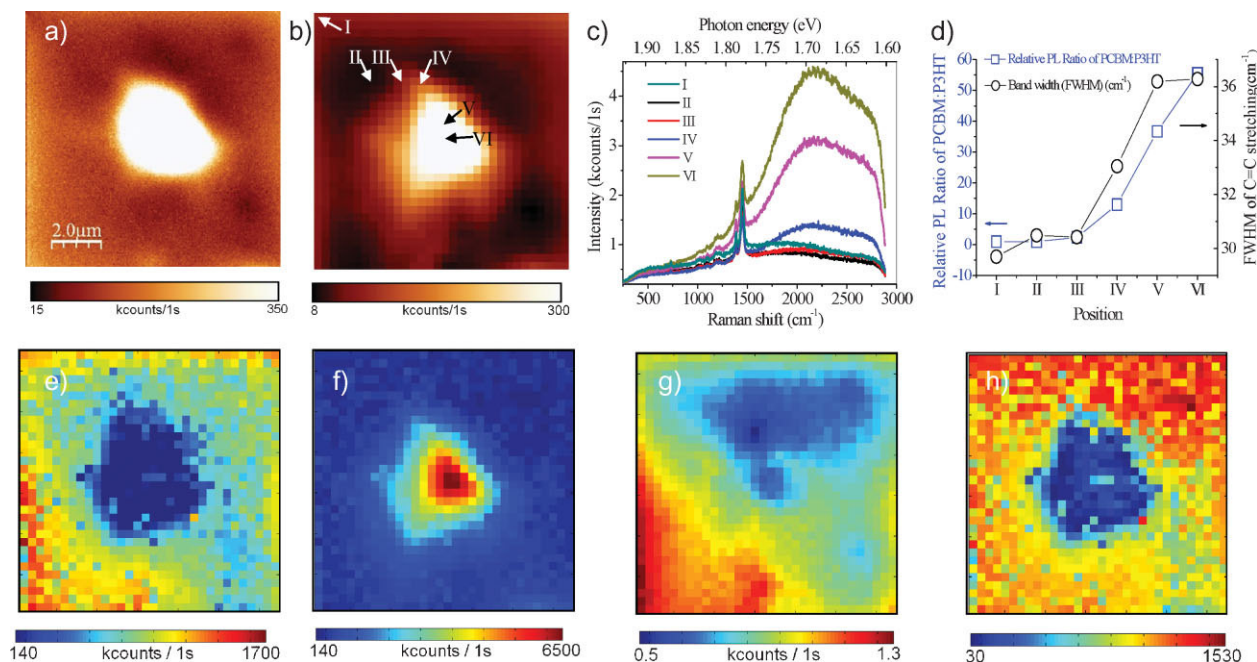
FULL PAPER

Figure 2. a) Confocal optical image recorded with an APD. b) Confocal image of the same scan area obtained by summing the total spectral pixel intensity from 223 cm^{-1} to 2886 cm^{-1}. c) Confocal spectra collected at positions I, II, III, IV, V, and VI as indicated in (b) composed of Raman and PL contributions. d) The relative PL ratios between PCBM and P3HT (curve labeled with blue open rectangles), and the FWHM of the P3HT C=C stretching vibrational Raman peaks (curve labeled with black open circles) at positions I, II, III, IV, V, and VI. e–g) Intensity distributions of P3HT PL (e), PCBM PL (f), and P3HT C=C vibrational Raman intensity (g) in the same scan area. h) P3HT PL quenching efficiency in the scan area (pixel by pixel ratio of the values from (e) and (g)). Scan area: 10 µm × 10 µm. The sample was thermally annealed at 140 °C for 30 min. Laser power: 250 µW. Acquisition time: 1 s per spectrum.

function). To demonstrate the evolution of the optical signals, several spectra collected at positions I, II, III, IV, V, and VI (indicated in Fig. 2b) are shown in Figure 2c (their fitted spectra are shown in Fig. S1 in the Supporting Information). The broad features of the spectra collected at the optically bright areas IV, V, and VI show the characteristic PCBM PL emission maximum at ca. 2100 cm^{-1} indicating the presence of large amounts of PCBM in this region. In contrast, the backgrounds of the spectra that were collected from the optically dark regions I and II are dominated by strong emissions at 1750 cm^{-1}, which is typical for the pristine P3HT film. The spectrum collected from position III shows a background line shape that falls in between that of the P3HT PL dominated (position I and II) and the PCBM PL dominated situations (position IV, V, and VI). Figure 2d shows the relative PL ratios of PCBM against P3HT (curve labeled with blue open rectangles), and the FWHM of the P3HT C=C stretching Raman peak (curve labeled with black open circles) at positions I, II, III, IV, V, and VI. The PL ratio of PCBM: P3HT at point VI is about 60 times larger and the FWHM of P3HT C=C stretching Raman peak is ca. 7 cm^{-1} broader than that at position I. As has been pointed out before, since the thiophene rings in the P3HT molecules are more closely stacked when the polymer is highly crystalline, the increased crystallite size and better internal order within the P3HT domains obtained by annealing leads to the narrowing of the C=C stretching Raman peak.[29] Our experiments clearly demonstrate that the presence of large PCBM aggregates deteriorates the regio-regularity of the P3HT molecules. Similarly, P3HT C=C Raman peak broadening effects have been reported by Yun et al.[30] at 1 µm

optical resolution comparing a series of P3HT:PCBM blend films that had been thermally annealed at different temperatures from 413 K to 300 K. We observed a similar effect and were able to clearly resolve the worsening of the P3HT local crystallinity at a spatial resolution of ca. 300 nm.

Based on the fitted 32 × 32 confocal mapping spectra, overview pictures of the PL intensity distributions of P3HT and PCBM, and the distribution of the Raman intensity of the P3HT molecules (derived from the intensity of the P3HT C=C Raman vibrational peak at 1450 cm^{-1}) in this area are shown in Figures 2e, f, and g, respectively. Correlated with the strong optical signals observed by the APD, a comparison between Figures 2e and f clearly demonstrates that the PCBM PL is responsible for the detected strong optical signals. A continuous decrease of the PCBM PL is observed around the big PCBM aggregate in the figure. P3HT molecules are distributed all over the tested sample area, even within the micrometer-sized PCBM island. However, the distribution of P3HT molecules is extremely inhomogeneous, which is strongly related to the presence of PCBM aggregates. For example, close to the PCBM big aggregate at the upper right hand side of this tested area, fewer P3HT molecules are present (Fig. 2g). We derived the P3HT PL quenching efficiency (Fig. 2h) by normalizing Figure 2e with Figure 2g. The red-colored region indicates places where the P3HT PL is less efficiently quenched than in the blue region. As is well known for the P3HT:PCBM organic solar-cell system, the degree of P3HT PL quenching is directly related to the extent of exciton dissociation by electron transfer to the PCBM.[26] Our study demonstrates that the regions
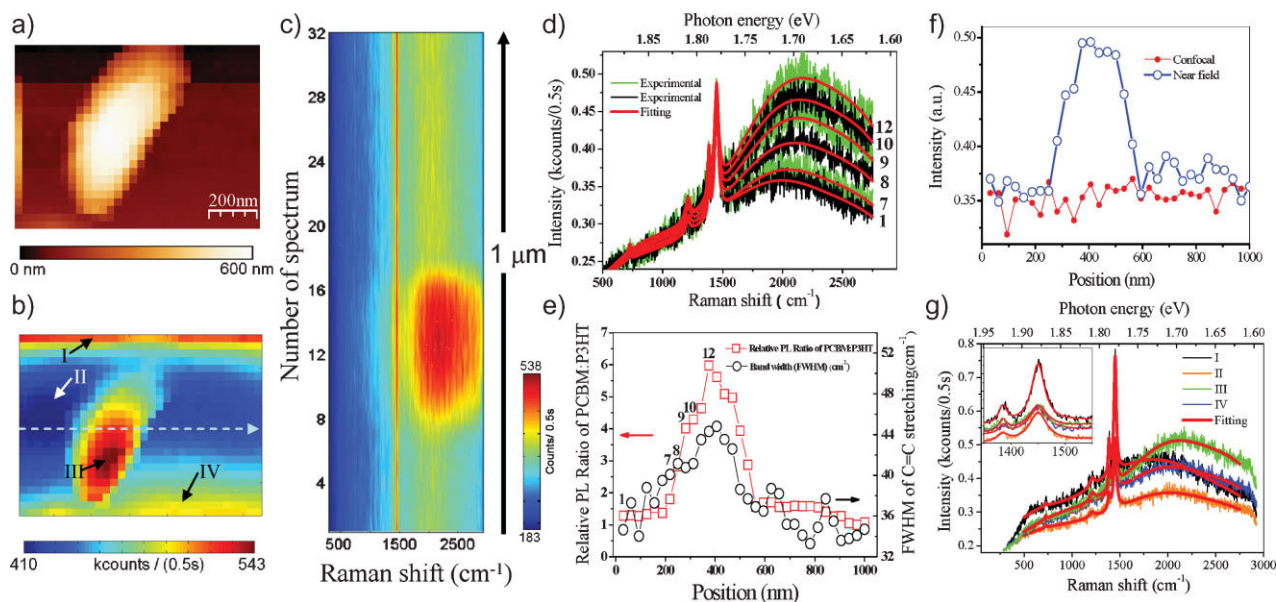
Materials
Views
www.MaterialsViews.com

ADVANCED
FUNCTIONAL
MATERIALS
www.afm-journal.de

FULL PAPER

Figure 3. a) Topographical image. b) Near-field spectroscopic mapping image obtained by summing the total spectral intensity from 283 cm^{-1} to 2926 cm^{-1}. c) 32 Spectra extracted from a line scan (1 μm), the position of which is indicated by the arrow in (b). d) Comparisons of several spectra extracted from the Raman line mapping sequence shown in (c). The green and black spectra are the experimental data whilst the red curves are the fitted spectra. e) The relative PL ratios between PCBM and P3HT (curves labeled with red open rectangles) and the FWHM changes of the P3HT C=C stretching Raman peaks (curves labeled with black open circles) along the line indicated in (b). f) Comparison of the near-field and confocal spectroscopic mapping along the same line indicated in (b). The optical signals plotted here are derived from the PCBM PL intensities. g) Near-field spectra collected at positions I, II, III, and IV as indicated in (b). The red curves are the fitting spectra. The inset figure shows the enlarged spectra from 1350 cm^{-1} to 1550 cm^{-1}. The sample was thermally annealed at 140 °C for 30 min. Scan area: 1 μm ×0.75 μm. Laser power: 250 μW. Acquisition time: 0.5 s per spectrum.

of highest P3HT PL quenching efficiency correlate with the location of PCBM aggregates because of the high concentration of acceptor molecules in these regions. Outside of the PCBM clusters, where the PCBM concentration is smaller, the quenching of the P3HT PL is much less efficient. Although the PL from the P3HT molecules located inside the PCBM aggregates is effectively quenched by efficient electron transfer, solar cell devices using the 30-min. annealed blend films exhibit extremely unsatisfactory cell efficiencies. This can mainly be attributed to the reduced overall quenching efficiency of excitons, because the formation of PCBM aggregates leads to large PCBM-depleted areas where the excited states of P3HT are much less efficiently quenched.

2.2. Near-Field Spectroscopic Mapping

2.2.1. P3HT:PCBM Blend Films Subjected to 30 Minutes of Annealing at 140 °C

Despite the rich information obtained by the confocal spectroscopic mapping, this technique only allowed us to study optical events occurring on the scale of several hundreds of nanometers, because of the diffraction-limited optical resolution. To push the optical resolution further down to the nanometer regime, we employed a near-field spectroscopic mapping technique. Figure 3 shows the correlated topographical and near-field spectroscopic mapping images obtained from a blend film that had been thermally annealed for 30 min. The scanning area was 1000 nm

×750 nm (32 × 24 data points). In the middle of the topographic image (Fig. 3a), an ellipsoidal island with a maximum width of 300 nm and maximum height of 500 nm is observed. The corresponding near-field mapping image (Fig. 3b), obtained by summing the total spectral intensity from 283 cm^{-1} to 2926 cm^{-1} shows intense optical signals at the location of the island. A gradually decreasing optical intensity from the maximum height of the island to the flat area is clearly resolved. Figure 3c displays a stack of 32 Raman spectra taken from a one-line near-field spectroscopic map (1 μm) along the arrow indicated in Figure 3b. Whereas the P3HT Raman peak at 1450 cm^{-1}, represented by the red line across Figure 3c, indicates the presence of P3HT molecules throughout this region, a clear optical signal evolution in the range from 1600 to 2600 cm^{-1}, corresponding to the PCBM PL, is observed following the one-line scan. A more detailed inspection of the spectra numbered with the same sequence as in Figure 3c, are plotted in Figure 3d as green and black curves. The fitted spectra (detailed information shown in Fig. S2 in the Supporting Information) are shown as red curves. Going from spectrum 7 to 12 it can be seen that the PCBM molecules tend to aggregate more and more severely as supported by the PCBM PL increase and the topographically obvious clustering. The approximate PL ratios of PCBM against P3HT and the FWHM of the P3HT C=C stretching Raman vibrational peak along this one-line scan are presented in Figure 3e. Similar to what was observed in Figure 2d, the FWHM of the C=C stretching Raman peaks broadened in the regions where the PL ratio of PCBM versus P3HT was larger. Going from spectrum 1 to 12, the PL ratio of PCBM against P3HT increases about 6 times. Correspondingly, the

ADVANCED
FUNCTIONAL
MATERIALS
www.afm-journal.de

Materials
Views
www.MaterialsViews.com

FWHM of the P3HT C=C stretching Raman vibrational peak increases by about $10 \, cm^{-1}$, indicating that the increasing clustering of PCBM induces reduced crystallinity of the P3HT domain.[30] The information reported above cannot be obtained by confocal spectroscopic mapping because of the diffraction-limited laser focus size. This is demonstrated in Figure 3f where the blue curve labeled with open circles, obtained using the near-field spectroscopic mapping technique, indicates the PCBM PL variations along the arrow shown in Figure 3b, whilst the red curve labeled with dots and showing no obvious optical signals changes was obtained using confocal spectroscopic mapping. Besides the optical contrasts revealed along the one-line mapping, Figure 3b also demonstrates strong optical contrasts at positions numbered I, II, III, and IV. To clarify the origin of this optical contrast, spectra collected from these different positions are shown in Figure 3g. The inset in Figure 3g shows the enlarged spectra in the range of $1350 \, cm^{-1}$ to $1550 \, cm^{-1}$. All the bold red curves are fitting curves. The spectral background collected at position III is dominated by the PL of PCBM with its maximum appearing at about $2100 \, cm^{-1}$. The spectrum collected from position I exhibits a spectral line shape with a PL maximum at about $1750 \, cm^{-1}$, which is typical for the P3HT PL emission line profile. The spectra collected at positions II and IV present a strong background intensity over the whole spectral range between around 1750 to $2100 \, cm^{-1}$ indicating that both P3HT and PCBM PL contribute to the spectral intensity. In addition, as shown in the inset of Figure 3g, the FWHM increases in the sequence of positions I, II, IV, and III, indicating that the regio-regularity of P3HT is the best at position I.

To get a deeper insight into the molecular distribution and the PL quenching efficiencies of P3HT in this area, we processed all the 32×24 spectra with the same fitting method mentioned above. Figure 4a, b, and c show the PL intensity distribution of P3HT and PCBM, and the molecular distribution of P3HT (derived from the intensity variations of the P3HT C=C vibrational Raman peak). The strong PCBM PL emission dominates the optical signals from the island (Fig. 4b), indicating larger PCBM aggregates. The P3HT molecules are distributed homogeneously in most parts of this region except for the P3HT-rich top part, as demonstrated in Figure 4c. Normalizing Figure 4a with Figure 4c, the P3HT PL quenching efficiency was obtained (Fig. 4d). Similar to what was observed from the confocal spectroscopic mapping measurements (Fig. 2h), the highest P3HT PL quenching efficiency correlates with the region where larger PCBM aggregates are present. Notably, the lowest P3HT quenching efficiency is found in the lower region of the sample. The smaller P3HT quenching efficiency in the lower region may be related to the lower amount of P3HT:PCBM interfaces through enhanced phase segregation as compared to that in the island region. Hence, the P3HT PL quenching via exciton dissociation and electron transfer to the PCBM LUMO is hindered, giving rise to an increased PL emission in this region.

2.2.2. P3HT:PCBM Blend Films Subjected to 5 Minutes of Annealing at 140 °C

For comparison with the 30-min. annealed sample as shown above, P3HT:PCBM blend films subjected to 5 minutes of annealing at 140 °C, which led to a near-optimum solar-cell performance, were
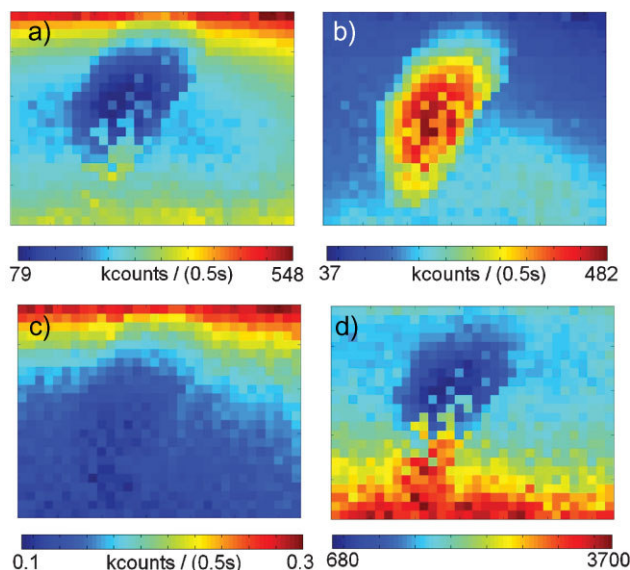

Figure 4. a–c) PL intensity distribution of P3HT (a), PCBM (b), and C=C vibrational Raman intensity (c) of P3HT in the same scan area as shown in Figure 3. d) P3HT PL quenching efficiency in the scan area (pixel by pixel ratio of the values from (a) and (c)). Scan area: $1 \, \mu m \times 0.75 \, \mu m$. The sample was thermally annealed at 140 °C for 30 min.

investigated with the spectroscopic mapping method. Different to what was observed for the 30-min. annealed sample, the 5-min. annealed sample showed homogeneous optical signals over an area of several tens of micrometers under confocal microscopic inspection. However, using the near-field spectroscopic mapping technique, distinctive optical contrast correlated with nanometer-sized topographical features is seen to appear (Fig. 5). The topographical image (Fig. 5a) taken over a region of 300 nm × 244 nm (32×26 data points) demonstrates the presence of ellipsoidal islands that are similar in shape to those observed for the 30-min. annealed blend film (Fig. 3a) but are of a much smaller size (heights lower than 60 nm and lateral diameters smaller than 100 nm). Despite of the non-optimized image resolution caused by a lack of pixels, some fine lengthy structures were observed next to the islands, which might, considering their structural dimensions, be the P3HT fibrils reported previously by J. Loos' group.[31] Further measurements are undertaken to verify this. Figure 5b displays the simultaneously obtained near-field spectroscopic mapping image by summing the total spectral intensity from $220 \, cm^{-1}$ to $2882 \, cm^{-1}$. The near-field imaging was capable of resolving the optical contrast at a pixel size of about 9 nm (indicated by the black arrows in Fig. 5a and b) between the two nanometer-sized islands in Figure 5a, which indicates that the optical resolution of our near-field spectroscopic imaging technique is on the order of at least 9 nm. This value is important for us not only because it breaks the resolution record from the point of view of optical microscopy; but also because it matches the P3HT exciton diffusion length that has recently been reported as being $8.5 \pm 0.7 \, nm$ by Shaw et al.[32] Figure 5c compares the topographic profile (black curve with open squares) and the correlated optical signal profile (red curve with open circles) along the dashed lines indicated in Figure 5a and 5b. The weakest optical intensity correlates with the locations of the ellipsoidal islands and the
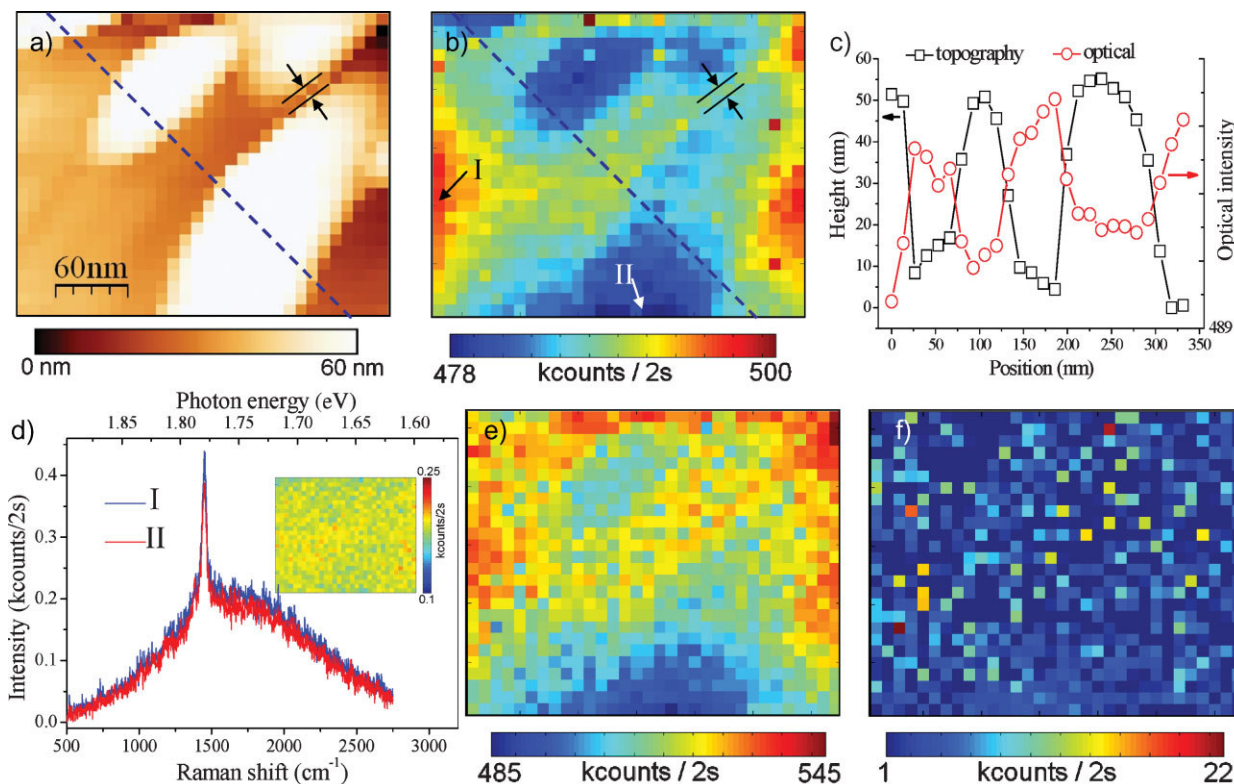
496

WILEY
InterScience®
DISCOVER SOMETHING GREAT

© 2010 WILEY-VCH Verlag GmbH & Co. KGaA, Weinheim

Adv. Funct. Mater. **2010**, 20, 492–499

www.MaterialsViews.com

ADVANCED
FUNCTIONAL
MATERIALS
www.afm-journal.de

FULL PAPER

Figure 5. a) Topographical and b) near-field optical images. The optical intensities were derived by summing the total spectral pixel intensity from 220 cm^{-1} to 2882 cm^{-1}. c) The correlation between the height and the optical intensities along the line indicated in (a) and (b). d) The tip-enhanced Raman spectra collected from positions I (blue spectrum) and II (red spectrum) as indicated in (b). The inset figure shows the C=C vibrational Raman intensity of P3HT in the same scan area. e,f) PL intensity distributions of P3HT (e) and PCBM (f) in the same scan area. The sample was thermally annealed at 140 °C for 5 min. Laser power: 250 μW. Acquisition time was 2 s per spectrum.

strongest optical intensity appears in the topographically flat regions.

To trace the origin of the optical signals observed, we carefully fitted and compared the 32×26 spectra collected during the spectroscopic imaging. In contrast to the 30-min. annealed blend film which showed dramatic spectral changes because of the local variations in the PCBM PL or the P3HT PL intensity, all the 32×26 spectra collected from the 5-min. annealed sample are dominated by P3HT PL emission. In addition, the intensity and the FWHM of the P3HT Raman peak are similar over the whole sample area, indicating a homogeneous P3HT molecular distribution and similar crystallinity. The optical contrast observed in Figure 5b is induced by slight total spectral intensity variations. As shown in Figure 5d, the two spectra collected from positions I and II (as indicated in Fig. 5b), where the most distinctive optical contrasts were observed, exhibit only tiny spectral intensity differences. The inset in Figure 5d shows the C=C vibrational Raman intensity of the P3HT distribution in the same scan area as Figure 5a. Figure 5e and f shows the PL intensity distributions of P3HT and PCBM, respectively, in this scan area. The P3HT PL variations dominate the optical contrast observed in this region, whilst the PL from PCBM is extremely weak. In addition, the variations of P3HT PL correlate with the positions of the islands, indicating that within the moderate-sized PCBM aggregates P3HT excitons are efficiently dissociated. The extremely weak PCBM PL emission

indicates that the PCBM molecules cluster into aggregates that are of a much smaller size than those in the 30-min. annealed sample; hence the radiative recombination of PCBM excitons within the PCBM aggregates is less likely to occur in the 5-min. annealed sample.

To summarize the two blend film conditions that we have studied above, Figure 6 shows sketches of the PCBM aggregates
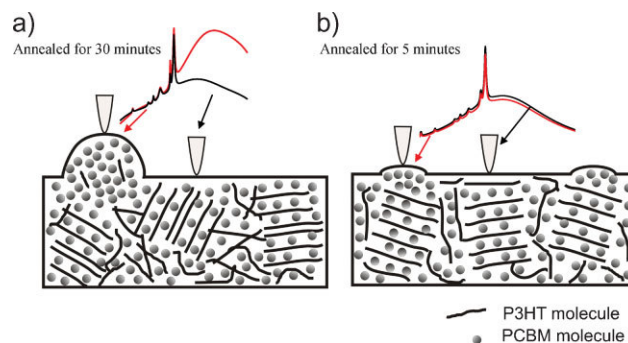

Figure 6. P3HT:PCBM blend films after a) 30-min. and b) 5-min. thermal annealing at 140 °C. The red spectra were collected when the tip was positioned above the regions where PCBM aggregates were present. The black spectra were collected when the tip was away from the PCBM aggregates.

dispersed in the P3HT:PCBM blend film upon 30-minutes (left picture) or 5-min. thermal annealing (right picture). The red spectra were collected when the tip was positioned above the regions where PCBM aggregates were present. The black spectra were collected when the tip was away from the PCBM aggregates. For the 30-min. annealed blend film, the PCBM molecules aggregate into micrometer-sized isolated clusters, whilst upon 5-min. thermal annealing PCBM forms nanometer-sized clusters. Devices based on the 5-min. annealed blends showed maximum performance while devices comprising 30-min. annealed films performed significantly worse. This shows that nanometer-sized PCBM clusters that are distributed inside the blend film endow the optimum compromise between a large electron donor/acceptor interface for efficient exciton dissociation and sufficient domain size for efficient electron transport along continuous percolation paths in both materials.

3. Conclusions

Both confocal and near-field spectroscopic mapping techniques were used to study the interplay between the morphology, molecular distribution, and P3HT PL quenching efficiency of P3HT:PCBM blend films that had been annealed at 140 °C for 30 minutes or 5 minutes. Upon 30-min. annealing, micrometer-sized PCBM aggregates were observed showing strong PCBM PL emission. These aggregates still contained small concentrations of P3HT, as evident from the Raman spectra. The FWHM of the P3HT C=C stretching Raman peak inside these PCBM clusters was broadened because of the local disturbance by the large PCBM aggregates, indicating a reduced crystallinity of the P3HT in these regions. Upon 5-min. annealing, the PCBM molecules formed nanometer-scale aggregates from which no obvious PL emission was observed. Despite of the homogeneous molecular distribution and crystallinity, the P3HT PL variations correlated closely to the presence of the PCBM aggregates because of the abundance of electron donor/acceptor interfaces for dissociating the P3HT excitons. We probed the PL and Raman signals of the donor and acceptor materials which allowed the direct identification of the chemical nature of the different domains. Moreover, we were able to reveal and quantify local quenching, which is related to the electron transfer from P3HT to PCBM. Based on the above reported research, we would like to contend that high-resolution near-field spectroscopic imaging is capable of mapping the local chemical composition and photophysics of P3HT:PCBM blends on a length scale of only a few nanometers.

It should be noted that compared to real organic solar cells based on P3HT:PCBM blend films, which are normally fabricated on PEDOT:PSS/ITO substrates, our model P3HT:PCBM blend films were fabricated on a silicon substrate and thus the films may have formed oversized aggregates because of PCBM nucleation on the oxide surface during thermal annealing. In order to improve the correlation between our observation and the real-device situation, we are currently investigating the influence of thermal annealing on a P3HT:PCBM blend film fabricated on a PEDOT:PSS/ITO substrate, which will be discussed in the future with respect to the corresponding device efficiency.

4. Experimental

Photovoltaic layers, consisting of P3HT (number-average molecular weight 83 000 g mol^{-1}, weight-average molecular weight 113 000 g mol^{-1}; RR = 95%) and a methanofullerene PCBM ([6,6]-phenyl-C$_{61}$-butyric acid methyl ester) in 1:1 (w/w) ratios were dissolved at a concentration of 1 wt. % in o-xylene. The solution was deposited on silicon wafers (with native oxide layer) by doctor blading at 65 °C. After drying, the layers were annealed at 140 °C for 5 and 30 minutes, respectively, under nitrogen atmosphere. All the samples were provided by Konarka Technologies GmbH.

A home-built parabolic-mirror-assisted confocal optical microscope was used to optically investigate the distribution of the P3HT and PCBM composites at an improved diffraction-limited resolution [33]. To further improve the optical resolution to several tens of nanometers and for collecting the correlated topographical information, a tip scanner based on shear-force feedback was attached to this confocal optical microscope [34]. A 632.8-nm He–Ne laser was used for excitation, the PL and Raman signals from the blend film after passing through one laser line filter (6 OD) and one notch filter (6 OD) were collected either by an avalanche photodiode (APD) or by a liquid-nitrogen-cooled CCD camera coupled to a spectrometer. In the confocal far-field measurements, the spectroscopic mapping images were obtained by collecting 32 × 32 data points from the 10 μm × 10 μm sample area at a step width of ca. 310 nm, which was comparable to the diameter of the focus (260 nm). For the near-field measurements, sharp Au tips with apexes of ca. 10 nm diameter were normally used, giving a less than 10-nm diameter confined near-field focus point. 32 spectra were collected per one scanning line (1 μm or 300 nm) at a step width of around 31 or 9 nm, synchronizing with each topographical data point. Considering the size of the near-field focus point, the scanning step size provided us with the possibility of studying optical events occurring at two different scan data points without signal averaging.

[1] C. J. Brabec, N. S. Sariciftci, J. C. Hummelen, *Adv. Funct. Mater.* **2001**, *11*, 15.

[2] W. L. Ma, C. Y. Yang, X. Gong, K. Lee, A. J. Heeger, *Adv. Funct. Mater.* **2005**, *15*, 1617.

[3] G. Li, V. Shrotriya, J. S. Huang, Y. Yao, T. Moriarty, K. Emery, Y. Yang, *Nat. Mater.* **2005**, *4*, 864.

[4] T. Erb, U. Zhokhavets, G. Gobsch, S. Raleva, B. Stuhn, P. Schilinsky, C. Waldauf, C. J. Brabec, *Adv. Funct. Mater.* **2005**, *15*, 1193.

[5] N. S. Sariciftci, L. Smilowitz, A. J. Heeger, F. Wudl, *Science* **1992**, *258*, 1474.

[6] X. N. Yang, J. Loos, S. C. Veenstra, W. J. H. Verhees, M. M. Wienk, J. M. Kroon, M. A. J. Michels, R. A. J. Janssen, *Nano Lett.* **2005**, *5*, 579.

[7] H. Hoppe, N. S. Sariciftci, *J. Mater. Chem.* **2006**, *16*, 45.

[8] F. Padinger, R. S. Rittberger, N. S. Sariciftci, *Adv. Funct. Mater.* **2003**, *13*, 85.

[9] D. Chirvase, J. Parisi, J. C. Hummelen, V. Dyakonov, *Nanotechnology* **2004**, *15*, 1317.

[10] M. Campoy-Quiles, T. Ferenczi, T. Agostinelli, P. G. Etchegoin, Y. Kim, T. D. Anthopoulos, P. N. Stavrinou, D. D. C. Bradley, J. Nelson, *Nat. Mater.* **2008**, *7*, 158.

[11] B. C. Thompson, J. M. J. Fréchet, *Angew. Chem. Int. Ed.* **2008**, *47*, 58.

Materials
Views
www.MaterialsViews.com

ADVANCED
FUNCTIONAL
MATERIALS
www.afm-journal.de

FULL PAPER

[12] E. Klimov, W. Li, X. Yang, G. G. Hoffmann, J. Loos, *Macromolecules* **2006**, *39*, 4493.

[13] Y. C. Huang, Y. C. Liao, S. S. Li, M. C. Wu, C. W. Chen, W. F. Su, *Sol. Energy Mater. Sol. Cells* **2009**, *93*, 888.

[14] M. Chiesa, L. Burgi, J. S. Kim, R. Shikler, R. H. Friend, H. Sirringhaus, *Nano Lett.* **2005**, *5*, 559.

[15] H. Hoppe, T. Glatzel, M. Niggemann, A. Hinsch, M. C. Lux-Steiner, N. S. Sariciftci, *Nano Lett.* **2005**, *5*, 269.

[16] C. R. McNeill, H. Frohne, J. L. Holdsworth, P. C. Dastoor, *Nano Lett.* **2004**, *4*, 2503.

[17] C. R. McNeill, H. Frohne, J. L. Holdsworth, J. E. Furst, B. V. King, P. C. Dastoor, *Nano Lett.* **2004**, *4*, 219.

[18] D. C. Coffey, O. G. Reid, D. B. Rodovsky, G. P. Bartholomew, D. S. Ginger, *Nano Lett.* **2007**, *7*, 738.

[19] M. Dante, J. Peet, T. Q. Nguyen, *J. Phys. Chem. C* **2008**, *112*, 7241.

[20] B. Pettinger, B. Ren, G. Picardi, R. Schuster, G. Ertl, *Phys. Rev. Lett.* **2004**, *92*, 096 101.

[21] R. M. Stöckle, Y. D. Suh, V. Deckert, R. Zenobi, *Chem. Phys. Lett.* **2000**, *318*, 131.

[22] B. Ren, G. Picardi, B. Pettinger, R. Schuster, G. Ertl, *Angew. Chem. Int. Ed.* **2005**, *44*, 139.

[23] B. Pettinger, K. F. Domke, D. Zhang, R. Schuster, G. Ertl, *Phys. Rev. B* **2007**, *76*, 113 409.

[24] J. Steidtner, B. Pettinger, *Phys. Rev. Lett.* **2008**, *100*, 236 101.

[25] T. Röder, H. S. Kitzerow, J. C. Hummelen, *Synth. Met.* **2004**, *141*, 271.

[26] H. Hoppe, M. Niggemann, C. Winder, J. Kraut, R. Hiesgen, A. Hinsch, D. Meissner, N. S. Sariciftci, *Adv. Funct. Mater.* **2004**, *14*, 1005.

[27] M. Al-Ibrahim, H. K. Roth, U. Zhokhavets, G. Gobsch, S. Sensfuss, *Sol. Energy Mater. Sol. Cells* **2005**, *85*, 13.

[28] M. Baibarac, M. Lapkowski, A. Pron, S. Lefrant, I. Baltog, *J. Raman Spectrosc.* **1998**, *29*, 825.

[29] Z. H. Liao, J. E. Pemberton, *J. Phys. Chem. A* **2006**, *110*, 13 744.

[30] J. J. Yun, J. Peet, N. S. Cho, G. C. Bazan, S. J. Lee, M. Moskovits, *Appl. Phys. Lett.* **2008**, *92*, 251 912.

[31] S. S. van Bavel, E. Sourty, G. de With, J. Loos, *Nano Lett.* **2009**, *9*, 507.

[32] P. E. Shaw, A. Ruseckas, I. D. W. Samuel, *Adv. Mater.* **2008**, *20*, 3516.

[33] J. Stadler, C. Stanciu, C. Stupperich, A. J. Meixner, *Opt. Lett.* **2008**, *33*, 681.

[34] M. Sackrow, C. Stanciu, M. A. Lieb, A. J. Meixner, *ChemPhysChem* **2008**, *9*, 316.

Parabolic mirror-assisted tip-enhanced spectroscopic imaging for non-transparent materials

Dai Zhang[a]* Xiao Wang,[a] Kai Braun,[a] Hans-Joachim Egelhaaf,[b] Monika Fleischer,[c] Laura Hennemann,[a] Holger Hintz,[a] Catrinel Stanciu,[a] Christoph J. Brabec,[b] Dieter P. Kern[c] and Alfred J. Meixner[a]*

A versatile and efficient tip-enhanced spectroscopic imaging technique based on a parabolic mirror (PM) assisted near-field optical microscope is demonstrated. The replacement of the conventional objective lens with a parabolic mirror allows the non-restricted investigation of sample materials regarding their opacity. In addition, an improved signal collection efficiency and effective excitation of the longitudinal plasmonic oscillation in the tip apex are obtained. The capabilities of PM-assisted tip-enhanced Raman (TER) and photoluminescence (PL) imaging in distinguishing the individual domains made of different chemical components in poly (3-hexythiophene)/[6, 6]-penyl-C_{61} butyric acid methyl ester (P3HT/PCBM) solar cell blend film and in the investigation of the plasmonic properties of geometrically well-defined Au cones are demonstrated. Copyright © 2009 John Wiley & Sons, Ltd.

Supporting information may be found in the online version of this article.

Introduction

The combination of spectroscopic [Raman fingerprint and photo luminescence (PL)] imaging and scanning probe microscopy at both optical and spatial resolutions on the nanometer scale is one of the topmost goals that tip-enhanced spectroscopic technique has targeted ever since its invention.[1] A satisfactory combination of both techniques is not trivial. Besides the stringent requirements regarding the long-time stability of the instrumentation that should be capable of maintaining the tip–sample distance and reproducibly positioning the tested species with ultra-high accuracy, at least two more technical problems have to be carefully considered.

The first problem concerns the capability of handling non-transparent sample substrates. Tip-enhanced spectroscopy and microscopy based on the inverted confocal microscope, the most commonly adopted configuration nowadays, have been restricted to transparent sample substrates since years.[2,3] The intrinsic reason is due to the position of the objective lens that is placed below the sample for laser focusing and optical signal collection. Transparent substrates, such as mica[4] and glass[5] or ultra-thin metal films with a thickness allowing enough laser power of a certain frequency to penetrate through, are strictly required, which greatly limits the capability of this technique in a variety of fields ranging from the fundamental scientific research to the practical industrial application. A side illumination configuration where a *p*-polarized laser beam is directed to the tip antenna from a large tilted angle *versus* the sample surface is proved to be an effective solution regarding this problem.[6] However, at least two issues need to be considered carefully. Firstly, the focal

spot projected from the side on the sample surface illuminates a large sample area in confocal mode leading to an increased optical background. Secondly, only a small fraction of the optical signals scattered or radiated can be collected because of the limited numerical aperture (NA) and the position of the lens as well as a partial shadowing of the signal by the tip shaft. These issues influence strongly the reliability and accuracy of a tip-enhanced spectroscopic imaging picture, which critically requires a homogeneous distribution of the near-field below the tip apex, a maximum signal – collection efficiency from all the angles above the sample surface and a minimum contribution of the confocal optical signal from the far-field focus illuminated sample area.

The second problem is how to precisely and selectively image the optical signals of interest. A tip-enhanced Raman (TER) spectrum normally exhibits well-defined Raman peaks superimposed on a broad and strong background. This background mainly consists of the PL from the excited tip antenna, Raman and PL

* Correspondence to: Dr. Dai Zhang and Prof. Alfred J. Meixner, Institute of Physical and Theoretical Chemistry, University of Tuebingen, Auf der Morgenstelle 8, 72076, Tuebingen, Germany.
  E-mail: dai.zhang@uni-tuebingen.de; alfred.meixner@uni-tuebingen.de

a Institute of Physical and Theoretical Chemistry, University of Tuebingen, Auf der Morgenstelle 8, 72076 Tuebingen, Germany

b Christian-Doppler-Lab for Surface Optical Methods, Johannes-Kepler-University and Konarka GmbH, Altenbergerstr. 69, A-4040 Linz, Austria

c Institute of Applied Physics, University of Tuebingen, Auf der Morgenstelle 10, 72076, Tuebingen, Germany

from the independent sample and substrate, as well as the sample molecule–substrate compound when strong interaction, such as covalent bonding, occurs between the sample and the substrate. Since both the Raman and PL information provide characteristic insights into the properties of the tested species, it is helpful to distinguish and extract these two types of information from one spectrum. Recently there were several reports about TER and PL imaging based on band pass filters to select photons within a certain wavelength range.[7,8] The problems accompanying this method are the selectivity and versatility. More explicitly, the full width at half maximum (FWHM) of the band pass filter plays a decisive role for the selectivity and accuracy of the 'Raman information' collected. The usual FWHM of the commercially available band pass filters are at least 5 nm, which is much broader than the average FWHM of a Raman peak. Hence, a band pass filter is liable for providing false Raman imaging pictures, especially, for systems consisting of multi-Raman-active components that exhibit similar Raman features. In addition, intrinsically band pass filtering allows only for a wavelength selectivity whilst being incapable of separating, e.g. the inelastically scattered photons from the emitted PL photons. For true Raman imaging of the tested species, this method is vulnerable to the artefacts induced by the sample or substrate PL, especially when the PL intensity is stronger than the Raman intensity. Recently, Pettinger's group[9] reported the Raman imaging picture of a single brilliant cresyl blue (BCB) dye molecule absorbed on a Au (111) surface by integrating its Raman peak intensity between 568 and 572 cm^{-1}, which effectively eliminates the influence from the strong Au PL. Since they scan the tip antenna over the sample to collect the scanning tunneling microscopy (STM) and the tip-enhanced spectroscopic information, imaging areas larger than the size of the focus are difficult to scan owing to the tip moving out of the focus.

Considering the advantages and disadvantages of the methods discussed above, we converted the conventional design concept of a tip-enhanced optical microscope in developing a new type of instrumentation using a parabolic mirror as the laser focusing and signal collection element.[10,11] We fix the position of the tip apex precisely in the laser focus, whilst scanning the sample *versus* the tip apex by using a piezo-controlled scanning table for the spectroscopic imaging. We present here tip-enhanced optical images recorded by collecting the whole spectrum consisting of sharp Raman peaks and a dispersive PL background from every individual data point. Spectroscopic imaging pictures can be plotted either with the intensity integration of a certain Raman peak or the PL from a certain wavelength range via careful spectral fitting.

In this paper, we will introduce first some basic principles of PM optics and then demonstrate the versatile capability of this type of microscope in studying non-transparent samples (P3HT/PCBM blend solar cell film and Au nano cone array) by TER and tip-enhanced photo-luminescence (TEPL) imaging.

Experimental

Sample preparations

Blended P3HT/PCBM films (Konarka) with a weight ratio of 1 : 1 were deposited on Si substrates and thermally annealed at 140 °C for 30 min under nitrogen protection before optical measurements. The Au cones were fabricated via a top-down process[12,13] in which a cone array was dry-etched from a metal stack on silicon by ion milling. The typical geometry of the cone has a base diameter

of around 150 nm and a sharp tip with the radius down to less than 5 nm.

Instrumentation

All the tip-enhanced spectroscopic measurements were carried out in a home-built parabolic mirror-assisted near-field optical microscope.[14] The distance control of this microscope is based on shear-force feedback. Au tips with an apex size of *ca* 30 nm in diameter are reproducibly fabricated by electrochemical etching and used throughout the measurements. A 632.8 nm He–Ne laser is used for the efficient tip plasmon excitation. A Raman spectrometer (SP, SpectroPro-2558, f 300 mm, Princeton Instrument) coupled to a liquid nitrogen-cooled CCD (charge-coupled device) detector (LN2-CCD, Spec-10 : 100B, Princeton Instrument) is used for collecting the spectrum. An avalanche photodiode detector (APD, SPCM-AQR-13, Perkin-Elmer) is used for single photon counting. For blocking the elastically scattered light, one notch filter (6 OD, Semrock) and one razor-edge filter (6 OD, Semrock) are positioned in front of the entrance slits of both the Raman spectrometer and the APD. A feedback-controlled scanning stage (Physik Instrumente, PI) is used for the precise movement of the sample with an accuracy of sub-nm in the x-y plane and one angstrom in the z direction. The feedback speed of the PI table is *ca* 1 ms which is four times faster than its moving speed during our tip-enhanced spectroscopic imaging.

Results and Discussion

PM optics

We have systematically developed and experimentally proved theories of PM optics since the last ten years.[14] A typical PM configuration used in the tip-enhanced spectroscopic imaging is illustrated in Fig. 1a. The PM is placed above the sample stage and a Au tip is approached through an axial hole into the focus of the PM. The mirror is illuminated symmetrically with a radially polarized laser beam creating via reflection a diffraction-limited focal spot. Three advantages are obtained with this configuration:

(1) The parabolic mirror focuses the laser beam onto the sample surface and at the same time collects optical signals from above the sample. Hence the bottleneck problem of the opaque sample substrates is no longer an issue of concern.
(2) Parabolic mirror focusing is based on reflection and is free from chromatic aberration; it can therefore be easily adapted to work with different laser wavelengths.
(3) As shown in Fig. 1b, an NA of 0.99 can be achieved by a PM due to its geometric properties and its focusing principle. Benefiting from this large NA, an efficient and symmetric signal collection over a solid angle of 2π above the sample surface can be easily realized, which is challenging for an air objective lens. Only a minor fraction of the signal is lost because of the small axial hole opened at the top of the PM and the blockage of the tip shaft. In addition, this large NA creates in the diffraction-limited focal volume of a radially polarized laser beam cylindrically converging waves that interfere around the optical axis and form an intensity maximum in which the field is predominantly polarized along the longitudinal direction (intensity of longitudinal polarized component 14.3 times stronger than that of the transverse direction) with a decay constant on the order
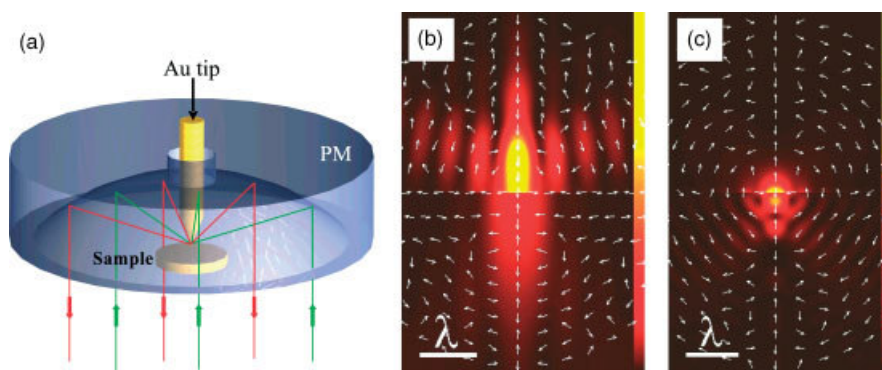
Figure 1. (a) Sketch of a parabolic mirror situated above a sample and the tip antenna approached through an axial hole into the focus of a radially polarized laser beam. Green arrows indicate the incoming laser beam and the red arrows indicate the outgoing laser beam and optical signals (Raman and PL). Snap shots of the electric field intensity distribution created by a radially polarized laser beam in the focal volume of (b) a high NA (0.99) parabolic mirror and (c) a high NA (1.4) objective lens at an air–glass interface. The white arrows indicate the polarization directions at every individual point. λ in this case is corresponding to 632.8 nm.

of λ (Fig. 1b).[15] In contrast, when the laser illuminates in transmission configuration through the objective lens (NA 1.4), the converging waves form an intensity maximum at the glass–air interface with the longitudinally polarized field component (intensity of longitudinal polarized component 3.5 times stronger than that of the transverse component) decaying within a small fraction of λ into the air-filled half space above the sample surface (Fig. 1c). Therefore, excitation of the longitudinal plasmonic oscillation of the tip antenna is much more efficient when the tip is positioned in the focus of a radially polarized laser beam in a parabolic mirror. Furthermore, a tighter focus which is slightly smaller than $\lambda/2$ is realized, which helps to minimize the background signals from the far-field focus illuminated sample area.[11]

TER imaging of the organic solar cell blend film

Conjugated polymer and fullerene blends, such as the P3HT : PCBM blend film, are promising candidates for developing low-cost and flexible photovoltaic devices.[16,17] The film morphology influences strongly the performance of P3HT : PCBM solar cell devices since it is directly related to the electron-hole pair dissociation and the charge generation process.[18] A precise experimental evaluation of the relationships between the blend film morphology, components distribution and the device performance at nanometer spatial and optical resolutions is difficult to achieve mainly because of the technical limitations of the conventional characterization methods, such as transmission electron microscopy (TEM)[19] or scanning transmission X-ray microscopy (STXM).[20] TER imaging together with the topographic imaging provide an excellent alternative for achieving this goal.

Strong PL emission can be observed from both P3HT and PCBM. The PL emission maximum appears at 1750 cm^{-1} for pristine P3HT film and at 2100 cm^{-1} for pristine PCBM film. According to our measurements, under 632.8 nm He–Ne laser illumination only the P3HT polymer exhibits well-defined Raman bands at 1450, 1385 and 728 cm^{-1} which are assigned to C=C stretching vibrations of the thiophene ring, C–C stretching and C–S–C deformation, respectively. Three weak Raman bands at 1210 cm^{-1}, 1090 cm^{-1} and 1009 cm^{-1} are assigned to the combination of C–C stretching and C–H bending, C–H bending, and C–C stretching, respectively.[21] No Raman peak is observed from pristine PCBM film. Therefore, the PL maximum of PCBM at 2100 cm^{-1} and the C=C stretching

Raman vibration mode of P3HT at 1450 cm^{-1} are followed to track the P3HT and PCBM distributions in their blend films (detailed spectroscopic information in supplementary Fig. S1).

Figure 2 shows the topographic and spectroscopic imaging by integrating 16 × 16 data points (256 Raman spectra) from a 500 nm × 500 nm area (31 nm per scan-step) of a P3HT/PCBM blend film. Considering the size of the near-field focus (<30 nm in diameter defined by the diameter of the tip apex,[22]) the 31-nm scan-step size enables us to study optical properties at two sequentially scanned data points without signal averaging. The topography reveals the presence of two islands with dimensions of several hundreds of nanometers. Figures 2b and 2c illustrate two of the 256 Raman spectra that are collected from position I and II as indicated in Fig. 2a. The red curves are fitted spectra using the fitting peaks coloured in green, orange and blue. The positions and FWHM of the green peaks are derived from those of the pristine P3HT Raman bands. Blue peaks are corresponding to the P3HT PL emission (maximum at 1750 cm^{-1}) and the two orange peaks are due to the PL emission from PCBM (maximum at 2100 cm^{-1} with a tail extending to the higher wavelengths). The PL emission from the Au tip is generally an important source contributing to the background of the tip-enhanced spectrum; however, in the spectral fitting of the P3HT/PCBM blends, its contribution to the optical background is neglected owing to the fact that its PL intensity is about two orders of magnitude weaker than the PL intensity of the P3HT and PCBM. When using these peaks to fit the original experimental data, the peak positions are fixed at the corresponding frequencies, whilst the relative intensities are carefully adjusted to reach the best fitting factor. It is through this strict fitting process that we separate the pure Raman intensity from the PL intensity and furthermore, the P3HT PL intensity from the PCBM PL intensity. As P3HT PL can be dramatically quenched when P3HT excitons dissociate at the P3HT/PCBM interface and undergo charge transfer to the lowest unoccupied molecular orbital in PCBM,[23] we prefer to use the Raman fingerprint, whose intensity is closely related to the amount of sample molecules, to determine the presence of P3HT. At the same time, as the P3HT PL quenching reflects the efficiency of charge generation at the P3HT : PCBM interface,[24] we rely on the P3HT PL intensity variations to study the local exciton dynamics between the P3HT and PCBM. Based on the above analysis and principles, we conclude from Figs. 2b and 2c that the amount of P3HT at location I is about 1.7 times (obtained by comparing the Raman intensity of the two
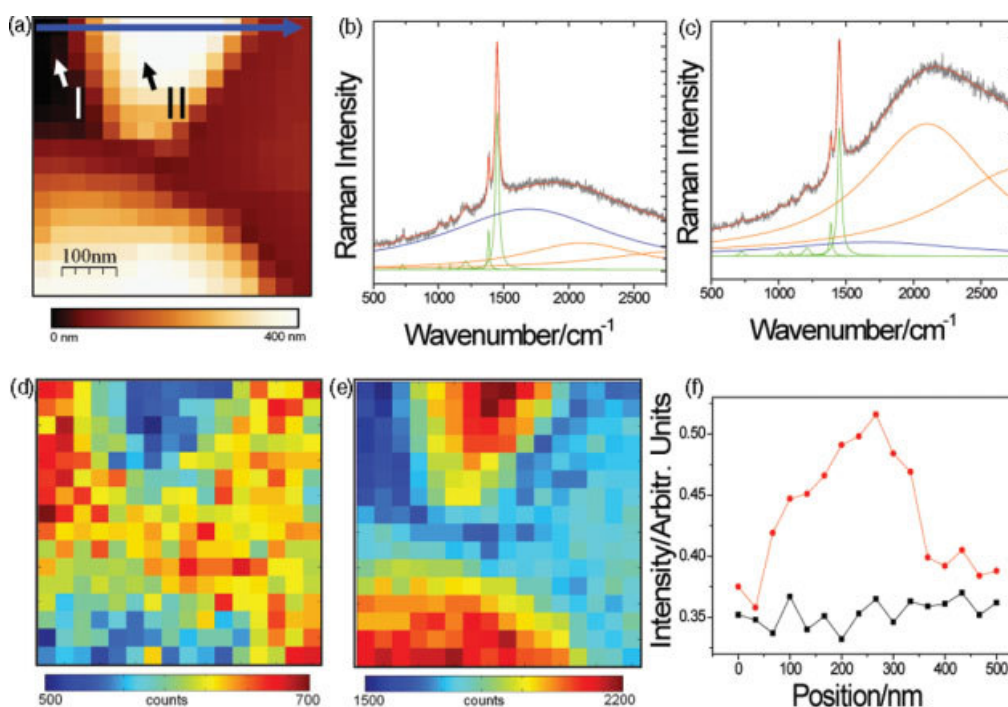
Figure 2. (a) Topographic image of the P3HT: PCBM blend solar cell film; (b) and (c) TER spectra collected at position I and II, respectively, from picture (a). The red curves are fitted to the spectra by the blue, orange and green peaks. The blue curve is derived from the PL emission profile from P3HT. The orange curves are derived from the PL emission profile from PCBM. The several green peaks are the Raman features from P3HT. (d) Raman imaging picture obtained by integrating the C=C stretching Raman peak of P3HT from 1442 to 1458 cm^{-1}; (e) PL imaging picture by integrating the PCBM PL intensity from 2098 to 2102 cm^{-1}; (f) comparison of the PCBM PL intensity changes along the line marked in Fig. 2a with tip-enhanced spectroscopic imaging (red curve) and normal confocal Raman imaging (black curve). Scan area: 500 nm × 500 nm. Acquisition time: 2 s per spectrum. Laser power at the focus: 250 W. Tip-sample distance: 2 nm.

locations) higher than that of the location II, whereas the PCBM PL signal collected at location I is only 1/24 (obtained by comparing the area ratios of PCBM PL/P3HT PL at location I and location II) of the location II.

In order to overview the distribution of P3HT and PCBM in the whole scan area, we integrated, for all the 256 Raman spectra, the intensity of the C=C stretching Raman vibrational mode from 1442 cm^{-1} to 1458 cm^{-1} for Raman imaging of the P3HT distribution (Fig. 2d) and the PCBM PL intensity from 2098 cm^{-1} to 2102 cm^{-1} for PL imaging of the PCBM distribution (Fig. 2e). Comparing Figs. 2a, 2d and 2e, straightforward overview maps of the P3HT and PCBM distribution in the blend film are clearly unfolded. In the P3HT:PCBM blend film, the PCBM PL signal variations are not necessarily related to the number of PCBM molecules present. For example, when PCBM is thoroughly mixed with P3HT at molecular level, the PCBM PL can be totally quenched owing to the complete exciton dissociation at the polymer–fullerene interfaces. However, when the PCBM molecules aggregate into clusters with the sizes larger than the PCBM exciton diffusion length (at the scale of several nanometers), strong PL can be observed owing to the radiative recombination of excitons before they can reach the polymer–fullerene interface. Considering the facts that P3HT polymers do not form aggregates in the blend film and the strong PCBM PL signals (shown in Fig. 2e) observed from the two islands, we conclude that the islands are composed mostly of PCBM. The topographically flat regions around the two islands are P3HT-enriched areas, based on the observation of strong Raman intensities from the C=C stretching vibrational mode. The distributions of these two components demonstrate an opposite tendency. This is due to the fact that although PCBM and P3HT are well mixed in the pristine blend film, PCBM molecules tend to diffuse and aggregate into clusters during the thermal-annealing process leaving behind regions around the clusters in a PCBM-depleted condition. At the same time, P3HT polymer molecules are squeezed out of the PCBM clustering region and form P3HT-enriched regions around them. This phenomenon had been reported before, however, at a scale of several micrometers by Klimov *et al.*[24] using macro-Raman mapping. Now, the clear observation of this phenomenon at the nanometer scale using TER imaging is demonstrated in Fig. 2. Figure 2f further confirms the capability of tip-enhanced spectroscopic imaging (red curve) in monitoring the changes of optical signals occurring on nanometer scales which are impossible to be managed by confocal Raman mapping (black curve) due to the diffraction-limited focus size. The quality of the image depends greatly on the number of data points per line scan. Denser data points per line enable a higher picture resolution but at the same time, increase the integral time for one imaging picture. This in turn increases the requirement for the stability of the instrumentation. We can, so far, successively image a 1 m × 1 m area with 32 data points per line for six times with reproducible results without the need for instrumentation adjustment in between the measurements.

Whilst the Raman fingerprint information provides concrete proof for the determination of chemical components distribution, the variations of PL intensity from P3HT and PCBM indirectly relate to the exciton dissociation and charge transfer that is the central process for transferring the solar energy to electric power. Our investigations point out a promising application of TER and PL spectroscopic imaging in this field. Systematic investigations of solar cell blend film are presently carried out in our lab.

Tip-enhanced PL imaging of Au nano cones

The plasmonic properties of metal nanostructures have been a hot topic in the past several years as assemblies of metal nanoparticles find a variety of applications in the fields of biosensors,[25] photonic waveguiding,[26] optical switching[27] and so on. The process of metal nanosphere assembly or aggregation is known to alter the optical properties of the nanostructure due to the interparticle electromagnetic coupling, which will cause variations in the PL intensity and plasmonic resonance shifts. As this electromagnetic coupling strongly depends on the excitation wavelength, the particle material, size, orientation, shape and the interparticle distances,[28,29] addressing experimentally this issue precisely and systematically is a demanding task. PL emission is an important criterion to evaluate the efficiency of the plasmonic excitation. The plasmon resonance is often determined from the white light spectrum of a metallic nanoparticle. Recently it was shown that the PL emission spectrum of aggregated Au particles also closely follows the resonance curve obtained from the white light spectrum regardless of the specific geometry of an individual nanoparticle.[30] Since the creation of an electron-hole pair is proportional to the square of the electric field strength at the local optical field, strong emission of PL photons by their recombination points at locations with high field strength. In order to relate the plasmon resonance and the PL emission with a precisely tunable geometrical arrangement under well-defined polarization conditions, we have investigated the plasmon excitation in Au nano cones and plasmon coupling between a sharp Au nano cone and a sharp Au tip as a function of their tip-to-tip position.

Figure 3 shows optical images of a Au nano cone recorded with our PM-assisted optical microscope in confocal configuration using radially (a) and azimuthally (b) polarized higher order laser modes. As described in the PM optics section, in the focal volume of a radially polarized laser beam a dominantly stronger electric field distribution exists in the longitudinal direction than that of the transverse direction; whilst for an azimuthally polarized laser beam the electric field in the focal volume is exclusively distributed in the transverse direction.[15] Such a distinctive difference in the electric field distribution is greatly helpful for determining the orientation of the principal dipole moment oscillation in a plasmonic nanostructure. The nano cone is more efficiently excited by the longitudinal electric field than the transverse electric field resulting in the ten times stronger PL emission signals observed in Fig. 3a than that of the Fig. 3b. This indicates that the principal dipole moment is orientated vertically *versus* the substrate, i.e. parallel to the cone axis.

By precisely positioning the tip above a nano cone in the well-polarized field we can use tip-enhanced PL imaging as a sensitive probe to study plasmonic dipole–dipole coupling as a function of the tip-to-tip position. Figure 3c shows three plasmon-enhanced spectra obtained from a Au nano cone, from the tip apex and from a configuration where the tip apex is positioned in close proximity above the nano cone. Both the nano cone and the tip apex exhibit strong PL emission with the intensity maxima (obtained by spectral fitting) at 850 cm^{-1} (1.854 eV) and 1000 cm^{-1} (1.835 eV). When the tip is positioned right above the nano cone, a sharper peak with a small shoulder appears in the spectrum exhibiting an intensity maximum at 1330 cm^{-1} (1.794 eV), which is 0.060 eV red-shifted *versus* that of the nano cone and 0.041 eV red-shifted *versus* that of the Au tip alone. Whilst the red-shifted PL emission energy reflects the coupling between the plasmonic dipole of the tip apex and the plasmonic dipole of the Au cone,[12] the values of the red-shifted
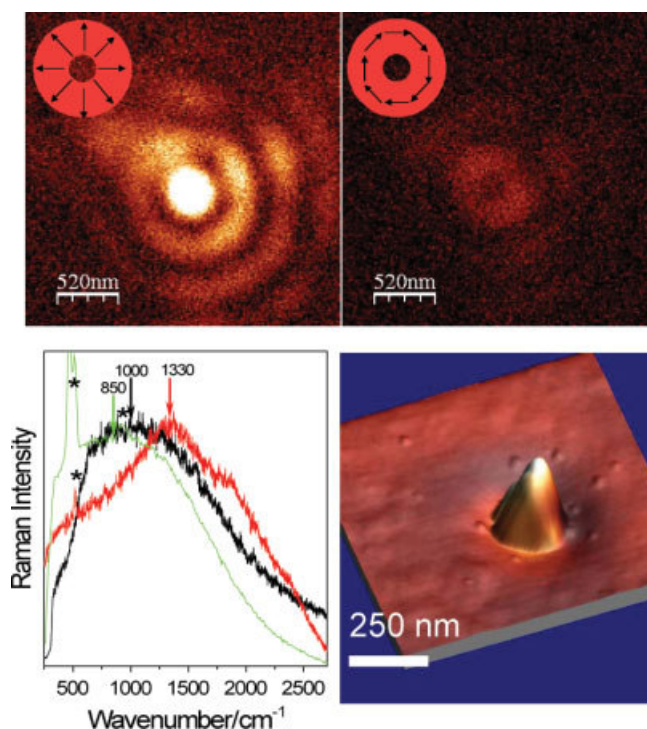

Figure 3. PL scans of a Au cone excited with (a) radially and (b) azimuthally polarized laser mode. Insets of Figs 3a and 3b illustrate the polarization directions of the respective laser modes. (c) Plasmon-enhanced spectra (normalized) collected from one Au cone (green), the apex of the Au tip (black) and the small gap between the Au tip apex and the top of the cone (red). The peaks labelled with * come from the Si substrate. (d) A superposition of the 3-D topography of a Au cone colourcoded with the PL intensity obtained when the cone is scanned beneath the tip. The brighter colour indicates a stronger optical signal.

PL emission energy can be used for the evaluation of the dipole coupling strength. Recently, Pettinger *et al.*[22] have reported a red shift from 1. 906 to 1.826 eV and an intensity increase of the TER spectral background for a tip approaching from far away to as close as 1 nm from a layer of guanine/ClO4-adsorbed on a Au (111) crystal surface, assigned to a strongly distance-dependent Au-tip and Au-surface plasmon coupling.

We have recently studied the plasmonic coupling between a sharp Au tip and a free standing Au nano cone on a Si substrate using tip-enhanced PL imaging based on the PM-assisted confocal microscope. Figure 3d shows a three dimensional topographic image recorded by scanning a nano cone below the tip at a constant distance of several nanometers with the PL signal intensity as a colour code.[12] It can clearly be seen that the strongest PL appears when the tip is positioned right above the top of the cone. Together with the red-shifted PL emission observed in Fig. 3c, we conclude that the strongest dipole–dipole coupling can be achieved by aligning the plasmonic dipole moment of the tip apex right on top of the dipole moment of a Au cone. The much weaker optical signal observed when the tip scans above the Si substrate shows that the PL from the Si can be neglected. Therefore, using tip-enhanced PL imaging one can obtain the following information in just one measurement: Firstly, the appearance of dipole–dipole coupling; secondly, how to spatially arrange the orientations of the two dipole moments to facilitate their plasmonic coupling and thirdly to evaluate the coupling strength between two dipoles.

Benefiting from the flexibility and accuracy of obtaining the optimized conditions for a strong dipole-dipole coupling between the tip and the plasmonic materials under test, we are able to illustrate details of the nano cone structure with an optical resolution down to about 10 nm,[12] as well as resolving small Au dots of 1–2 nm height on a smooth Au film with the tip-enhanced PL imaging at an optical resolution of about 12 nm.[10]

Conclusion

Tip-enhanced spectroscopic (Raman and PL) imaging of non-transparent samples, P3HT/PCBM blend solar cell film and Au nano cones, are realized using PM-assisted near-field optical microscopy. In addition to its unrestricted choices of sample substrates regarding the transparency, this technique demonstrated excellent stability and accuracy in the determination and imaging of different chemical components in a mixed system at nanometer scales based on Raman fingerprint and PL information. It also provides excellent polarization conditions allowing the excitation of exclusively transversely oriented transitional dipole moments or nearly exclusively longitudinally oriented dipole moments, which is greatly helpful for the investigation of the plasmonic properties of photonically active materials with an optical resolution down to about 10 nm. Further promising applications of this PM-assisted spectroscopic imaging technique in the field of material science are anticipated.

Acknowledgements

Supporting information

Supporting information may be found in the online version of this article.

References

[1] R. M. Stöckle, Y. D. Suh, V. Deckert, R. Zenobi, *Chem. Phys. Lett.* **2000**, *318*, 131.
[2] N. Hayazawa, Y. Inouye, Z. Sekkat, S. Kawata, *Chem. Phys. Lett.* **2001**, *335*, 369.
[3] A. Hartschuh, N. Anderson, L. Novotny, *J. Microsc.* **2003**, *210*, 234.
[4] E. Bailo, V. Deckert, *Angew. Chem. Int. Ed.* **2008**, *47*, 1658.
[5] A. Hartschuh, E. J. Sánchez, X. S. Xie, L. Novotny, *Phys. Rev. Lett.* **2003**, *90*, 095503.
[6] B. Pettinger, B. Ren, G. Picardi, R. Schuster, G. Ertl, *Phys. Rev. Lett.* **2004**, *92*, 096101.
[7] A. Hartschuh, H. H. Qian, A. J. Meixner, N. Anderson, L. Novotny, *Nano Lett.* **2005**, *5*, 2310.
[8] H. H. Qian, C. Georgi, N. Anderson, A. A. Green, M. C. Hersam, L. Novotny, A. Hartschuh, *Nano Lett.* **2008**, *8*, 1363.
[9] J. Steidtner, B. Pettinger, *Phys. Rev. Lett.* **2008**, *100*, 236101.
[10] M. Sackrow, C. Stanciu, M. A. Lieb, A. J. Meixner, *ChemPhysChem* **2008**, *9*, 316.
[11] J. Stadler, C. Stanciu, C. Stupperich, A. J. Meixner, *Opt. Lett.* **2008**, *33*, 681.
[12] M. Fleischer, C. Stanciu, F. Stade, J. Stadler, K. Braun, A. Heeren, M. Haeffner, D. P. Kern, A. J. Meixner, *Appl. Phys. Lett.* **2008**, *93*, 111114.
[13] M. Fleischer, F. Stade, A. Heeren, M. Haeffner, D. P. Kern, K. Braun, C. Stanciu, A. J. Meixner, in Excitons and Plasmon Resonances in Nanostructures, eds A. O. Govorov, Z. M. Wang, A. L. Rogach, H. Ruda, and M. Brongersma, MRS Symposia Proceedings No. 1055E (Materials Research Society, Warrendale, PA, 2008), Paper No. 1055-GG10-04.
[14] C. Stanciu, M. Sackrow, A. J. Meixner, *J. Microsc.* **2008**, *229*, 247.
[15] M. A. Lieb, A. J. Meixner, *Opt. Express* **2001**, *8*, 458.
[16] W. L. Ma, C. Y. Yang, X. Gong, K. Lee, A. J. Heeger, *Adv. Funct. Mater.* **2005**, *15*, 1617.
[17] G. Li, V. Shrotriya, J. S. Huang, Y. Yao, T. Moriarty, K. Emery, Y. Yang, *Nat. Mater.* **2005**, *4*, 864.
[18] B. C. Thompson, J. M. J. Fréchet, *Angew. Chem. Int. Ed.* **2008**, *47*, 58.
[19] X. N. Yang, J. Loos, S. C. Veenstra, W. J. H. Verhees, M. M. Wienk, J. M. Kroon, M. A. J. Michels, R. A. J. Janssen, *Nano Lett.* **2005**, *5*, 579.
[20] C. R. McNeill, B. Watts, L. Thomsen, W. J. Belcher, A. L. D. Kilcoyne, N. C. Greenham, P. C. Dastoor, *Small* **2006**, *2*, 1432.
[21] M. Baibarac, M. Lapkowski, A. Pron, S. Lefrant, I. Baltog, *J. Raman Spectrosc.* **1998**, *29*, 825.
[22] B. Pettinger, K. F. Domke, D. Zhang, R. Schuster, G. Ertl, *Phy. Rev. B* **2007**, *76*, 113409.
[23] H. Hoppe, M. Niggemann, C. Winder, J. Kraut, R. Hiesgen, A. Hinsch, D. Meissner, N. S. Sariciftci, *Adv. Funct. Mater.* **2004**, *14*, 1005.
[24] E. Klimov, W. Li, X. Yang, G. G. Hoffmann, J. Loos, *Macromolecules* **2006**, *39*, 4493.
[25] A. V. Whitney, J. W. Elam, S. L. Zou, A. V. Zinovev, P. C. Stair, G. C. Schatz, R. P. Van Duyne, *J. Phys. Chem. B* **2005**, *109*, 20522.
[26] W. L. Barnes, A. Dereux, T. W. Ebbesen, *Nature (London)* **2003**, *424*, 824.
[27] M. J. Feldstein, C. D. Keating, Y. H. Liau, M. J. Natan, N. F. Scherer, *J. Am. Chem. Soc.* **1997**, *119*, 6638.
[28] K. L. Kelly, E. Cornado, L. L. Zhao, G. C. Schatz, *J. Phys. Chem. B* **2003**, *107*, 668.
[29] P. K. Jain, S. Eustis, M. A. El-Sayed, *J. Phys. Chem. B* **2006**, *110*, 18243.
[30] M. Steiner, C. Debus, A. V. Failla, A. J. Meixner, *J. Phys. Chem. C* **2008**, *112*, 3103.

Chapter 3. Tuning the Raman and fluorescence spectra of SAMs on a metallic substrate by an applied DC-electric field.

In this chapter the experiments were performed on the latest updated microscope with STM feedback and a new diode laser, which operates in pulsed or in continuous wave mode. The motivation of this work is to investigate the collective influence of electrical and optical excitations on a self assembled monolayer (SAM) films on a gold substrate in a STM tunneling junction. This system can be used as a model interface between a molecule and an electrode, as well as it is used in organic electronics. The combination of TERS and STM allow studying molecules on metallic surfaces und varying DC electric fields. We showed the influence of the e-field on a SAM of 5-Chloro-2-Mercatobenzothiazole (CL-MBT) by measuring spectra at different bias voltages. We acquired the chemical fingerprints of the molecule and impose reproducible changes within the individual spectra.

Moreover the chemically bonded molecules give rise to a massive enhancement of the luminescence under bias voltages which are higher than the energetic position of the Highest Occupied Molecular Orbital (HOMO) respective to the Fermi level of the sample. This effect is much likely driven by stimulated emission of electrons from the Fermi-level of the metal substrate to the HOMO of the molecule, while the gap mode acts as a plasmonic resonator. We present experiment results and theoretical models with a simulation. The enhancement is dependent of both the bias voltage and the power of the incident laser light and show a nonlinear behavior for both variables. To our best knowledge this effect has not been reported so far.

This chapter is based on:

Braun, K.; Kern, A. M.; Wang, X.; Adler, H.; Peisert, H.; Chasse, T.; Zhang, D.; Meixner, A. J. "Superluminescence from an optically pumped single molecule tunneling junction by injection of plasmon induced hot electrons" *submitted* **03/2014**

Superluminescence from an optically pumped single molecule tunneling junction by injection of plasmon induced hot electrons

Kai Braun[1], Andreas M. Kern[1], Xiao Wang[1], Hilmar Adler[1], Heiko Peisert[1], Thomas Chassé[1], Dai Zhang[1], and Alfred J. Meixner[1]*

[1] Eberhard Karls University Tübingen, Institute of Physical and Theoretical Chemistry, 72076

Tübingen, Germany

Scanning tunneling microscopy, hot electrons, scanning near-field optical microscopy, light emitting diode, tip enhanced Raman spectroscopy, quantum plasmonics

Here, we introduce and experimentally demonstrate a bias-driven superluminescent point light-source based on an optically pumped molecular junction (gold-substrate/molecule/gold-tip) of a scanning tunneling microscope, operating at ambient conditions and providing almost three orders of magnitude higher electron-to-photon conversion efficiency than state of the art. A

positive, steadily increasing bias-voltage shows a step-like rise of the optical signal emitted from the junction, along with 40% spectral narrowing, reflecting stimulated emission and optical feedback. The unique optical gain medium is based on hole-injection from the tip (anode) into the highest occupied orbital of the closest molecule (lower level). A large population inversion is achieved by optical pumping as plasmon induced hot electrons above the Fermi-level of the substrate (upper level, kathode). Raman scattering from gap molecules acts as an optical seed and feed-back is provided by the cavity plasmon-polariton resonance. The system reflects many essential features of a superluminescent light emitting diode.

The emission of photons from the gap of a scanning tunneling microscope (STM) has been a focus of interest for more than twenty years[1,2] and has been used for acquiring spectroscopic information with ultra-high spatial resolution[3]. For pure metal surfaces[4,5] or organic monolayers adsorbed directly on a metal surface[6], the emission of light originates predominantly from the radiative decay of localized surface plasmons (LSP) excited by inelastic electron tunneling (IET) as the direct luminescence of the molecules is quenched. If the molecules are decoupled from the metal surface by an ultra-thin dielectric spacer, intrinsic molecular luminescence can be observed down to the single-molecule level, showing vibronic bands[7,8]. Very recently electroluminescence from a conducting molecule, bridging the gap was observed[9]. The efficiency of photoemission is quite low, typically with a quantum efficiency per tunneling electron of the order of 10^{-6}-10^{-5} emitted photons[2]. A different approach for ultra-high resolution optical spectroscopy has emerged. So-called tip enhanced Raman scattering (TERS)[10,11], or gap mode near-field optical microscopy[12], has attracted great interest as a means for local Raman[13,14] or luminescence spectroscopy[15] with nanometer spatial resolution. In this approach, the metal tip serves as an

optical antenna and generates an electromagnetic near field in the gap, locally enhancing excitation. At the same time, the emission and radiation of photons into the far field[16] is enhanced due to the increased local density of optical states in the gap. Since efficient Raman scattering from molecules in the gap requires gap widths as short as one nanometer, electron tunneling is meanwhile routinely used to control the tip/sample distance[14,17,18], or to measure in tip/specimen/substrate conduction junctions[19].

Here, we demonstrate bias driven amplification of tip enhanced Raman scattering from a single or very low number of molecules enclosed in an optically pumped tunneling junction of a STM. For efficient excitation and collection of photons the molecular junction was centered in the focus of a parabolic mirror used in place of the objective lens in a confocal microscope[20-23]. We have chosen 5-chloro-2-mercaptobenzothiazole (Cl-MBT) molecules since (i) they chemically bind to the metal substrate allowing their π-electron system to overlap with the surface orbitals of the substrate, (ii) their first electronically excited state lies in the ultraviolet and cannot be reached by the laser photons at $\lambda = 632.8$ nm, therefore reducing photo damage and (iii) they have a static electric dipole moment with a negative partial charge located on the Cl-atom bound to the benzene ring.
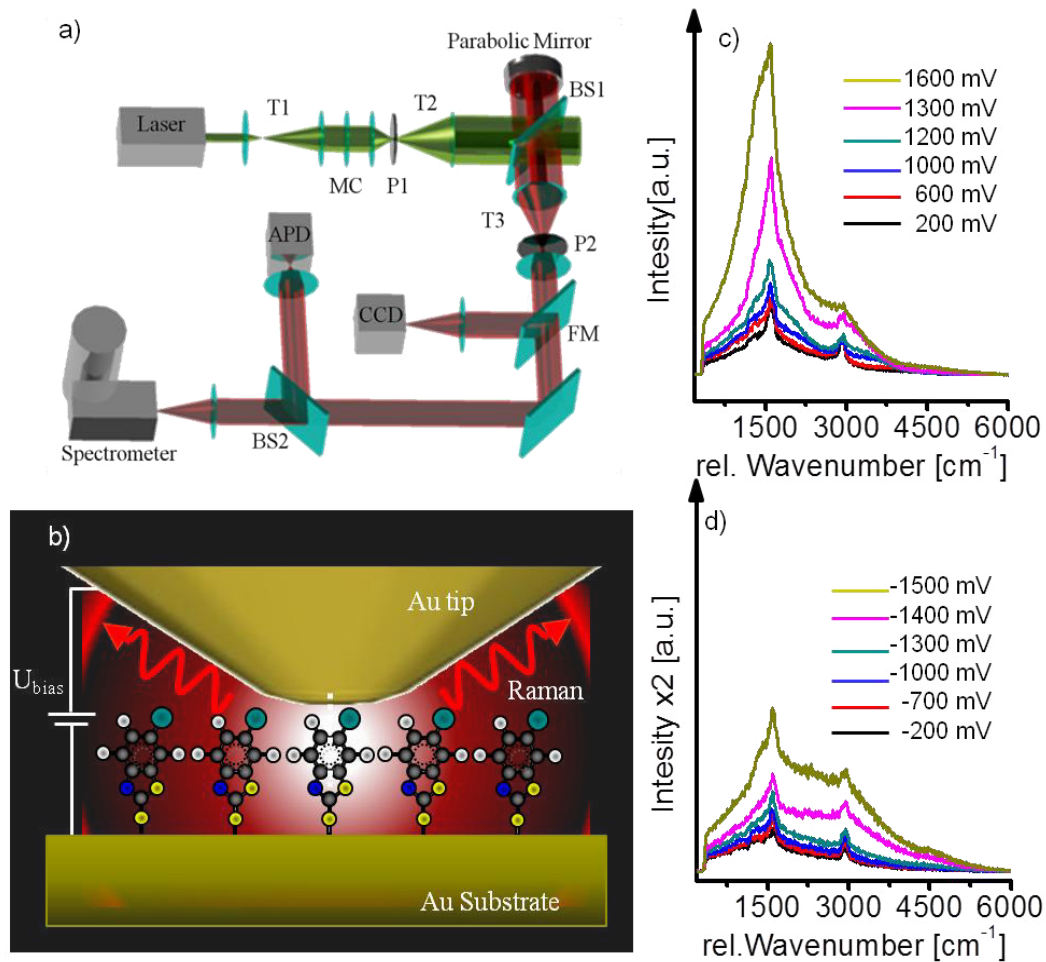
Figure 1. a) Experimental arrangement with a parabolic mirror giving excellent optical access to the gold/molecule/gold junction of scanning tunneling microscope. b) Typical tunneling junction consisting of a sharp gold that tip statically positioned one nanometer above a gold substrate covered with a monolayer of chemisorbed Cl-MBT-molecules illuminated with laser light (632.8 nm) for tip enhanced Raman scattering (TERS). Sequences of TERS-spectra recorded from the tunneling under constant laser illumination as a function of the bias voltage For positive bias voltage c) a threshold-like intensity increase of the narrow Raman band is observed for $U_{bias} >$ 1200 mV. For negative bias voltage d) mainly the broad luminescence background increases.

When a positive bias-voltage is applied between tip and sample and steadily increased while the tunneling current is kept constant, the negatively charged part of the molecules experiences an increasing attractive force towards the positively charged tip. In the low bias-voltage range, i.e. for $|U_b| < 1000$ mV, the spectra (Fig. 1c and 1d) change only moderately irrespective of the polarity of the applied voltage and one can observe the typical tip-enhanced Raman bands of Cl-MBT residing on a broad luminescence background. When U_b exceeds $+ 1000$ mV we observe a strong intensity increase of more than one order of magnitude affecting mainly the aromatic Raman bands around 1600 cm^{-1} and hence leading to an overall spectral narrowing. In contrast for negative bias mainly the luminescence background increases leading to a spectral broadening (Fig. 1d, Fig. 2a, i-iv).
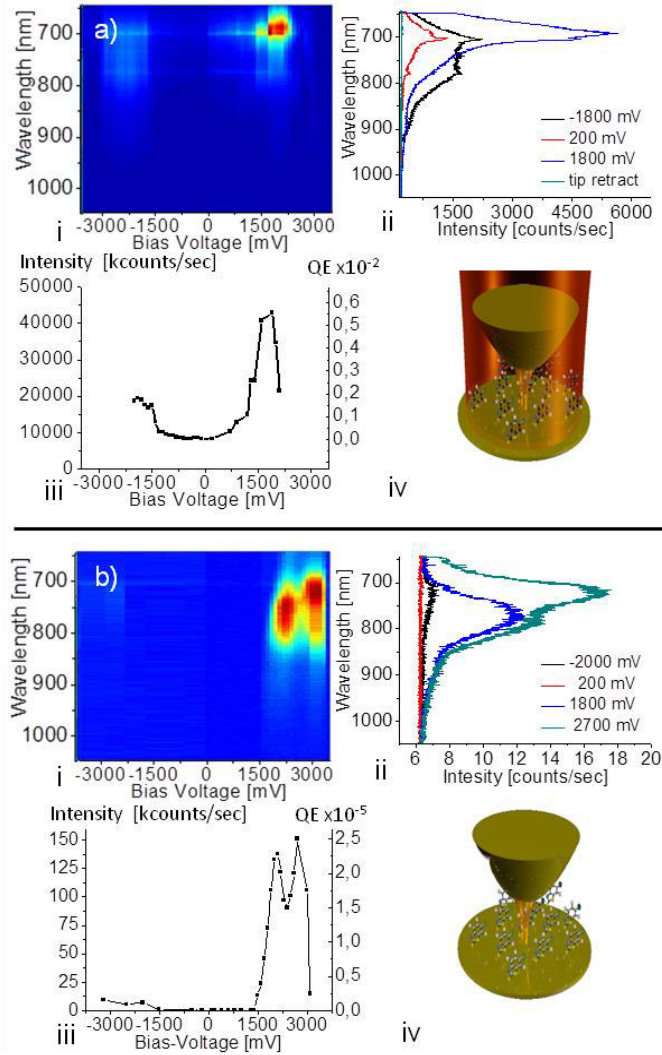
Figure 2. a) TERS-spectra from the tunneling junction excited at λ = 632.8nm (iV) with 270μW as a function of the bias voltage (i), (ii) with the respective spectrally integrated intensity trajectory (iii) as a function of bias voltage. b) Electroluminescence spectra excited by inelastic tunneling without laser illumination (iv) as a function of the bias-voltage (i), (ii). All spectra were recorded with the same tunneling current (1nA) and are normalized to 1s integration time. The corresponding quantum efficiencies (QEs) are defined as the number of Stokes-shifted photons per tunneling electron and can directly be compared for the two situations.

This behavior is fully reversible up to U_b=2000 mV (further data see supplementary Fig. S6). When the voltage scan is repeated with the same tunneling current but without simultaneous laser illumination (Fig. 2b, i-iv) we observe a sharp onset of weak electroluminescence signal at $U_b \geq$ 1500 mV due to inelastic tunneling (Fig. 2b, iii) reaching a first maximum of 138 kcounts[-1] at U_b = 1900 mV followed by a second maximum at U_b = 2300 mV. Ultraviolet photoelectron spectroscopy measurements of a monolayer of Cl-MBT on Au reveal that the energetic distribution of the highest occupied molecular orbital (HOMO) of the surface-bound molecules with respect to the Fermi level of the Au substrate lies at around (-1.5) – (-2.0) eV and the d-bands of Au lie below -2.0 eV (see supplementary Fig. S2) which is coincident the two intensity maxima in Fig. 2b, iii. In agreement with theoretical predictions[24,25] the sharp onset of the electroluminescence signal marks the potential difference that has to be overcome by the anode for hole injection into the HOMO of the molecule located at the narrowest position of the tip-sample gap and for which an effective current stars to flow through this molecule. For electrons near the Fermi energy recombining with the hole, the excess energy corresponds to the band at around 775 nm observed for U_b = 1800 mV (blue spectrum in Fig. 2b, ii). When the bias voltage is further increased, $U_b \geq$ 2000 mV, electrons from surface orbitals of the d-band begin to tunnel elastically to the tip, also giving rise to holes in the metal. The recombination of these holes with electrons from the Fermi level is then the source of the energetically higher, blue-shifted band observed for U_b = 2700 mV with a maximum at 725 nm (green spectrum in Fig. 2b, ii). If the bias voltage is inverted (negative tip and positive sample) we observe only a very weak electroluminescence signal originating from the blue shifted band centered at 725 nm and indicating that electron flow through the molecule is hindered. In contrast, electroluminescence form a pure Au/Au junction induced by inelastic electron tunneling is independent of the tip

polarity[1-5]. The situation here is analogue to a light emitting diode (LED) consisting of a pn-junction. When the LEDs anode lead has a voltage that is more positive than its cathode lead by at least the LED's forward voltage drop, current flows that can emitting photons with an energy equivalent to the band gap. The quantum efficiency of 10^{-5} is matching state of the art[2,9]. Comparing the data in Fig. 2 a) and b) we note a dramatic effect of the incident radiation: the bias dependent increase of the TERS spectrum is about three orders of magnitude larger than the electroluminescence signal at U_b = 1800 mV under identical tunneling current, which is equivalent to a conversion efficiency of almost 10^{-2} photons per tunneling electron. In addition we observe a sharpening of the TERS signal with increasing bias voltage with a fixed peak maximum at 700 nm where as the electroluminescence band at U_b = 1800 mV has a red sifted maximum at 775 nm and a three times larger half-width. Both effects cannot be explained simply adding the TERS-signal and the electroluminescence. Recently, it has been shown that plasmon-excited nanoparticles can be an efficient source of hot electrons[26,27]. Consequently, illuminating the tip/sample junction with a focused laser beam polarized along the tip's axis, a coupled surface plasmon oscillation in the Au-tip and the underlying sample Au-surface is induced, manifesting itself as a highly localized surface charge oscillation at the very apex of the tip and the Au surface below. This oscillating surface charge constitutes an efficient laser-power dependent source of hot electrons that can recombine with the hole in the junction-molecule analogue to a large population inversion in the upper level with a large number of hot electrons and a lower level of the depopulated HOMO of the molecule in the gap. As a consequence the electron to photon conversion efficiency QE at a bias of 1800 mV is almost three orders of magnitude larger for the optically pumped junction (Supplementary Fig. S5). The dependence of the TERS-spectra recorded at U_b = 1800 mV and constant tunneling current as a function of the

incident laser power (IL) (pulse length 100 ps, 80 MHz repetition rate) also exhibits a distinct nonlinear intensity increase both for the luminescence background and the background subtracted Raman signal (see inset). The spectrally integrated intensity of the TERS signal Fig.3 c) shows a low-gain regime for an optical pump power, IL < 250 μW, a high-gain regime for 250 μW < IL < 750 μW and saturates for IL > 750 μW. The spectra in the low gain regime are mainly determined by the plasmon resonance of the Au/Au-junction and have a full width half maximum of about 90 nm with a superimposed narrow Raman peak. For higher pump power the spectral width of the luminescence background decreases by about 40% to 55 nm and forms together with the Raman bands at 1600 cm^{-1} one sharp peak. Such a spectral narrowing along with the nonlinear intensity increase observed as a function of bias voltage or of optical pump power is a reliable sign of signal amplification by positive feedback directing a portion of the amplified Raman and photoluminescence (PL) emission back towards the substrate/molecule hybrid system. Indeed resonant surface plasmon amplification by stimulated emission from plasmonic nano- and micro-structures has recently been predicted and experimentally realized. Considering the fact that the Raman scattering and PL emission processes originate in the very center of the tip/substrate gap, any generated photon will first couple to the gap mode before being scattered to the far field. While the gap mode's plasmon resonance is very broad, exhibiting a quality factor of only Q≈15, the resonantly stored energy is extremely well localized spatially, in a volume having an upper limit of approximately 4×4×1 nm3 (see Supplementary Fig. S1).
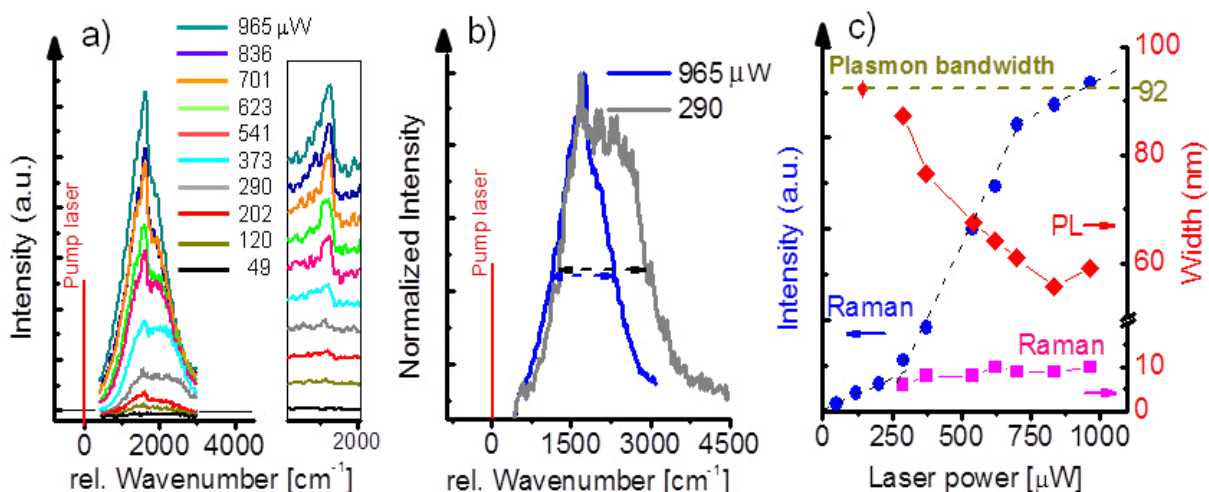
Figure 3. a) TERS spectra recorded as a function of optical pump power for a constant bias voltage of +1800 mV with the background subtracted Raman band at 1600 cm^{-1} shown in the inset. 3b) Illustrating the spectral narrowing by overlapping the spectra recorded at 290 μW and at 965 μW. c) Spectrally integrated intensity of the Raman peak (blue), the luminescence background (gray circles), the luminescence FWHM (red) and the FWHM if the Raman band (purple) as a function of optical pump power.

Hence, feedback of the emitted energy back to the quantum system can thus still occur. Surface plasmon amplification by stimulated emission from a nanometer sized optical gain medium similar to a laser has recently been predicted and experimentally realized[28-30]. When our system is optically pumped, stimulated emission is much greater than spontaneous emission due to a large population of hot electrons near the Fermi-level (upper level) and one hole in the HOMO (lover level) where as the Q-factor of the plasmonic resonator is rather. Hence spectral narrowing (Fig. 3a) and the nonlinear intensity increase (Fig. 3c) cannot be expected to be as pronounced as for a conventional laser with a high Q resonator. Hence the emission of our

system should be called superluminescence[31] or amplified spontaneous emission[32] in perfect agreement with similar systems known from classical laser physics.
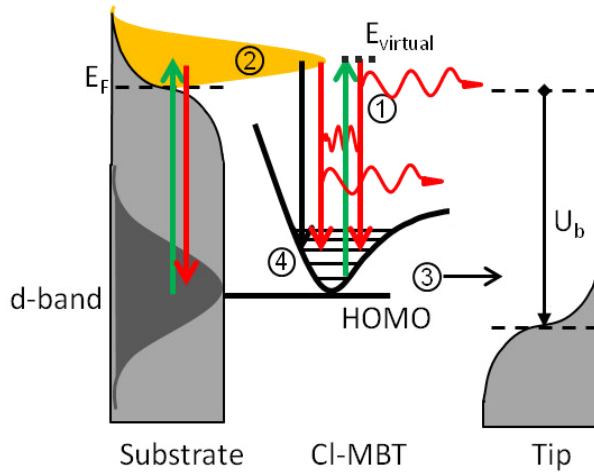

Figure 4. Schematic energy level diagram of the gap/molecule hybrid system in a laser-illuminated tunneling junction. The incident radiation (green arrows) leads to (1) Raman scattering form the surface-bound molecules and generates hot surface electrons (2) with a non-thermal distribution indicated in yellow. Nonradiative processes are indicated by black arrows, i.e. elastic tunneling of electrons from the molecules' HOMO levels to the tip (3) when the Fermi-level of the tip falls below the HOMO-level and nonradiative recombination of hot electrons. Stimulated emission occurs from hot electrons recombining with holes in the molecules repopulating the HOMO levels (4).

The individual processes involved can be summarized in an energy level scheme as represented in Fig. 4. Green arrows represent processes drawing energy from the incident pump-laser field, i.e. Raman scattering from the surface-bound molecules (1) and generation of hot electrons from the d-band (2). Plasmon excitation is not shown in this figure. When the Fermi level of the tip drops below the energy of a surface-bound molecule's HOMO energy, efficient

elastic electron tunneling from the molecule closest to the tip sets in (3), leaving behind a hole in the molecule. This hole can then easily be refilled by a hot surface electron from the Au substrate (4), emitting a photon which can be observed by the detector. The rate of this optical process depends on two factors: the local density ρ_e^* of hot surface electrons which is a function of the incident laser power, and the tunneling rate k_t from the HOMO to the tip which is a function of the applied bias voltage. The fact that we observe significant spectral narrowing for positive bias voltages above threshold (Fig. 1b) and high pump power (Fig. 3a) suggests that optical feedback takes place.

Depletion of the HOMO via elastic tunneling to the tip and generation of hot electrons by irradiating the plasmonic system with incident laser light apparently leads to a population inversion between an empty HOMO-level and the higher lying energy level of hot electrons and thus gain is expected under the very conditions for which enhanced emission can be observed experimentally: TERS scattering from neighboring molecules acts as an optical seed signal in the cavity mode and is amplified in the molecular tunneling junction by stimulated emission from hot electrons recombining with holes in the surface-bound molecules. This leads to the spectral narrowing of the amplified signal (Fig. 1b and Fig. 3a)) in the metal-molecule-metal junction for a positive bias voltage above threshold. For a negative bias voltage the negatively polarized molecules are repelled from the tip rather forming a thin insolating layer. Hence, electrons must tunnel directly from the tip to the metal substrate, leading to the broad luminescence in Fig. 1d). The behavior of the molecule/gap hybrid system can be described with a coupled rate-equation model for the population P_0 of the molecule's HOMO level and the gap mode's energy density ρ_ϕ (see Supplementary). This model reproduces the nonlinear increase of the emitted signal as a

function of the incident laser power (vis. Fig. 3 c) and the bias voltage (vis. Fig. 2 a), the corresponding curves shown in Supplementary Fig. S7. The optical system comprising the gap mode, plasmonic feed-back and the substrate/molecule hybrid system is an important step towards an efficient superluminescent point-light source, containing an extremely small and fast optical gain medium exhibiting a population inversion, i.e. the hot-electron recombination of the molecule's depleted HOMO level, bi-directionally coupled to a resonator, i.e. the plasmonic gap mode.

Our results demonstrate how optical enhancement inside the plasmonic cavity can be further increased by a stronger localization via tunneling through a molecule. We anticipate that stimulated emission from an STM junction will advance our fundamental understanding of quantum plasmonics and lead to new analytical applications. Furthermore, this concept represents the basis for novel ultra-small, fast, optically and electronically switchable devices and could find applications in high-speed signal processing and optical telecommunications.

ASSOCIATED CONTENT

Supporting Information.

Figure S1: Tip enhanced spatial resolution. Figure S2: Valence band spectra for Au and Cl-MBT on Au. Figure S3: Pulse conversion scheme. Figure S4: Calculation tip-enhancement factor. Calculation of QE and amplification. Figure S5: Comparison Au/Au- to Au/Cl-MBT/Au-junction. Figure S6: Reproducibility. Figure S7: Switching behavior. Theoretical modeling. Figure S8: Simulations. Table 1: Parameters for Simulation. Materials and methods

AUTHOR INFORMATION

Corresponding Author

Alfred J. Meixner
alfred.meixner@uni-tuebingen.de

Eberhard Karls University Tübingen, Institute of Physical and Theoretical Chemistry, 72076 Tübingen, Germany

Author Contributions

 The manuscript was written through contributions of all authors. All authors have given

approval to the final version of the manuscript.

Notes

Any additional relevant notes should be placed here.

ABBREVIATIONS

  STM scanning tunneling microscopy; LSP localized surface plasmon; IET inelastic electron

tunneling; TERS tip enhanced Raman spectroscopy; Cl-MBT 5-Chloro-2-Mercaptobenzotiazole;

HOMO highest occupied molecular orbital; LED light emitting diode; PL photoluminescence; IL incident laser power.

REFERENCES

(1) Gimzewski, J. K.; Sass, J. K.; Schlitter, R. R.; Schott, J. Enhanced Photon Emission in Scanning Tunnelling Microscopy *Europhys. Lett.* **1989**, *8*, 435.

(2) Rossel, F.; Pivetta, M.; Schneider, W.-D. Luminescence experiments on supported molecules with the scanning tunneling microscope *Surf. Sci. Rep.* **2010**, *65*, 129.

(3) Berndt, R.; Gimzewski, J. K.; Schlittler, R. R. Enhanced photon emission from the STM: a general property of metal surfaces *Ultramicroscopy* **1992**, *42–44, Part 1*, 355.

(4) Berndt, R.; Gimzewski, J. K.; Johansson, P. Inelastic tunneling excitation of tip-induced plasmon modes on noble-metal surfaces *Phys. Rev. Lett.* **1991**, *67*, 3796.

(5) Johansson, P.; Monreal, R.; Apell, P. Theory for light emission from a scanning tunneling microscope *Phys. Rev. B* **1990**, *42*, 9210.

(6) Berndt, R.; Gaisch, R.; Gimzewski, J. K.; Reihl, B.; Schlittler, R. R.; Schneider, W. D.; Tschudy, M. Photon Emission at Molecular Resolution Induced by a Scanning Tunneling Microscope *Science* **1993**, *262*, 1425.

(7) Qiu, X. H.; Nazin, G. V.; Ho, W. Vibrationally Resolved Fluorescence Excited with Submolecular Precision *Science* **2003**, *299*, 542.

(8) Wu, S. W.; Nazin, G. V.; Ho, W. Intramolecular photon emission from a single molecule in a scanning tunneling microscope *Phys. Rev. B* **2008**, *77*, 205430.

(9) Reecht, G.; Scheurer, F.; Speisser, V.; Dappe, Y. J.; Mathevet, F.; Schull, G. Electroluminescence of a Polythiophene Molecular Wire Suspended between a Metallic Surface and the Tip of a Scanning Tunneling Microscope *Phys. Rev. Lett.* **2014**, *112*, 047403.

(10) Hayazawa, N.; Inouye, Y.; Sekkat, Z.; Kawata, S. Metallized tip amplification of near-field Raman scattering *Opt. Commun.* **2000**, *183*, 333.

(11) Stockle, R. M.; Suh, Y. D.; Deckert, V.; Zenobi, R. Nanoscale chemical analysis by tip-enhanced Raman spectroscopy *Chem. Phys. Lett.* **2000**, *318*, 131.

(12) Raschke, M. B.; Lienau, C. Apertureless near-field optical microscopy: Tip-sample coupling in elastic light scattering *Appl. Phys. Lett.* **2003**, *83*, 5089.

(13) Hartschuh, A.; Pedrosa, H. N.; Novotny, L.; Krauss, T. D. Simultaneous Fluorescence and Raman Scattering from Single Carbon Nanotubes *Science* **2003**, *301*, 1354.

(14) Zhang, R.; Zhang, Y.; Dong, Z. C.; Jiang, S.; Zhang, C.; Chen, L. G.; Zhang, L.; Liao, Y.; Aizpurua, J.; Luo, Y.; Yang, J. L.; Hou, J. G. Chemical mapping of a single molecule by plasmon-enhanced Raman scattering *Nature* **2013**, *498*, 82.

(15) Kinkhabwala, A.; Yu, Z.; Fan, S.; Avlasevich, Y.; Mullen, K.; Moerner, W. E. Large single-molecule fluorescence enhancements produced by a bowtie nanoantenna *Nat Photon* **2009**, *3*, 654.

(16) Paolo, B.; Jer-Shing, H.; Bert, H. Nanoantennas for visible and infrared radiation *Rep. Prog. Phys.* **2012**, *75*, 024402.

(17) Stadler, J.; Schmid, T.; Zenobi, R. Nanoscale Chemical Imaging Using Top-Illumination Tip-Enhanced Raman Spectroscopy *Nano Lett.* **2010**, *10*, 4514.

(18) Steidtner, J.; Pettinger, B. Tip-enhanced Raman spectroscopy and microscopy on single dye molecules with 15 nm resolution *Phys. Rev. Lett.* **2008**, *100*, 236101.

(19) Liu, Z.; Ding, S.-Y.; Chen, Z.-B.; Wang, X.; Tian, J.-H.; Anema, J. R.; Zhou, X.-S.; Wu, D.-Y.; Mao, B.-W.; Xu, X.; Ren, B.; Tian, Z.-Q. Revealing the molecular structure of single-molecule junctions in different conductance states by fishing-mode tip-enhanced Raman spectroscopy *Nat Commun* **2011**, *2*, 305.

(20) Sackrow, M.; Stanciu, C.; Lieb, M. A.; Meixner, A. J. Imaging nanometre-sized hot spots on smooth Au films with high-resolution tip-enhanced luminescence and Raman near-field optical microscopy *Chemphyschem* **2008**, *9*, 316.

(21) Stanciu, C.; Sackrow, M.; Meixner, A. J. High NA particle- and tip-enhanced nanoscale Raman spectroscopy with a parabolic-mirror microscope *J. Microsc.-Oxford* **2008**, *229*, 247.

(22) Wang, X.; Zhang, D.; Braun, K.; Egelhaaf, H. J.; Brabec, C. J.; Meixner, A. J. High-Resolution Spectroscopic Mapping of the Chemical Contrast from Nanometer Domains in P3HT:PCBM Organic Blend Films for Solar-Cell Applications *Adv. Funct. Mater.* **2010**, *20*, 492.

(23) Zhang, D.; Heinemeyer, U.; Stanciu, C.; Sackrow, M.; Braun, K.; Hennemann, L. E.; Wang, X.; Scholz, R.; Schreiber, F.; Meixner, A. J. Nanoscale Spectroscopic Imaging of Organic Semiconductor Films by Plasmon-Polariton Coupling *Phys. Rev. Lett.* **2010**, *104*, 056601.

(24) Buker, J.; Kirczenow, G. Theoretical study of photon emission from molecular wires *Phys. Rev. B* **2002**, *66*, 245306.

(25) Galperin, M.; Nitzan, A. Optical properties of current carrying molecular wires *J. Chem.Phys.* **2006**, *124*.

(26) Knight, M. W.; Sobhani, H.; Nordlander, P.; Halas, N. J. Photodetection with Active Optical Antennas *Science* **2011**, *332*, 702.

(27) Mukherjee, S.; Libisch, F.; Large, N.; Neumann, O.; Brown, L. V.; Cheng, J.; Lassiter, J. B.; Carter, E. A.; Nordlander, P.; Halas, N. J. Hot Electrons Do the Impossible: Plasmon-Induced Dissociation of H2 on Au *Nano Lett.* **2012**, *13*, 240.

(28) Bergman, D. J.; Stockman, M. I. Surface Plasmon Amplification by Stimulated Emission of Radiation: Quantum Generation of Coherent Surface Plasmons in Nanosystems *Phys. Rev. Lett.* **2003**, *90*, 027402.

(29) Noginov, M. A.; Zhu, G.; Belgrave, A. M.; Bakker, R.; Shalaev, V. M.; Narimanov, E. E.; Stout, S.; Herz, E.; Suteewong, T.; Wiesner, U. Demonstration of a spaser-based nanolaser *Nature* **2009**, *460*, 1110.

(30) Stockman, M. I. The spaser as a nanoscale quantum generator and ultrafast amplifier *J. Opt.* **2010**, *12*, 024004.

(31) Saleh, B. E. A.; Teich, M. C. *Fundamentals of Photonics*; Wiley: New York, 1991; Vol. Wiley Series in Pure and Applied Optics.

(32) Siegman, A. *Lasers*; University Science Books: Mill Valley, California, 1986.

For Table of Contents only: